

POLITECNICO DI TORINO

Collegio di Ingegneria Chimica e dei Materiali

**Master of Science Course
in Materials Engineering**

Master of Science Thesis

**Electronic Properties of Graphene-based
Field Effect Transistors**



Tutor

Dr. A. Lamberti

Hosting University Supervisor

Prof. H. Goto

Candidate

Luisa Baudino

March 2018

Sommario esteso

Fin dalla sua scoperta nel 2004 [1], [2], [3], [4], il grafene ha riscosso molto interesse nella comunità scientifica a ragione delle sue peculiari quanto singolari proprietà particolarmente adatte all'industria elettronica. Nonostante l'iniziale picco di interesse per il materiale bi-dimensionale sia oramai scemato con gli anni, il grafene rimane tutt'oggi uno dei fulcri della ricerca per materiali innovativi e nuove proprietà vengono continuamente scoperte o confermate [5], [6], [7].

Il grafene possiede una mobilità elettronica intrinsecamente molto alta [8], [9], il che lo rende un ottimo materiale per la realizzazione di dispositivi ad alta frequenza, e in determinate condizioni può presentare un trasporto di tipo balistico [10], [11]. Tra le sue particolarità si annoverano anche un effetto di campo ambipolare e l'effetto di parità [12]. Questo consiste nella differenziazione di alcune proprietà in base al numero di piani atomici: in particolare si può ricordare il fatto che i campioni con numero dispari di piani possiedono una dispersione di energia lineare, mentre qualora abbiano un numero di piani pari presentano una dispersione di tipo parabolico. Queste ed altre proprietà, quali un effetto hall quantistico detto "semi intero" che assume valori semi interi [13] e una possibile super conducibilità [14], fanno sì che l'industria elettronica veda il grafene come uno dei possibili materiali del futuro.

Il lavoro di tesi descritto nel presente elaborato ha riguardato lo studio delle proprietà di trasporto elettronico di due tipi di dispositivi a base grafene. Inizialmente si è focalizzata l'attenzione su dispositivi cosiddetti "convenzionali", in cui il grafene è interamente in contatto con il substrato. In un secondo momento ci si è dedicati alla realizzazione di dispositivi con grafene sospeso, che dovrebbero mostrare un netto miglioramento delle proprietà, essendo il grafene libero di comportarsi a pieno titolo come un materiale bi-dimensionale qual è [10].

La struttura dell'elaborato è la seguente. Nel primo capitolo si affrontano i temi base del grafene, al fine di situare questo materiale nel giusto contesto scientifico-culturale. Vengono esplorati la sua storia, la sua struttura e le sue principali proprietà, nonché i principali metodi di produzione. Si affrontano pertanto i temi di reticolo reale [19] e reciproco [20], di dispersione lineare (e non) di energia [7], [8], [12], di effetto Hall quantistico [8], [13], [22], e di spettroscopia Raman [22], [33-37]. Tra le tecniche di ottenimento del grafene [38-42] si ricordano l'esfoliazione meccanica tra le tecniche "top-down" e la deposizione in fase vapore CVD tra le tecniche "bottom-up".

Seguono, nel secondo capitolo, delle considerazioni di base sui transistor e di fisica dei semiconduttori. I transistor vengono introdotti partendo dalla legge di Moore [44], per passare in seguito allo sviluppo vero e proprio dei dispositivi attraverso una breve analisi storica [48-57] e ai principi fisici che ne permettono il funzionamento. Vengono inoltre riportate le equazioni di base dei vari regimi di funzionamento dei transistor.

Vengono quindi mostrati i metodi sperimentali che hanno permesso la realizzazione dei dispositivi analizzati. Tra i dispositivi realizzati si possono distinguere due sottogruppi: un primo in cui il grafene è in diretto contatto con il substrato, dispositivi in seguito chiamati NSG (Non Suspended Graphene), e un secondo in cui il grafene vorrebbe essere sospeso su una trincea realizzata in fotoresist. La scelta di questi due tipi di dispositivi è stata motivata dalla lettura di alcuni articoli che asserivano che i dispositivi con grafene sospeso presentassero un netto miglioramento delle proprietà di trasporto elettronico [10], [19]. Dal momento che la preparazione dei due tipi di campioni è abbastanza simile, viene in primo luogo descritta in modo dettagliato la preparazione dei dispositivi NSG. Per quanto riguarda la preparazione dei dispositivi SG, ripresa in parte dall'articolo di *Tombros et al.* (2011) [26], vengono messe in evidenza le differenze rispetto alla preparazione dei primi.

Entrambi i tipi di dispositivi vengono realizzati su wafer di silicio presentanti 300 nm di ossido nativo SiO₂, opportunamente lavato in bagno ultrasonico di acetone e metanolo al fine di eliminare impurità

superficiali. Questo viene quindi ricoperto da uno strato di HMDS idrofobico tramite spin coating, quindi si procede con la deposizione di grafene per esfoliazione meccanica con la tecnica del nastro adesivo. L'identificazione del numero di piani grafenici di ogni campione viene effettuata durante un'osservazione al microscopio ottico. Tramite apposito software è possibile analizzare i picchi dell'assorbimento nello spettro del verde di substrato e target grafenico e calcolarne la differenza. Si usano quindi l'equazione (1) per ottenere il Relative Green Shift (RGS) e il fitting di tipo sperimentale riportato in Figura 1 per risalire al numero di piani grafenici.

$$RGS = \frac{G_s - G_g}{G_g} \quad (1)$$

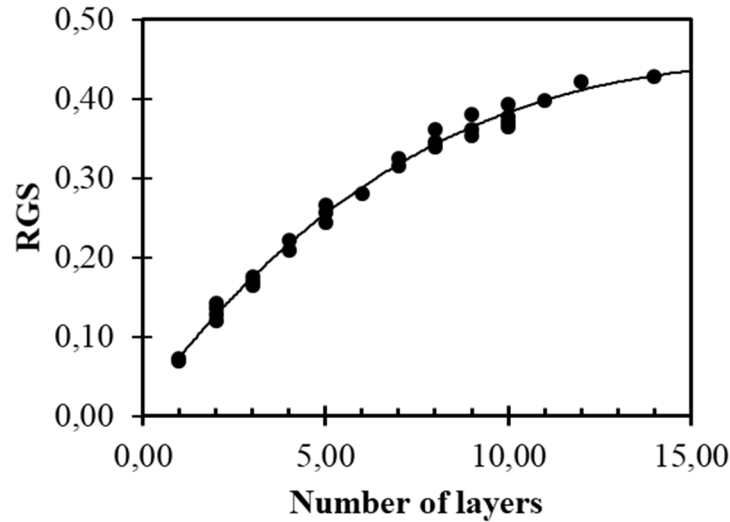


Figura 1. Evoluzione sperimentale del RGS rispetto al numero di piani grafenici (modificata da [66]).

I campioni vengono quindi protetti da due strati di photoresist litografico positivo, rispettivamente un primo strato di copolimero (9% poli- (Metil MetAcrilato-co-Acido Metacrilico), in Lattato di Etile (MMA 8.5-MMA EL9)) [67] e un secondo di PMMA, cui seguono dei processi di litografia a cannone elettronico e di modellizzazione del dispositivo tramite i software CAD DraftSight e WeCas per realizzare gli elettrodi sui target. Lo sviluppo dopo ogni scrittura litografica è effettuato con una miscela MIBK:IPA (1:3) per circa un minuto. I campioni vengono successivamente sciacquati in IPA per 30 secondi e asciugati con una pistola di azoto sotto pressione. Si procede infine con la deposizione degli elettrodi tramite un processo di PVD di due strati: un primo di cromo di 5 nm e in un secondo strato di oro di 100 nm. Una volta effettuato il processo di lift-off in acetone i dispositivi sono pronti per essere testati. Un riepilogo dei passaggi per la realizzazione di questo tipo di device è presente nella Figura 2.

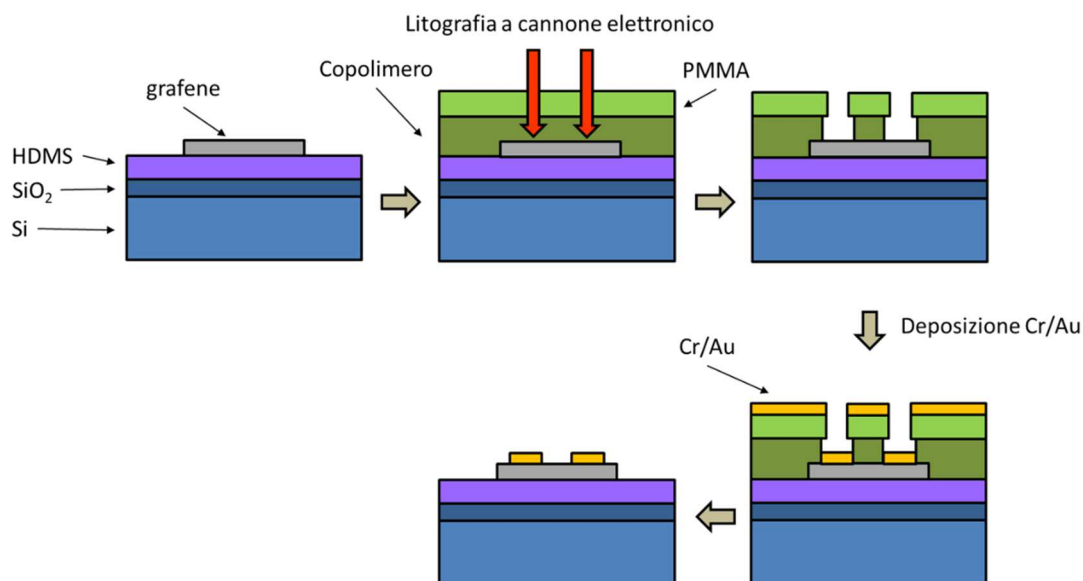


Figura 2. Riassunto del processo di realizzazione dei dispositivi NSG.

I dispositivi SG si differenziano da quelli NSG per la natura del primo rivestimento del substrato. In questo caso, infatti, non viene usato HMDS bensì LOL-2000, o poli-metilglutarimmide [71], e lo spessore è decisamente maggiore in quanto sarà responsabile della sospensione del piano grafenico. Lo spessore cercato è di circa $1,3\text{ }\mu\text{m}$, il che corrisponde a circa cinque processi di deposizione per spin coating. Tuttavia, uno spessore ottimale deve ancora essere definito, e la precisione della deposizione per spin coating non permette un adeguato controllo dimensionale. La tecnica con cui il grafene viene depositato sui dispositivi è la stessa che nel caso di dispositivi NSG, ma l'individuazione del numero di piani grafenici non può essere effettuata durante la scansione al microscopio ottico a causa del colore giallastro dello strato di LOL che falserebbe i risultati (Figura 3). La tecnica più adatta ad identificare il numero di piani grafenici in questo caso è la spettroscopia Raman, che deve essere effettuata a fine processo di produzione dei dispositivi, affinché la presenza dello strato di resist organico non falsi i risultati.

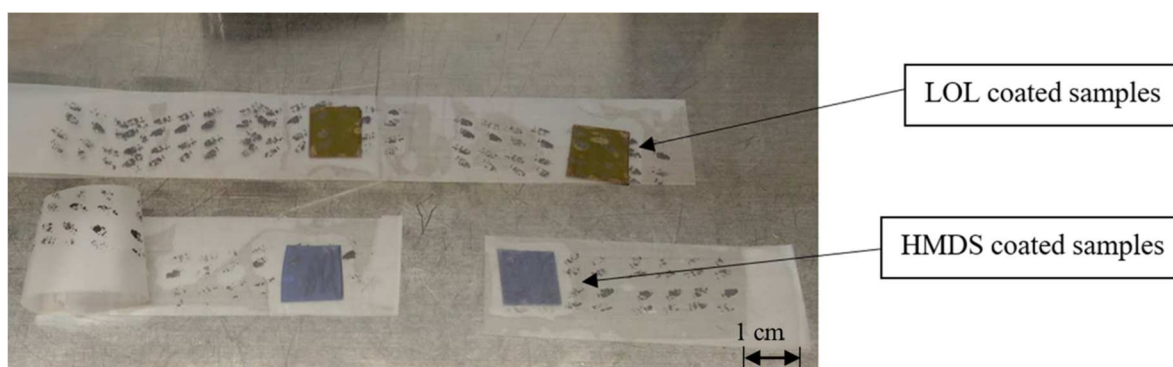


Figura 3. Campioni ricoperti di LOL (in alto) e di HMDS (in basso) durante la deposizione di grafene con la tecnica del nastro adesivo. Si può notare che i campioni per i dispositivi sospesi presentano una superficie giallastra, mentre quelli per i dispositivi tradizionali presentano la tipica superficie blu-viola dei campioni di silicio.

Una volta individuati i target si procede anche in questo caso con una serie di processi litografici e modellizzazione, resi più difficili dalla presenza dello strato di resist organico che rende l'osservazione al microscopio a scansione elettronica più ardua. Lo sviluppo delle parti esposte viene realizzato sempre

con la miscela MIBK 1:3 IPA e con le stesse tempistiche. La modellizzazione e deposizione degli elettrodi di questi dispositivi è analoga a quella dei dispositivi NSG, mentre si differenziano poi nuovamente i processi di lift-off. Mentre nel caso dei dispositivi NSG si era usato acetone, in questo caso non può essere utilizzato in quanto attaccherebbe anche lo strato di LOL sottostante il target grafenico (Appendice 1). Si usa quindi un bagno di xilene a 80°C in seguito al quale i campioni vengono asciugati con una pistola di azoto sotto pressione. Un'esposizione a raggi UV lontani con una lampada a mercurio attacca quindi lo strato di LOL e rimuove le ultime tracce di copolimero residue dopo il lift-off. Lo sviluppo dopo l'esposizione è effettuato a temperatura ambiente per un minuto in lattato di etile ed è seguito da una sciacquata in esano. L'intero processo di preparazione dei dispositivi con grafene esfoliato meccanicamente e sospeso è riportato in Figura 4.

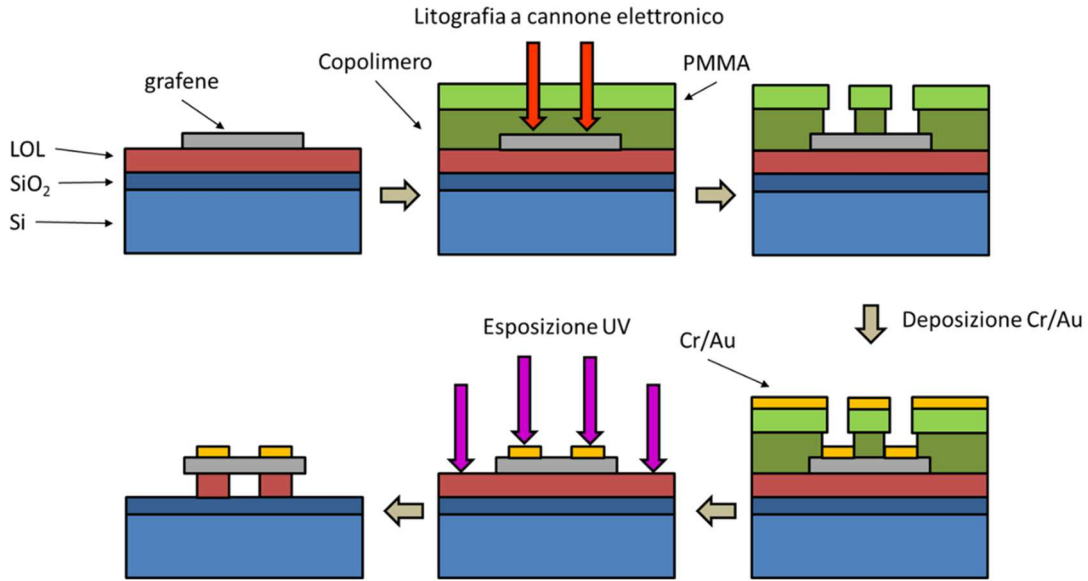


Figura 4. Riepilogo del processo di realizzazione dei dispositivi SG.

Si è quindi passati alla caratterizzazione dei dispositivi precedentemente realizzati. I dispositivi tradizionali (NSG) sono stati sottoposti a misure di conducibilità a quattro punti con geometria a barre di tipo Hall in Ultra High Vacuum (10^{-7} Torr $^{-1}$). I valori di mobilità μ sono stati ricavati dalle curve di conducibilità tramite l'equazione (2) in cui C_{sub} rappresenta la capacità del substrato e $\left| \frac{d\sigma}{dV_g} \right|$ la pendenza della curva di conducibilità rispetto alla tensione del gate. Dalla variazione della posizione del punto di Dirac dopo il trattamento di ricottura ΔV_g , inoltre, è possibile risalire alla quantità di impurezze rilasciate durante il processo tramite l'equazione (3), in cui q rappresenta la carica elementare, pari a $1.6 * 10^{-19}$ C [73].

$$\mu = \frac{1}{C_{sub}} * \left| \frac{d\sigma}{dV_g} \right| \quad (2)$$

$$n = \frac{C_{sub} * \Delta V_g}{q} \quad (3)$$

Tutti i dispositivi NSG analizzati sono stati testati prima e dopo un trattamento di ricottura di 1 ora a 100 °C. Questo è necessario al fine di rimuovere eventuali tracce di vapore acqueo e ossigeno adsorbite superficialmente durante il processo di preparazione dei dispositivi ([3], [73]), o di resist residuo dopo i processi di lift-off ([60], [74]), che spesso sono responsabili di un apparente drogaggio di tipo p nei dispositivi. Un prospetto delle caratteristiche dei dispositivi è riportato nella Tabella 1, dove è possibile

vedere che la maggior parte dei dispositivi presenta un drogaggio di tipo p , coerente con l'assorbimento superficiale di impurezze precedentemente accennato. L'unico dispositivo presentante un drogaggio di tipo n è quello realizzato sul campione 14. È possibile inoltre notare che oltre al diverso drogaggio, questo dispositivo presenta anche un valore di mobilità decisamente superiore a quelli degli altri dispositivi, raggiungendo un valore di $8696 \text{ cm}^2/\text{Vs}$ dopo il trattamento termico.

Tabella 1. Prospetto delle caratteristiche dei dispositivi NSG ottenute da test a quattro terminali. Si riportano la mobilità elettronica prima e dopo il trattamento termico (TT) a 100°C per un'ora

Dispositivo #	Numero di piani	Lunghezza canale, μm	Larghezza canale, μm	Drogaggio	μ_e prima deTT, (cm^2/Vs)	μ_e dopo il TT (cm^2/Vs)
3	Monolayer	2.00	3.04	P	1739	2609
14	Monolayer	2.00	2.06	N	6957	8696
15.2	Monolayer	1.00	1.96	P	2609	3478
15.1	Bilayer	2.00	7.11	P	3478	4348

Un confronto tra i tre dispositivi monolayer è riportato in Figura 5. In esso è possibile notare come i valori di conducibilità delle lacune per i tre dispositivi siano abbastanza simili, mentre quelli degli elettroni sono molto diversi a seconda del dispositivo considerato. D'altra parte, è anche vero che i valori di conducibilità degli elettroni dei singoli dispositivi non variano considerevolmente in seguito al trattamento termico, mentre quelli delle lacune si riducono di circa un terzo del valore iniziale.

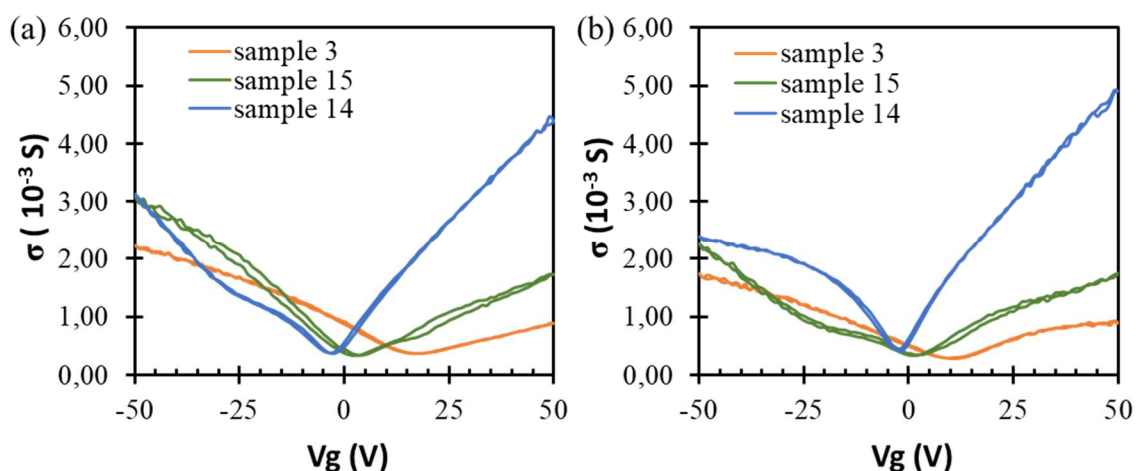


Figura 5. Confronto dei tre dispositivi monolayer non sospesi (a) prima e (b) dopo il trattamento di ricottura di un'ora a 100°C .

Volendosi soffermare sull'effetto della ricottura dei dispositivi (**Tabella 2**), è possibile notare come tutti i dispositivi presentanti lo stesso tipo di drogaggio rispondano al trattamento termico nello stesso modo, indipendentemente dalla temperatura cui questo è stato effettuato (nel caso del dispositivo 3, una seconda ricottura è stata effettuata per un'ora a 110°C). Anche in questo caso, infatti, solo il dispositivo 14 mostra un incremento nella mobilità di entrambi i portatori di carica e il punto di Dirac è situato nella regione delle tensioni negative anche dopo il trattamento termico.

Tabella 2. Caratteristiche dei dispositivi NSG dopo il trattamento termico. Per ogni dispositivo vengono riportati lo scostamento del punto di Dirac, la quantità di impurezze rilasciate, le mobilità finali e le variazioni di mobilità di elettroni (μ_e) e lacune (μ_h).

Dispositivo #	ΔV_g [V]	Impurezze rilasciate	$\Delta\mu_e$ [%]	μ_e finale [cm ² /Vs]	$\Delta\mu_h$ [%]	μ_h finale [cm ² /Vs]
3	-10	7,19 E+11	+ 50 %	2609	- 25 %	2609
3 (at 110 °C)	-2	1,44 E+11	0	2609	- 33 %	1739
14	+0.5	3,59 E+10	+ 25 %	8696	+ 67 %	8696
15 (MLG)	-2	1,44 E+11	+ 33 %	3478	- 50 %	2609
15 (BLG)	-13	9,34 E-11	+ 25 %	4348	- 77 %	609

La migliore qualità del dispositivo del campione 14 (Figura 6) rispetto agli altri si nota anche nella simmetria della mobilità di elettroni e lacune, come previsto dalla teoria [77], [80], che raggiungono il valore di 8696 cm²/Vs. Un abbozzo di questo comportamento può essere visto anche nel dispositivo 3 che dopo un primo trattamento termico presenta una mobilità di lacune e elettroni pari a 2609 cm²/Vs. Tuttavia, in questo caso i valori ottenuti sono decisamente inferiori, nonché transitori dal momento che dopo una seconda ricottura, volta a migliorare le proprietà del dispositivo, queste non solo non migliorano bensì peggiorano. Tuttavia, un aspetto comune a tutti i campioni è l'insorgere di una saturazione nel ramo delle tensioni in cui si trova il punto di Dirac, dopo il trattamento termico di ricottura. Questo effetto potrebbe essere causato dal trasferimento di carica dagli elettrodi metallici al piano grafenico [84], [85].

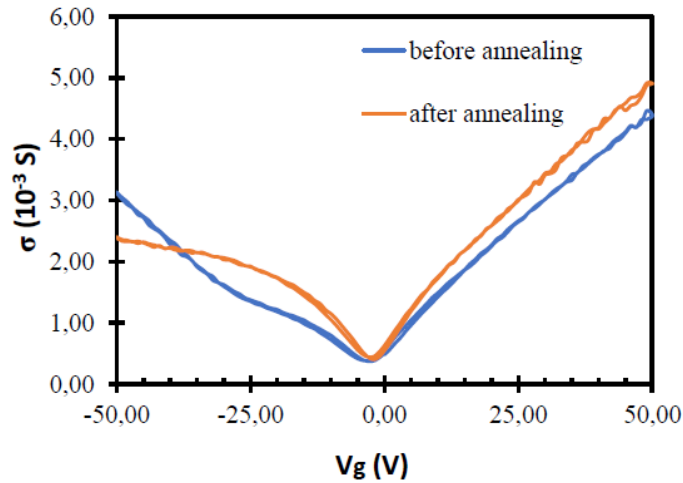


Figura 6. Curva di conducibilità del dispositivo realizzato sul campione 14 prima (in blu) e dopo (in arancione) il trattamento di ricottura di 1 ora a 100 °C.

È stato inoltre possibile realizzare un confronto tra un dispositivo monolayer e uno bilayer realizzati sullo stesso campione (Figura 7). Questo ha permesso di verificare sperimentalmente che le curve dei dispositivi MLG sono lineari mentre quelle dei dispositivi BLG sono paraboliche in prossimità del punto di Dirac [8], [12]. La forma parabolica deriva dalla presenza di termini non diagonali nell'hamiltoniana a basse energie del bistrato [20], [81], [82], termini motivati dalla asimmetria dei due piani grafenici dei campioni BLG. Questo tipo di Hamiltoniana descrive il comportamento di fermioni chirali massivi, al contrario di quanto accade nel caso di campioni monolayer.

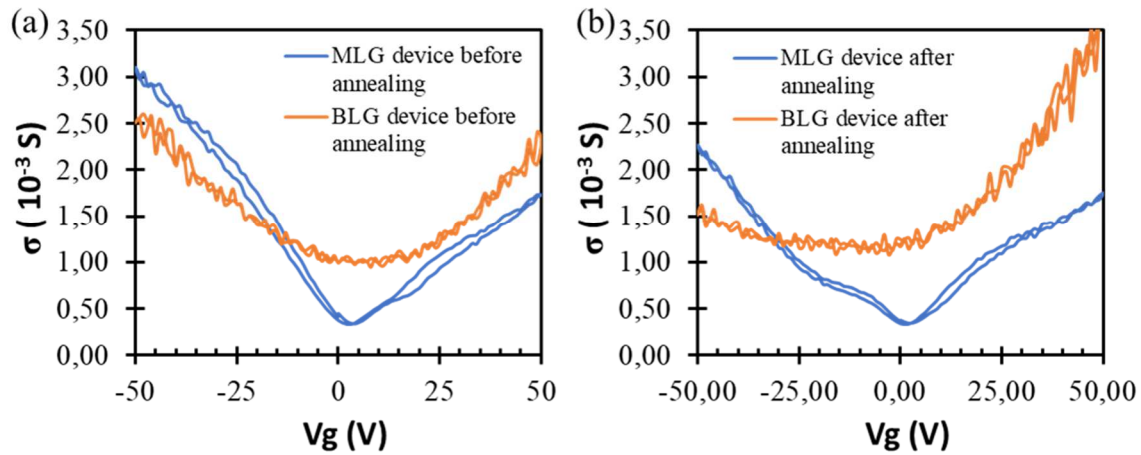


Figura 7. Confronto tra un dispositivo MLG e uno BLG realizzati sul campione 15 (a) prima e (b) dopo il trattamento di ricottura a 100 °C per un'ora

Tuttavia, come è possibile notare sia nelle curve che nei valori numerici riportati nella **Tabella 3**, il trattamento termico è risultato nefasto nel caso di questo campione. Si può notare infatti che sebbene il punto di Dirac si sia avvicinato al suo valore teorico e la mobilità degli elettroni sia aumentata, quella delle lacune è crollata a valori molto bassi. Nel caso del campione MLG è ragionevole pensare che le impurezze rilasciate durante il trattamento termico siano state riassorbite, dal momento che il ramo delle tensioni positive sembra riacquistare la giusta concavità, mentre quello delle tensioni negative la perde in seguito alla ricottura. Il caso del campione BLG è di più difficile interpretazione, poiché non presenta sporgenze anomale, bensì una rotazione della curva stessa in seguito al trattamento termico. Tuttavia, essendo nello stesso campione sembra ragionevole imputare questo comportamento all'assorbimento di qualche impurezza.

Tabella 3. Confronto fra le proprietà del dispositivo MLG e BLG prima e dopo un trattamento termico (TT) a 100 °C per 1 ora

	MLG prima del TT	MLG dopo 1h a 100°C	BLG prima del TT	BLG dopo 1h a 100°C
μ_e [cm ² /Vs]	2609	3478	3478	4348
μ_h [cm ² /Vs]	5217	2609	2609	609
Punto di Dirac [V]	3.5	1.5	10	-3
Impurezze rilasciate [cm ⁻²]		1.44 E+11		9.34 E+11

Si sono quindi testati i dispositivi realizzati depositando il grafene sopra lo strato di LOL prima che questi fossero esposti ai raggi UV. In questo caso il test non era a quattro elettrodi bensì si è utilizzata una geometria a due elettrodi per le misure di conducibilità. Al fine di poter effettuare un confronto fra questi dispositivi, chiamati LOL-NSG, e i dispositivi NSG tradizionali si è dovuto prendere in considerazione i risultati di test a due elettrodi anche per i device NSG. Si è infatti riscontrato che nel caso di test a due terminali i valori della mobilità potevano risultare inferiori anche di un ordine di grandezza, a causa della resistenza di contatto che non viene considerata in questo tipo di misure.

Tutti e 26 i dispositivi analizzati presentavano lo stesso comportamento: tutti presentano un alto drogaggio di tipo *p*, e il punto di Dirac non appare nel range di tensioni analizzate, risultando così a tensioni superiori ai 40 V (Figura 8), come riportato in [26] e [30]. Tuttavia, non è stato possibile definire se questo importante spostamento fosse da imputare interamente ad un drogaggio dei dispositivi in

seguito alla preparazione con uno strato di resist così spesso, o se fosse dovuto ad una qualche interferenza da parte del resist presente in tale quantità.

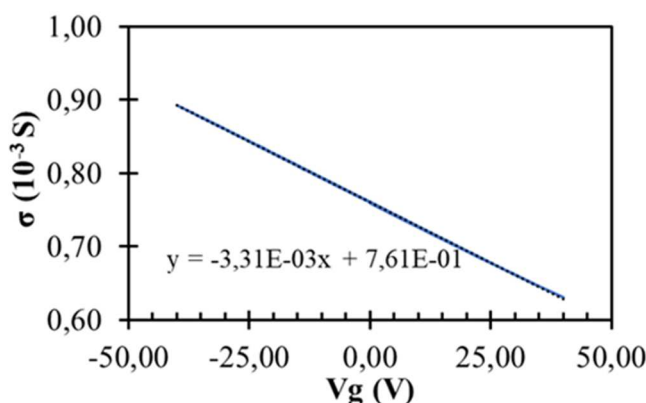


Figura 8. Curva di conducibilità di uno dei dispositivi LOL-NSG. È possibile notare che il punto di Dirac non appare nel range di tensioni della misura, risultando a tensioni maggiori di 40 V.

I valori riportati in questo tipo di dispositivi presentano un'alta dispersione. Questo può essere attribuito al fatto che non si è a conoscenza del numero di piani grafenici di ogni campione a questo stadio della ricerca congiuntamente all'alta influenza della resistenza di contatto. La capacità dello strato di LOL è stata calcolata grazie all'uso di un profilometro superficiale e all'indice di rifrazione riportato nella scheda di sicurezza del materiale e risultava essere pari a $1.7 \cdot 10^{-9} \text{ Fcm}^{-2}$. La capacità totale dei due strati è stata quindi ottenuta assimilandoli a due capacitori in serie ed è risultata essere pari a $1.48 \cdot 10^{-9} \text{ Fcm}^{-2}$. I valori di mobilità dei dispositivi su LOL risultano essere inferiori a quelli dei dispositivi tradizionali, circa di un ordine di grandezza. Nonostante l'alta dispersione si può tuttavia in prima approssimazione effettuare un confronto tra le pendenze delle curve di conducibilità che presentano alcuni valori ricorrenti, riportati nella Tabella 5.

Tabella 4. Valori ricorrenti della pendenza della curva di conducibilità dei dispositivi LOL-NSG

$\left \frac{d\sigma}{dV_g} \right $	1E-8	2E-8	1E-7	2E-7	3E-7	4E-7	6E-7	1E-6	2E-6	3E-6
count	1	1	3	8	2	5	1	2	1	2

A prima vista potrebbe sembrare logico effettuare una classificazione del numero di piani grafenici anche solo approssimativa in funzione dei valori ricorrenti di $\left| \frac{d\sigma}{dV_g} \right|$, tuttavia questa sarebbe fuorviante dal momento che si è notato che anche nel caso di dispositivi con lo stesso numero di piani grafenici il valore della mobilità, e quindi di $\left| \frac{d\sigma}{dV_g} \right|$ può variare in modo considerevole. Un esempio di quanto possa essere difficile approcciarsi a questo aspetto a questo punto della ricerca viene riportato in Figura 9. In essa è possibile vedere tre target grafenici che al microscopio ottico sembrerebbero avere lo stesso spessore, ma che presentano rispettivamente dei valori di $\left| \frac{d\sigma}{dV_g} \right|$ di (a) 3E-6, (b) 4E-7 e (c) 2E-8.

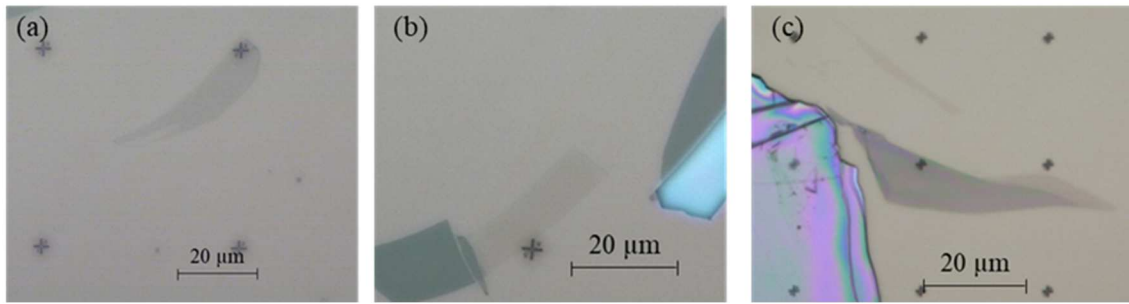


Figura 9. Osservazioni al microscopio ottico dei dispositivi LOL-NSG (a) 7.3, (b) 8.1, (c) 10.5

L'analisi dei risultati dei dispositivi LOL-NSG non è pertanto risultata conclusiva a questo stadio della ricerca. Si potrebbe pensare che il LOL non costituisca un buon strato idrofobo dal momento che non solo non permette di identificare il numero di piani grafenici al microscopio ottico, ma è responsabile di dispositivi che risultano altamente drogati. Tuttavia, affinché queste supposizioni acquistino un fondamento sarebbe necessario svolgere alcuni test aggiuntivi per determinare parametri quali la rugosità dello strato di LOL. È ragionevole pensare, infatti, che questa possa essere irregolare dal momento che viene depositato durante cinque deposizioni di spin coating. Questa irregolarità potrebbe influenzare altamente i valori di mobilità dei dispositivi. Si ritiene che l'ellissometria potrebbe essere una tecnica adatta ad effettuare tali accertamenti, con l'accortezza che lo spessore di LOL potrebbe avere inclusioni tra i vari strati che renderebbero le misure più difficili.

Lo studio si conclude con un'analisi di tutte le criticità riscontrate durante la produzione dei dispositivi sospesi, dal momento che una realizzazione corretta di tali dispositivi non è stata nelle nostre possibilità. In primo luogo, ci si è accorti che la geometria degli elettrodi per condurre test a quattro punti e la geometria dei flakes dei dispositivi non erano compatibili. Questo risultava nel collasso dei dispositivi sottoposti ad esposizione UV, o quantomeno nella non verificabilità della corretta sospensione. Si è quindi deciso di cambiare la geometria degli elettrodi per migliorare la resistenza meccanica dei dispositivi. A tal scopo si è deciso di adottare una geometria per test di misura della conducibilità elettrica a due punti e di aggiungere delle maschere di supporto del dispositivo a lato degli elettrodi di misura (Figura 10). In questo modo riducendo la zona sospesa del grafene e fornendo un adeguato supporto laterale alla struttura si è cercato di stabilizzare il dispositivo, che risultava meno sottoposto a sforzi di flessione.

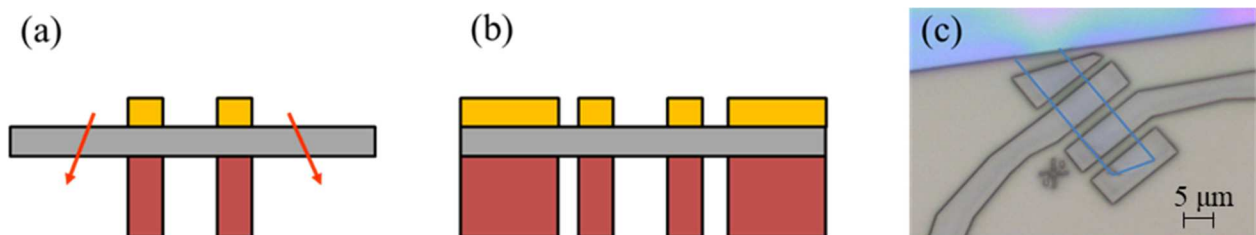


Figura 10. (a) geometria iniziale degli elettrodi che sforzava troppo il dispositivo, (b) nuova geometria con le maschere laterali di supporto, (c) immagine x1000 al microscopio ottico di uno dei dispositivi con la nuova geometria degli elettrodi prima della deposizione (il flake grafenico è stato ricalcato in blu per poterlo riconoscere meglio).

Un secondo problema è stato riscontrato durante l'esposizione dei campioni con la nuova geometria degli elettrodi e consiste nella non completa rimozione dello strato di resist durante l'esposizione UV. I nuovi campioni, realizzati con lo stesso protocollo dei precedenti e sottoposti agli stessi parametri di

esposizione presentavano una superficie con uno strato di resist spaccato da crepe (Figura 11), quando il resist avrebbe dovuto essere completamente rimosso dopo l'esposizione ai raggi UV.

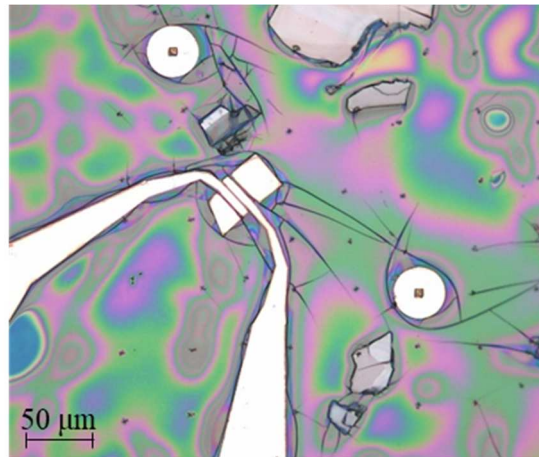


Figura 11. Immagine al microscopio ottico x200 del campione recante lo strato di resist crepato in seguito ad esposizione UV.

Diverse ipotesi sono state addotte come plausibili cause di questo comportamento. Inizialmente si è pensato che il resist avesse potuto degradarsi nel periodo di tempo tra la realizzazione dei dispositivi e l'esposizione UV. Si è quindi provato a realizzare un campione di prova depositando solo LOL su un substrato vergine ed esponendolo ai raggi UV. L'insorgere delle crepe nello strato di resist anche nel campione di prova hanno permesso di stabilire che il lasso di tempo intercorso tra la realizzazione del campione e la sua ultima esposizione UV non fosse responsabile delle crepe, dal momento anche che il campione osservato al microscopio subito dopo le operazioni di lift-off non presentava alcun problema (Figura 12).

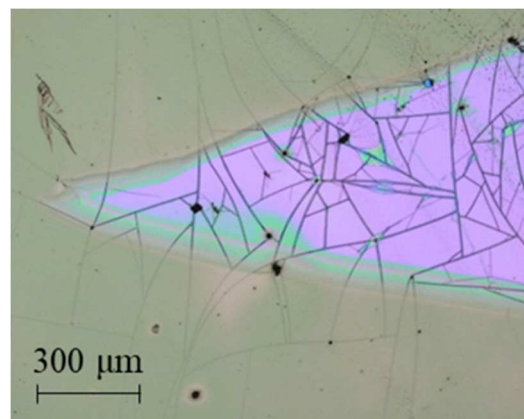


Figura 12. Osservazione al microscopio ottico del campione di prova dopo l'esposizione ai raggi UV.

È possibile notare come la parte esposta ai raggi UV sia diventata rossiccia e sia stata solo in parte attaccata. Si riscontra inoltre l'insorgenza di crepe sia nella parte esposta che in quella non esposta.

Si è passati quindi ad ipotizzare che il tempo di esposizione fosse inadeguato, ovvero troppo lungo o troppo corto. Tuttavia, se il tempo di esposizione fosse stato troppo lungo non vi sarebbero dovute essere tracce residue di resist, e anche il resist sottostante gli elettrodi avrebbe dovuto essere rimosso. Si sono quindi preparati nuovi campioni di prova che sono stati esposti per tempi crescenti. I campioni esposti per 5, 10 e 12 minuti non risultavano completamente attaccati al contrario di quanto succedeva con un

tempo di esposizione di 15 minuti. Tuttavia, si è notato che nel caso di 12 minuti lo strato residuo di resist risultava essere molto sottile. Provando ad esporre nuovamente i campioni precedentemente esposti per 10 e 12 minuti si è notato che la zona esposta durante la prima esposizione risultava completamente disciolta dopo il secondo trattamento, nonostante non tutta l'area fosse stata esposta (Figura 13 e Figura 14).

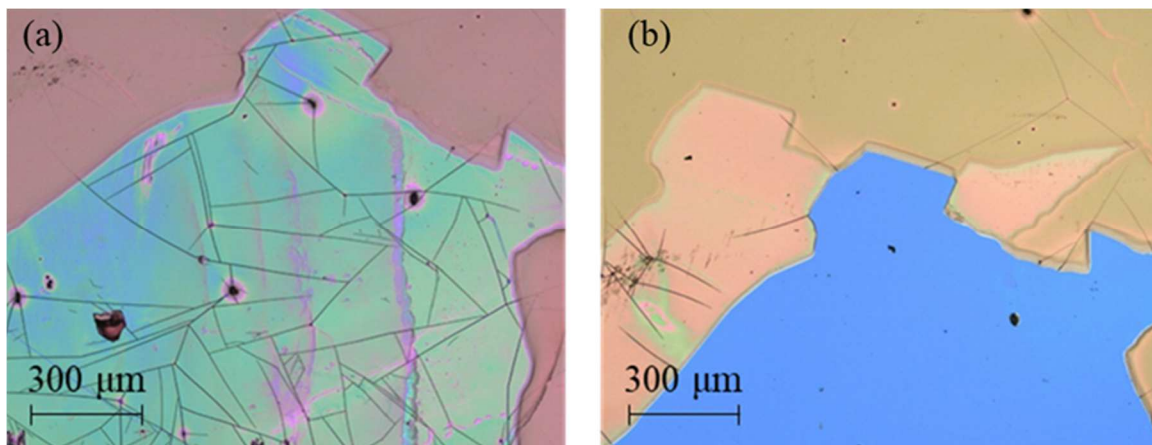


Figura 13. Osservazione al microscopio ottico del campione di prova esposto ai raggi UV per (a) 12 minuti e (b) 12 minuti seguiti da 5 minuti aggiuntivi. In (b) si può vedere come la zona esposta dalla prima maschera sia completamente disciolta, anche nelle zone che non sono state esposte nel secondo procedimento

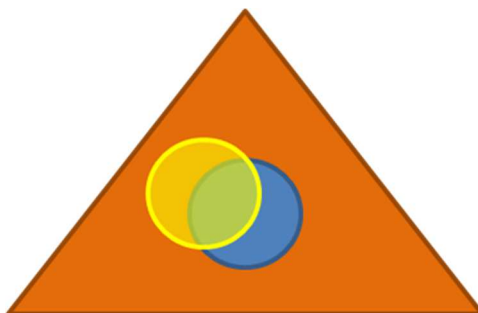


Figura 14. Schema del campione esposto inizialmente per 12 minuti e successivamente per 5 minuti aggiuntivi. La maschera usata per la prima esposizione è disegnata in blu, mentre quella della seconda è gialla. Dopo lo sviluppo del campione il resist sovrastante la zona blu risultava essere completamente rimosso, mentre quello sopra la zona gialla solo parzialmente.

L'effetto del tempo di sviluppo è stato quindi analizzato. Dal momento che durante le esposizioni dei campioni precedenti anche la parte non esposta era stata rimossa con successo dopo un secondo sviluppo, si è tentato di esporre un ultimo campione per 12 minuti e raddoppiare il tempo di sviluppo (Figura 15). Dato il successo di queste tempistiche nella preparazione del campione di prova, si è definito un nuovo protocollo di esposizione: 12 minuti di esposizione ai raggi UV, 2 minuti di sviluppo in lattato di etile e 1 minuto di risciacquo in esano a temperatura ambiente. Dal momento che il tempo di sviluppo sembrerebbe essere più influente che non il tempo di esposizione, abbiamo attribuito questo bisogno di cambiare il protocollo ad una riduzione della sensibilità del resist rispetto alle sue condizioni ottimali.

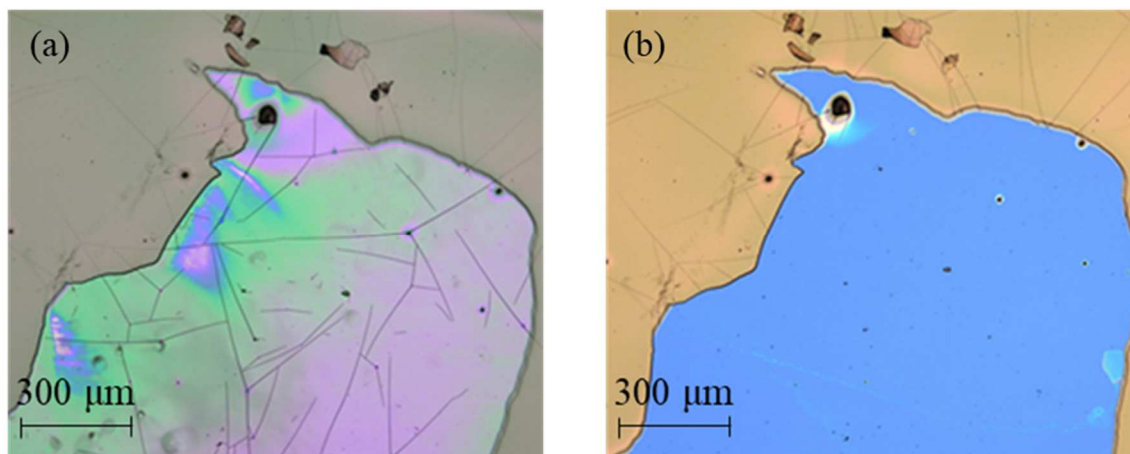


Figura 15. Osservazione al microscopio ottico del campione esposto per 12 minuti (a) dopo il primo sviluppo e (b) dopo il secondo sviluppo. È possibile notare che dopo il secondo sviluppo il resist è completamente rimosso.

Tuttavia, nonostante i campioni di prova risultassero completamente attaccati, l'esposizione del campione con i dispositivi con il nuovo protocollo non ha portato i risultati attesi. Osservando il campione al microscopio ottico si vede che uno strato di resist polimerico rimane presente sulla maggior parte del substrato, rarefacendosi solo in prossimità dei flake di grafite. In prossimità dei dispositivi tuttavia non sempre il resist viene rimosso, e non si riesce ancora a capire se la sospensione sia avvenuta con successo o no. Un esempio di dispositivo quasi privo di resist nei suoi dintorni è riportato in Figura 16. Per capire se la sospensione sia avvenuta o no occorrerebbe svolgere test elettrici.

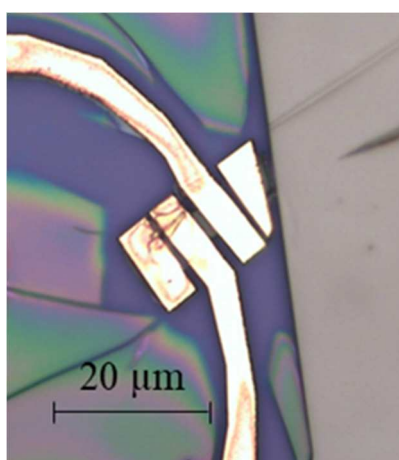


Figura 16. Osservazione al microscopio ottico di uno dei dispositivi dopo essere sottoposto a 12 minuti di raggi UV, 2 minuti in lattato di etile e 1 minuto in esano. Dal contrasto ottico non è possibile capire se il dispositivo sia stato correttamente sospeso o se invece del resist sia rimasto sotto il dispositivo

Durante l'esposizione e il conseguente sviluppo è sorto un altro problema, illustrato in Figura 17. Questo consiste nell'insorgenza di rilievi sulla superficie degli elettrodi. Varie ipotesi sono state prese in considerazione riguardo la causa di questi rilievi, tra cui l'accumulazione di resist solubilizzato dall'esposizione UV. Tuttavia, non avendo potuto determinare la causa di questo effetto si è deciso di non effettuare una nuova esposizione del campione per rimuovere il resist residuo poiché sarebbe potuto risultare in una ulteriore degradazione degli elettrodi, nefasta per eventuali test elettrici.

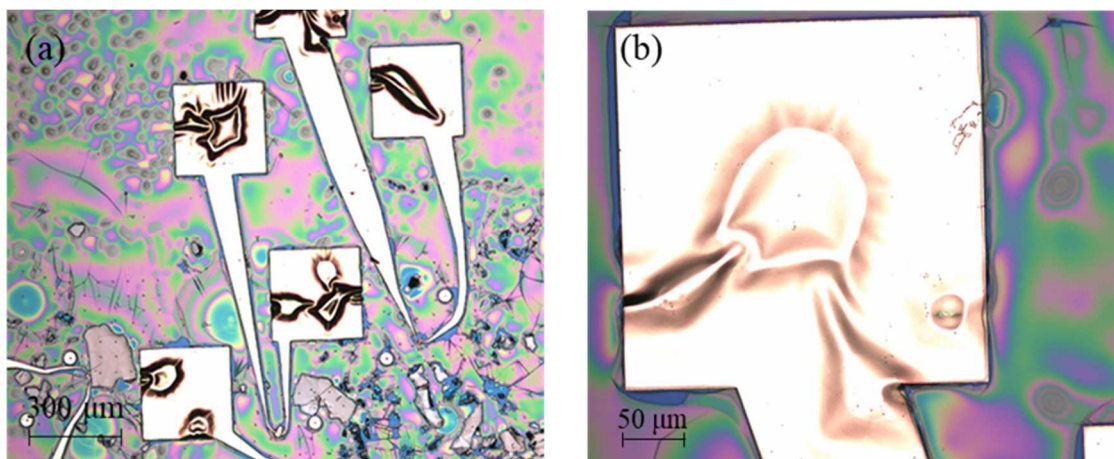


Figura 17. Osservazione al microscopio ottico degli elettrodi dopo essere sottoposti a 12 minuti di raggi UV, 2 minuti in lattato di etile e 1 minuto in esano. (a) È possibile notare che il resist polimerico rimane diffuso sulla superficie del campione e che gli elettrodi presentano dei rilievi. (b) dettaglio di uno degli elettrodi accartocciati

Per concludere, in questo studio sono stati realizzati due tipi di dispositivi a base grafene con diverso strato idrofobico. In un primo momento si sono analizzati i dispositivi tradizionali facendo un confronto tra dispositivi monolayer e dispositivi bilayer, quindi si è proceduto con la realizzazione e la caratterizzazione di dispositivi su uno strato micrometrico di LOL. Questi rappresentavano dei dispositivi intermedi durante la realizzazione di dispositivi sospesi, la cui realizzazione purtroppo non è stata portata a termine con successo. Si è cercato di effettuare un confronto tra i due tipi di dispositivi, mettendone in evidenza tuttavia tutte le limitazioni dovute al caso, quindi i problemi sorti durante la realizzazione dei dispositivi sospesi sono stati illustrati.

Lo studio di queste due categorie di dispositivi ha permesso di evidenziare alcune delle proprietà del grafene che interessano maggiormente il campo dell'elettronica. Nonostante la realizzazione dei dispositivi sospesi non abbia avuto esito positivo, ha permesso di effettuare uno studio comparativo tra i dispositivi su LOL e quelli tradizionali. Si è pertanto notato che sebbene i dispositivi su LOL siano meno prestazionali di quelli tradizionali, presentano dei valori equiparabili a quelli tradizionali di media qualità e sono promettenti nel caso di una sospensione completata con successo. Riteniamo pertanto che sia importante portare avanti la ricerca per ottimizzare il processo di produzione di questo tipo di dispositivi la cui architettura rivestirà un ruolo di fondamentale importanza nella ricerca delle proprietà elettroniche del grafene.

Table of contents

Introduction	1
1. Graphene	3
1.1 History	3
1.2 Properties	4
1.2.1 Band structure and energy diagram	6
1.2.2 Integer quantum hall effect (IQHE)	7
1.2.3 Raman spectra	8
1.3 Synthesis of graphene	10
1.4 Applications	13
2. MOS FET	15
2.1 Origins of transistors	15
2.2 Working principles	17
2.2.1 Accumulation operation	19
2.2.2 Depletion regime	20
2.2.3 Inversion regime	20
2.2.4 Current in the MOS transistor	21
3. Experimental methods	23
3.1 Preparation of the mechanically exfoliated NSG samples	23
3.1.1 Preparation of the substrate	23
3.1.2 Deposition of graphene	23
3.1.3 Etching of the samples by Electron Beam Lithography (EBL)	25
3.2 Preparation of the mechanically exfoliated SG samples	31
3.3 Electrical measurements	34
3.3.1 Four-terminal measurements	34
3.3.2 Two-terminal measurement	35
4. Results and discussion	37
4.1 NSG standard devices	37
4.2 LOL-NSG devices	47
4.3 SG devices	51
5. Conclusions	59
List of acronyms	63
References	67
Supporting information 1. Solubility of three kind of resists	73
Supporting information 2. Infographic of the mechanically exfoliated NSG devices	74
Supporting information 3. Optical microscopy images of the LOL-NSG devices before the realization of the electrodes	77

Supporting information 4. Infographic of the mechanically exfoliated LOL-NSG devices	83
Supporting information 5. Study of the exposure time	95
Acknowledgements	97
Ringraziamenti finali	99

Introduction

Ever since its discovery back in 2004 [1] [2] [3] [4] graphene has attracted a lot of attention for its set of peculiar properties, which were and still are very promising for the electronic industry. The rush for the “miracle material” exploded in the early 2000s, but more than ten years after the initial excitement, research is still stable and novel exciting properties are continually confirmed or discovered [5] [6] [7].

Particularly interesting for the electronic industry are properties related to electronic transport, a field in which graphene seems to still hold the leader position [8]. Graphene possesses a really high mobility at room temperature [9], a large surface area per unit mass and can show ballistic transport in the right conditions [10] [11]. Ambipolar field effect can be observable and a tuneable band gap can be opened if a suitable electric field is applied to bilayer graphene. One of the peculiarities of this two-dimensional (2-D) material is the fact that its properties are strictly related to its number of layers. Monolayer graphene samples (MLG) and samples with an odd number of layers show a linear energy dispersion, whereas bilayers (BLG) and even-numbered-layers samples show a parabolic energy dispersion. This is called parity effect and is one of the particularities of this amazing material [12].

All of these characteristics make graphene a perfect candidate for the realization of high profile devices such as field effect transistors. Although there has been a lot of research going on, an effective method to produce transistors at a large scale isn't yet available and its properties aren't fully understood yet. Peculiarities such as integer hall effect have already been investigated and understood [13], whereas others like superconductivity are still under investigation [14].

In this work we attempt to study the electronic transport properties of graphene-based devices by differentiating between conventional non-suspended graphene devices and innovative suspended devices in which the properties are expected to greatly increase [10]. The structure of this work is as follows. First, a theoretical background of graphene is drawn in chapter 1. In it the history of the material, its structure, its properties and the fabrication methods are addressed. We then continue in chapter 2 to address the main features of metal oxide semiconductor field-effect-transistors (MOSFETs) starting from the history of their discovery to the principles behind their operation. Experimental methods of fabrication of the non-suspended and suspended devices are then addressed in chapter 3, whereas the results and discussion are left for chapter 4, differentiating the different kinds of devices realized.

1. Graphene

1.1 History

Carbon, the basic element for all kinds of life on earth, can be found in nature in several forms. The most commonly known forms are graphite, which is a stack of atomic plans of carbon atoms arranged in a hexagonal lattice (in blue in Figure 1.1), and diamond, a metastable three-dimensional form. Another commonly known form of molecular carbon is fullerenes, also known as buckyballs, which consist of a sheet of carbon atoms rolled into a sphere-like shape (in green in Figure 1.1). They were discovered in 1985 by Sir Harold W. Kroto, Richard. E. Smalley and Robert F. Curl, Jr., which were then awarded the Nobel Prize in Chemistry in 1996 [15]. Carbon nanotubes (CNTs) completed the series of allotropic forms of carbon known to scientists until the early 2000s, when a new revolutionary material was discovered. CNTs were discovered in 1991 by Sumio Iijima and consist of a single or multiple sheets of carbon atoms rolled into a cylindrical shape. Depending on the number of concentric cylinders CNTs are called single-walled (SWNTs) and multi-walled carbon nanotubes (MWNTs) [16].

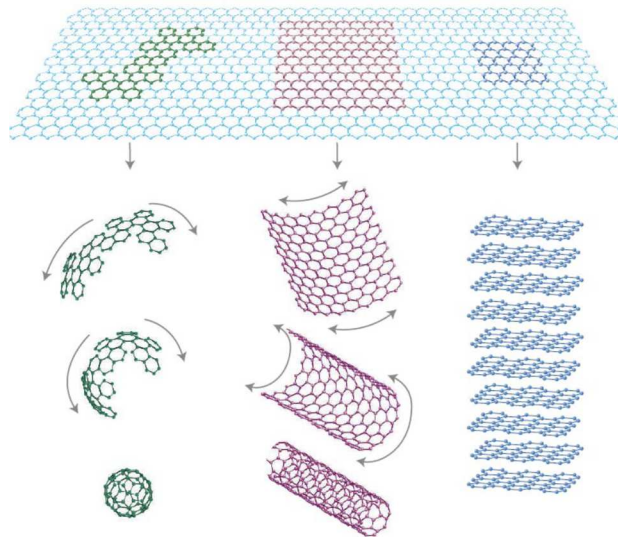


Figure 1.1. Different forms of carbon derived by a single sheet of carbon atoms: from the left, it is possible to obtain a fullerene if it is sphere shaped (in green), a nanotube if it is rolled in a cylindrical shape (in red) and graphite if the layers are stacked (in blue) [2].

It was 2010 when Andre Geim and Kevin Novoselov were awarded the Nobel Prize in Physics "for ground-breaking experiments regarding the two-dimensional material graphene" [1]. Although the existence of such a two-dimensional material had been theorized in 1947 by Philip R. Wallace, it was then regarded as a purely scholar example for calculations in solid state physics [2]. As a matter of fact, Lev Landau and Rudolf Peierls in the 1930s had stated than the existence of 2-D materials was impossible because of their thermodynamic instability which led to discontinuity at thickness of several nanometres [3]. The thermal fluctuations on low-dimensional crystal lattices were supposed to result in atomic displacements comparable to interatomic distances [17]. This knowledge was supported by observations such as the decreasing of the melting temperature of thin films with the decreasing of their thickness, but was proven wrong in 2004 when graphene, the first of a long series of 2-D materials, was discovered by Geim and Novoselov [3].

Graphene consists of a flat monolayer of carbon atoms arranged in a 2-D honeycomb lattice with a carbon-carbon bond length of 0.142 nm [7]. The method with which it was first obtained is called Scotch

Tape technique and consists on mechanical exfoliation of a highly oriented pyrolytic graphite flake thanks to multiple and successive peeling [2]. Mechanical cleavage was known as a way to prepare samples for Scanning Tunnelling Microscopy and optical studies, but it was first used specifically as a way to cleave graphite in the 1990s by Ohashi et al [18]. In their study of thin graphite flakes they measured the electrical resistivity as a function of the thickness, reaching ~ 30 layers in the thinnest one [19]. Although this technique may seem outdated and unfit to scientific works, it is still currently used in the research field, and in this work, as it is the one which yields the samples of higher quality both structurally and electronically [6].

After its discovery in 2004 and the following success of measuring its electronic properties in 2005 always by the Manchester group of Geim and Novoselov, graphene became the centre of many attentions due to its peculiar properties and many potential applications [5]. This can be seen in Figure 1.2, where the number of publications about graphene is shown to grow exponentially since the year 2000.

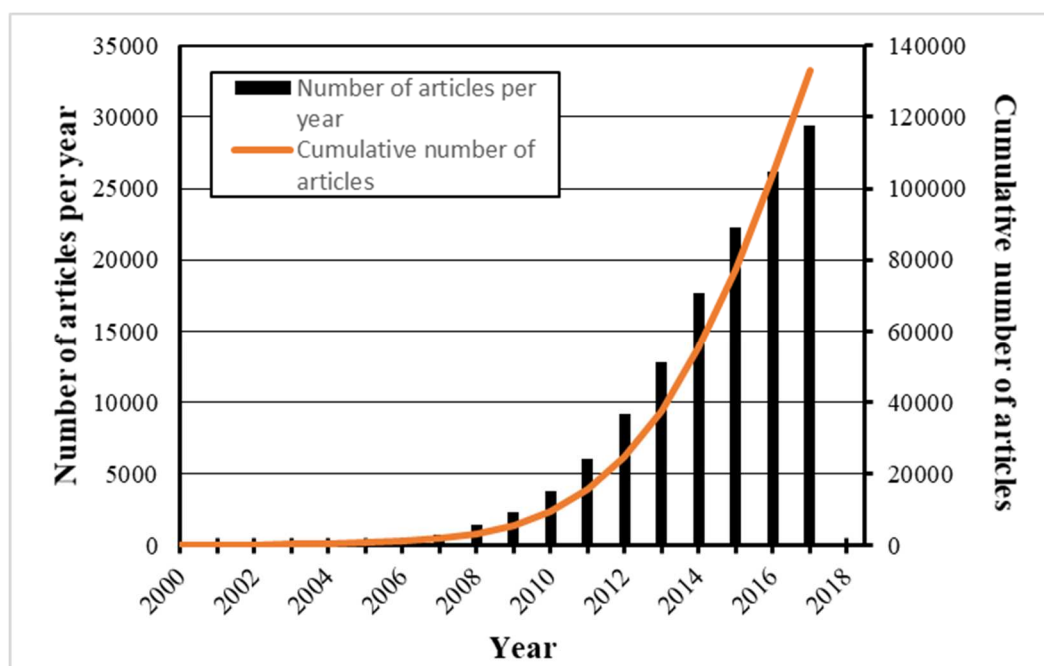


Figure 1.2. Evolution of the number of publications on graphene since the year 2000. The number of articles per year has been taken from the Web of Science website, by selecting only the articles having “graphene” as a topic (data updated in February 2018).

The interest raised by graphene in the scientific community arises from several of its peculiar properties and the vast amount of different possible applications: from the field of the microelectronics to the reinforced composites. Its main properties and the methods available to produce graphene will be now analysed to better contextualize this peculiar material.

1.2 Properties

Graphene is composed of a single graphitic layer, nominally a single layer of carbon atoms hybridized sp^2 arranged in a honeycomb lattice. The lattice is then hexagonal, as in graphite, and has a two-atoms basis, whose sites are called A and B. This can be also seen as two triangular sublattices interpenetrating each other and related by inversion symmetry [19] (Figure 1.3).

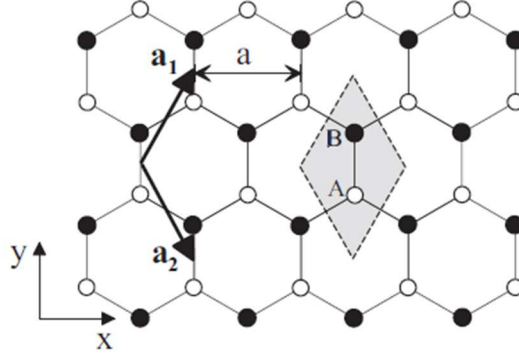


Figure 1.3. Honeycomb crystal structure of monolayer graphene. The shaded figure represents the unit cell which contains two atoms: A atoms (in white) and B atoms (in black) which give rise to two sublattices [20].

The reciprocal lattice of graphene is a hexagonal Bravais lattice too, as shown in Figure 1.4. The first Brillouin zone, defined as the smallest volume enclosed by planes cutting perpendicularly in half the reciprocal lattice vectors drawn by the origin, is hexagonal. Between the six corners of the Brillouin zone just two are inequivalent, meaning they cannot be connected using a reciprocal lattice vector. They are usually indicated by K_+ and K_- (in red and green in Figure 1.4) and can be called ‘valleys’ borrowing a term from the semiconductor physics. The corners of the Brillouin zone of graphene are generally called ‘Dirac points’ because of the behaviour of the electrons in this zone, as will be later explained. Another interesting kind of point of the Brillouin zone is the M point (in yellow in Figure 1.4), which resides at the centre of each rectangular face, and where another singularity occurs. The van Hove singularity sees a divergence of the density of states and should play an important role in a predicted superconductivity in graphene [21]. Following theoretical assumptions, electrons should condense into a superconducting state in MLG, either by doping, placing it on superconducting materials, or intrinsically. Recent studies have reported successful results on doping induced and proximity induced superconductivity, the latter being with electron-doped cuprate semiconductors [14]. However, up to now the intrinsic superconductivity has not yet been observed.

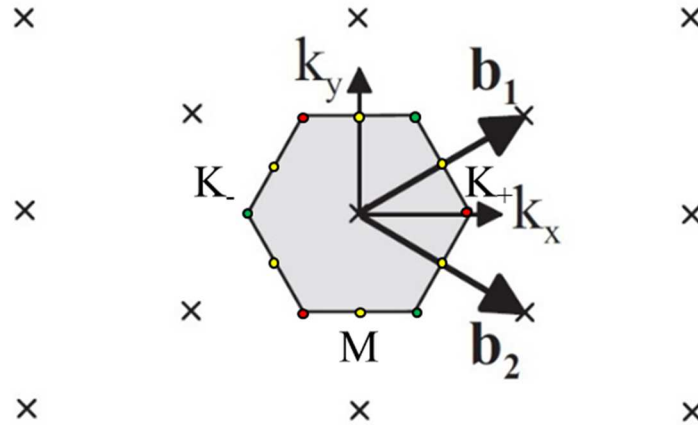


Figure 1.4. Reciprocal lattice of graphene. The crosses are the reciprocal lattice points whereas b_1 and b_2 are the two primitive vectors of the reciprocal lattice. K_+ and K_- points are respectively indicated by red and green dots, M points in yellow dots. The shaded area represents the Brillouin zone (modified from [20]).

Graphene presents a set of very notable properties. As a matter of fact, it possesses one of the highest Young Modulus amongst known materials, about 1 TPa [22], a theoretical specific surface area of about 2600 m²/g, a thermal conductivity of about 3000 W/mK and 2.3% of absorption of visible light [7].

Unfortunately, these properties are theoretical or shown only when graphene is isolated or is a single crystal. Whenever graphene is put in contact with other materials or used in devices these properties decrease, though they remain high values compared to other conventional materials. This is mainly due to the decrease of its superficial area and to the scattering phenomena that appear at grain boundaries of most graphene flakes, as it is the case for polycrystalline graphene grown by Chemical Vapour Deposition (CVD) on copper substrates, and at the interface between graphene and the substrate [7]. For these reasons, extensive researches are being conducted on both supported and suspended graphene to better understand the role of the substrate in the lowering of both thermal [23], [24], [25] and electronical properties [10], [26].

1.2.1 Band structure and energy diagram

Graphene is a zero-gap semiconductor and presents ambipolar electric field effect. This means that the charge carriers can be tuned between holes and electrons at high concentrations at room temperature by applying a suitable voltage [17], [27]. Its particularity resides in the fact that the mobility depends only weakly from the temperature and remains high even at high carrier density, thus indicating a ballistic transport on the submicron scale [8]. Ballistic electronic transport has been reported in bilayer devices in studies such as [28] and [29], and near ballistic transport has been recorded in suspended graphene devices in [11].

The energy dispersion of graphene can be described with a Dirac-like Hamiltonian near the Dirac points in monolayer graphene, resulting in a linear energy dispersion. This means that electrons near these points move at a constant speed relatable to the speed of light c , called Fermi velocity $v_F \approx c/300$ [19], behave like relativistic particles and when interacting with the lattice give rise to massless Dirac fermions, electrons that have lost their rest mass [22].

In the case of bilayer graphene, instead, the energy dispersion assumes a parabolic shape (Figure 1.5). This is due to the fact that in bilayer graphene we have quadratic terms on the off-diagonal of the low-energy Hamiltonian instead of the linear terms in the Dirac-like Hamiltonian of monolayer graphene. This parity effect can be seen also in few-layer graphene (FLG). If the number of layers is odd the energy dispersion will be linear, whereas it will be parabolic in the case of even layer number [12], [8]. The resulting quasiparticles are then chiral, as in the monolayer case, but have a finite mass $m \approx 0.05m_0$ [17], with m_0 being the effective mass.

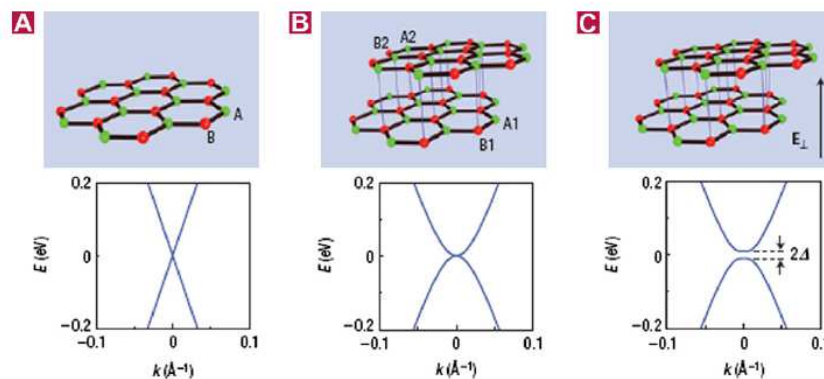


Figure 1.5. Energy dispersion relations calculated for (A) monolayer graphene and (B) bilayer graphene in low energy regimes. The valence and conduction band cross at the six corners of the Brillouin zone and the Fermi level is located at zero energy level. (C) If a perpendicular electric field is applied a tuneable band gap opens in bilayer graphene [7].

The low energy band structure of monolayer graphene in the vicinity of the first Brillouin zone can be seen in Figure 1.6. In it we can see the asymmetry between the valence and conduction band in the vicinity of the Γ point, which indicates the centre of the Brillouin zone. The fact that the Dirac cones coincide with the corners of the Brillouin zone in graphene is due to the crystal point symmetry [9]

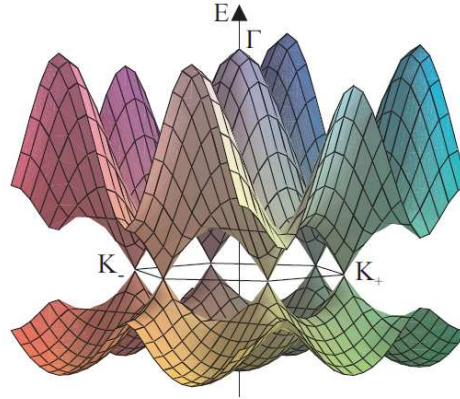


Figure 1.6. Low energy band structure of monolayer graphene in the vicinity of the first Brillouin zone [20].

In graphene the electrons do not possess a spin but a degree of freedom in the relative amplitude of the Bloch function on the two sublattices. This is called pseudospin. They are also chiral, meaning the direction of the pseudospin is related to the one of the electronic momentum. This puts a constraint on the scattering process: the pseudospin is conserved upon scattering if the potential cannot disrupt the A-B symmetry, causing anisotropy and absence of backscattering in the monolayer case.

Furthermore, due to its honeycomb lattice, graphene possesses two different kinds of edges, armchair and zig-zag (Figure 1.7), which possess different characteristics and electronic band structures [8]. While the armchair edges show no carriers at the Dirac point, like bulk graphite, a singular density of states is localized at zigzag edges [30].

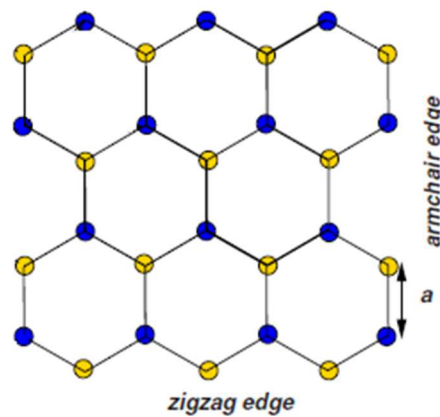


Figure 1.7. Zigzag and armchair edges in honeycomb lattice [8].

1.2.2 Integer quantum hall effect (IQHE)

Impurities have a very important role in the mobility of the carriers as they can act as scattering points, thus limiting the conductivity of the samples. In low dimensional materials, however, they become

responsible for a peculiar behaviour known as Integer Quantum Hall Effect [8], [13], [22]. In such cases, the impurities cause a break of the degeneracy and transform many quantum states from extended to localised at the edge of a band. The population of localised levels not participating in the conductivity, it is possible to observe the rise of plateaux in the conductivity as a function of the density of levels (Figure 1.8).

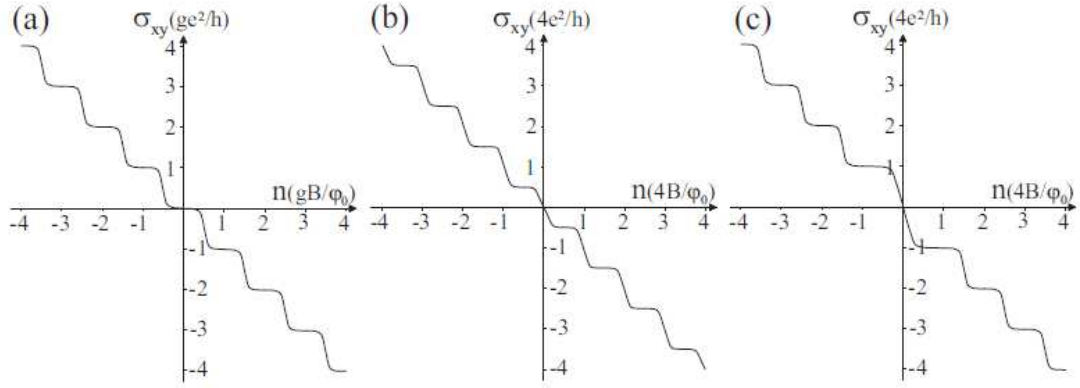


Figure 1.8. Density dependence of the conductivity σ_{xy} due to integer quantum Hall effect. In (a) a conventional 2-D semiconductor system, in (b) monolayer graphene, in (c) bilayer graphene. On the x-axis the carrier density has steps of gB/ϕ where g is the additional system degeneracy, B is the magnitude of the magnetic field and ϕ the flux quantum [20].

In the case of monolayer graphene, each plateau arises from a fourfold degeneracy of Landau levels, due to spin degeneracy and valleys degeneracy. The plateaux then have a step of $4e^2/h$ and assume values of half integer instead of integer values of $4e^2/h$ because of the fourfold degenerate landau level fixed at zero energy [27], [31]. The conductivity σ_{xy} then answers to the equation (1.1)

$$\sigma_{xy} = \pm \frac{1}{2} (2N + 1) \left(\frac{4e^2}{h} \right) \quad (1.1)$$

Where h is the Planck constant, equal to $6.626 \times 10^{-34} \text{ m}^2 \text{ kg s}^{-1}$, e is the elementary charge, equal to $1.60 \times 10^{-19} \text{ C}$, where N is an integer number. In the case of bilayer graphene there is one additional degeneracy to take into account, the one of the zero-energy levels. At zero-energy one has an eight-fold degeneracy which causes the step to be of $8e^2/h$, thus forcing the conductivity to assume integer values as can be seen in Figure 1.8. This additional degeneracy rises from the coupling of the two layers which modifies the nature of the massless Dirac fermions into other quasiparticles [32].

1.2.3 Raman spectra

Graphene samples can now be obtained quite easily, as will be later explained in paragraph 1.3, but the identification of the number of layers can still be quite difficult. Historically, the techniques used to distinguish between different thicknesses were the optical contrast in Optical Microscope (OM) observations, the Atomic Force Microscopy (AFM), but only if the film contained wrinkles or folds, and the Transmission Electron Microscopy (TEM). Raman spectroscopy emerged as a fast and non-destructive technique which can give both structural and electronic information with high precision [22], [33]. It allows univocal identification of the orientation and number of layers of the specimens [34] other than characterisation of doping, edges, grain boundaries and disorder amongst others [35]. The presence of both structural and electronics information in the spectra derives from the gapless nature of graphene, which make all incident wavelengths resonant [33].

An example of Raman spectra of graphite and graphene can be seen in Figure 1.9. It is possible to distinguish two main peaks which are always visible in graphite samples. Those are historically called G peak, at $\sim 1580 \text{ cm}^{-1}$, and G' band at $\sim 2700 \text{ cm}^{-1}$ if a laser of 514 nm is used. Though these two have a similar name, they are not related. The G peak is a primary in-plane vibrational mode of high frequency phonons near Γ (Figure 1.10), whereas G', also known as 2D [33], is related to the D peak and arises from second order zone-boundary scattering phonons [36].

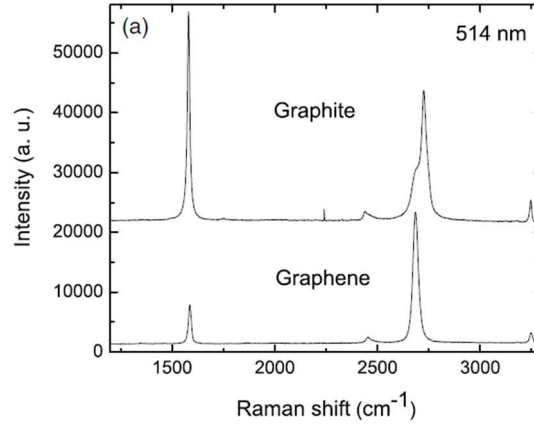


Figure 1.9. Comparison of the Raman spectra of Graphite and Graphene at 514 nm. The two spectra are scaled in order to have a similar height of the $\sim 2700 \text{ cm}^{-1}$ peak [34].

The D peak originates from one inelastic and one elastic scattering processes of transversal optical (TO) phonons near the edges of the Brillouin zone at K, whereas in the second order G' band there are two inelastic processes. The G' peak arises when an electron is excited into the conduction band and recombines with a hole in the valence band after a two phonon scattering process. The conservation of energy and momentum for the two intermediate states makes it a double resonance intra-valley scattering process which connects the K_+ and K_- points.

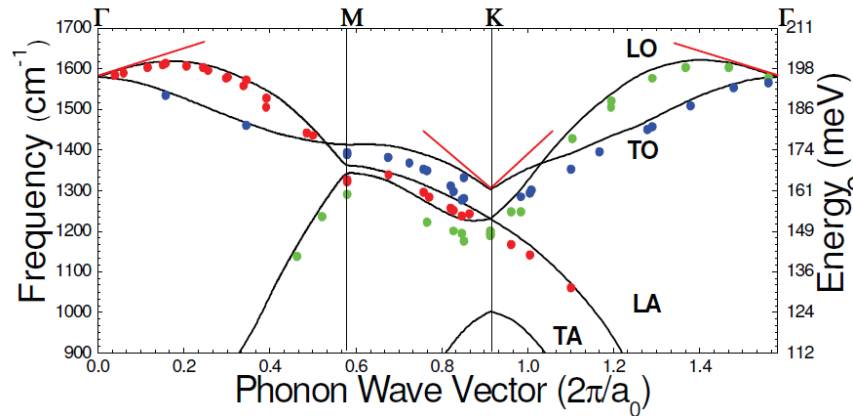


Figure 1.10. Dispersion of in-plane phonon modes in graphene in the Raman spectra range of frequency and energy [33].

As the number of layers of graphene increases, the G' peak modifies its shape, full width at half maximum (FWHM) and position because of the changes in the interlayers forces of AB stacked graphene (Figure 1.11). This allows one to calculate the number of layers and the substrate thickness [37] from the position of the peak and the ratio of the peak intensities $I_{G'}/I_G$ [34] [35].

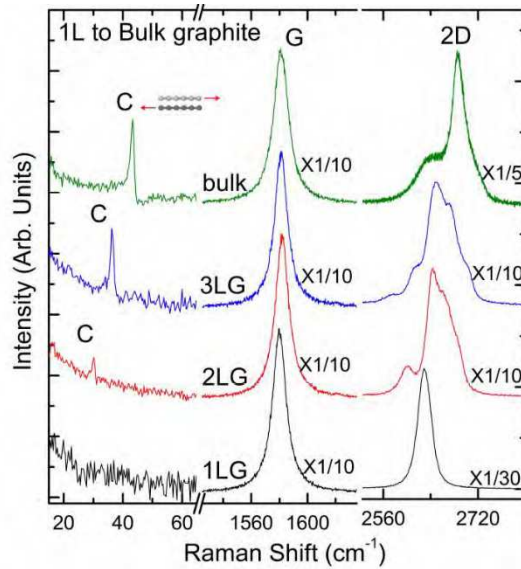


Figure 1.11. Evolution of the Raman spectra of graphene as the number of layer increases [22].

1.3 Synthesis of graphene

Depending on the size and quality required, graphene can be obtained in several different ways [7]. Generally speaking, those methods are divided into two main categories based on the chosen approach (Figure 1.12): we call top-down the techniques that start from graphite specimen and try to separate the single monolayers, whereas we call bottom-up those techniques that start from carbon precursors and led to the formation of graphitic layers [19]. In the following pages a synthetic and not exhaustive review of the most common techniques will be performed.

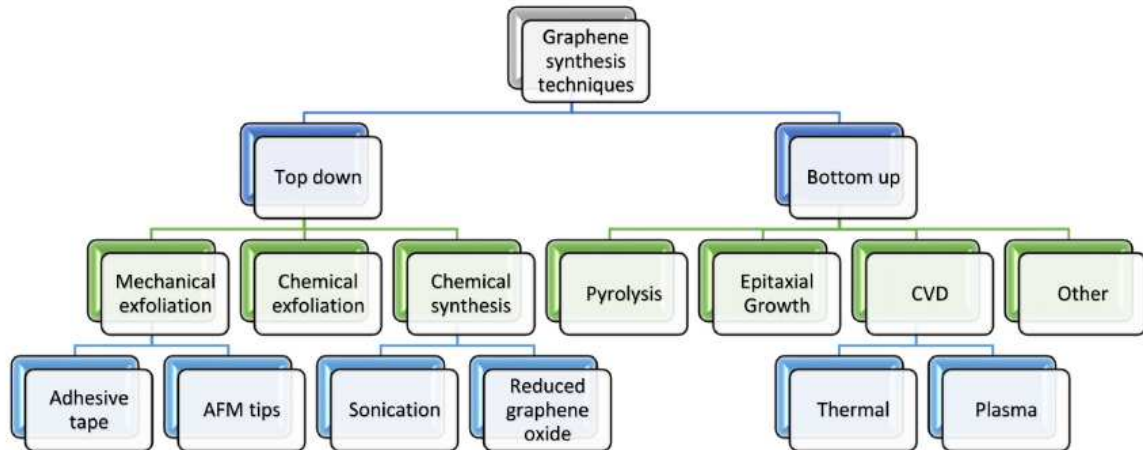


Figure 1.12. Overview of the different approaches available to synthesize graphene [38].

The top down approach is historically the first to have been discovered. It yields samples of high purity but cannot always be scaled up to industrial applications. In the top-down categories we can find the following techniques:

- *Mechanical exfoliation.* Mechanical exfoliation can be performed in different ways, namely by using an adhesive tape (Figure 1.13 a), by ultrasonication [38], by photoexfoliation (Figure

1.13 b) [22], [39]. The successive peelings of a graphite flake with an adhesive tape is the most widely known method and the one used by Geim and Novoselov to first isolate graphene in 2004 [3]. The so-called Scotch tape technique is unfortunately not scalable, since it is essentially a manual operation, but is the cheapest and easiest method to obtain samples of high quality and purity. Usually an observation at the OM or a Raman Analysis is necessary to identify the flakes of graphene in the sample [38] [40]. The mechanical exfoliation by tape technique is the method used to obtain monolayer graphene in this study.

- *Chemical Exfoliation.* The chemical exfoliation of graphite consists in two successive steps. Firstly, graphite is added in a colloidal suspension to weaken the van der Waals bonds between the various sheets and to form GICs (Graphite Intercalated Compounds), then the GICs are exfoliated by heating or sonication to obtain graphene (Figure 1.13 c) [38].

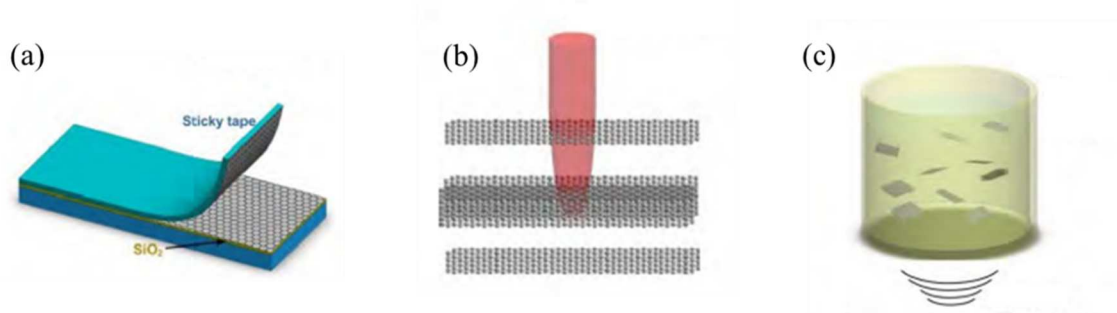


Figure 1.13. Comparison of three different exfoliation methods to obtain graphene: (a) mechanical exfoliation by adhesive tape, (b) photoexfoliation, (c) chemical exfoliation. During mechanical exfoliation an adhesive tape is used to exfoliate graphite, whereas a laser beam is used in photoexfoliation. During chemical exfoliation a colloidal suspension undertakes ultrasonication [22].

- *Reduction of Graphite Oxide (GO, Figure 1.14).* GO is usually prepared by graphite oxidation thanks to agents including concentrated sulphuric acid, nitric acid and potassium permanganate, based on the Hummers method. Once graphite oxide is obtained, exfoliation can be easily performed in water thanks to its hydrophilicity which yields a stable dispersion. We then obtain graphene oxide, which can be reduced thanks to chemical agents like hydrazine, but also more environmental-friendly agents like vitamin C [41], electrochemical reduction, thermal reduction [38] [7], or UV irradiation.

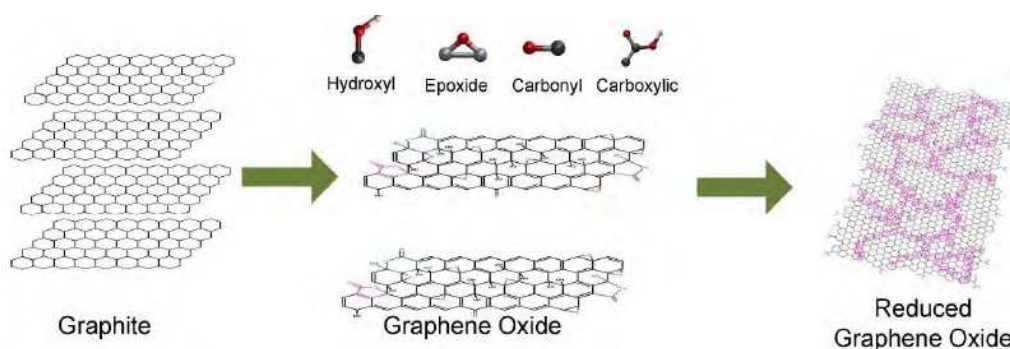


Figure 1.14. Synthesis of graphene by oxidizing graphite, exfoliating the graphite oxide to graphene oxide and then reducing it [22].

Between the bottom-up techniques the most common ones are:

- *Chemical Vapour Deposition (CVD*, Figure 1.15). CVD has been used to synthesize few-layers graphene on metal substrates since 2006 [7] and has since grown to become one of the most promising techniques for large scale production of graphene films. CVD techniques include thermal CVD and plasma-enhanced CVD (PECVD), where the temperature of the process can be cooled down due to the presence of the plasma. In thermal CVD, carbon is deposited on transition metals substrates, such as copper or nickel, exposed to hydrocarbon gases and graphene films are obtained through the precipitation of the diffused carbon atoms. Nickel was the first substrate on which graphene growth was attempted, but other substrates are reported in literature such as platinum on which FLG can be grown [42]. Nonetheless, copper appears to be the most efficient one because monolayers of graphene can be grown on it and because of the self-limiting growth of graphene on it [38] [39]. The graphene films can then be transferred to other substrates after etching the metal, thus obtaining high quality films. Substitutional dopants can also be introduced in the films by tuning the gases during the growth process. Such a technique presents nonetheless several drawbacks such as the difficulty to control the number of layers, the folding of the film and the growth of secondary crystals [40].

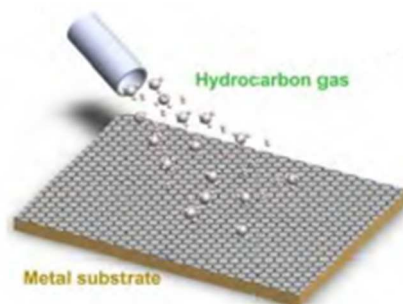


Figure 1.15. Illustrative setup for CVD of graphene [22].

- *Thermal decomposition of SiC* (Figure 1.16). Graphene can also be obtained in top of SiC substrates, by annealing the substrate under Ultra High Vacuum (UHV) at ~ 1300 °C. During the annealing of the substrate the silicon atoms sublime thus allowing the carbon atoms to rearrange itself into few-layer graphene depending on the time and temperature of the process. The graphene thus obtained grows as an epitaxial layer on the Sic substrate, but it is a very expensive process [38]. This technique is mostly used in the semiconductor industry because it requires no transfer of the graphene film after its growth [7] and the graphene islands can be patterned with standard lithography methods [40].

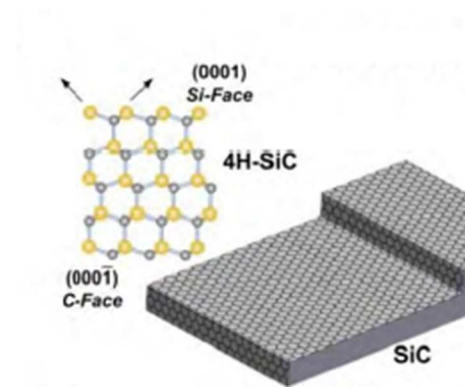


Figure 1.16. Schematic of the graphene growth on SiC substrate [22].

1.4 Applications

Graphene has attracted the attention of many fields due to its peculiar properties. These range from high frequency electronics to flexible and wearable devices, from optoelectronics to energy storage and generation, from composites to biomedical applications (Figure 1.17).



Figure 1.17. Overview of some of the possible graphene applications in different fields of research [22].

The main potential fields of applications related to graphene main properties are summarized in Table 1.1. It is possible to see that its applications mainly involve electronics due to its high transport properties. Its possible use as a transparent electrode or as a component for displays and touch screens has raised a lot of interest in the scientific community. This is determined by the need to find an alternative to indium tin oxide (ITO) which is brittle and presents high costs of production. Graphene presents high thermal and electrical conductivity, high chemical stability, high elasticity, and low optical absorbance. All of

these characteristics and the abundance of carbon make it a suitable alternative to ITO. Nevertheless, graphene properties are now being tested mainly in transistor devices to better understand its behaviour in different situations.

The interest in graphene, however, does not involve only electronic applications. Its use in chemical sensors, or as a filler in composites for high-performance sport equipment are just some of its possible applications. A recent development [43] is the discovery that a two-layer graphene film grown by epitaxy on a SiC substrate can undergo a reversible phase transformation to a diamond-like film at room temperature after nano-indentation. This could allow some openings for ultrahard coating activated by pressure and force-controlled dissipation switches.

Table 1.1. Summary of the applications and technologies enabled by different properties of graphene (modified from [22]).

Feature	Possible applications and technologies
Atomic thickness	Flexible devices, thin and flexible electronic components, portable devices
Foldable material	Novel engineered materials
2-D material	Chemical/biological sensors
Solution-processable	Novel composite and functional materials
High carrier mobility	Ultra-high frequency electronic devices
Optical absorption	Optoelectronic and thermoelectric devices, photodetectors
Field effect sensitivity	Highly sensitive transducers
High intrinsic capacitance and specific surface area	Supercapacitors
Photovoltaic effect, photocatalytic effect	Energy conversion, harvesting and self-powered devices
Theoretically predicted “chiral superconductivity”	High T_c superconductors
Dirac fermions	Valleytronics

2. MOS FET

Most engineers have encountered at some point of their academic career Moore's Law (Figure 2.1), stating that the number of transistors per chip roughly doubles every two years [44]. Originally Moore's statement was that their count would double every year, but it was later revised into the now common formulation. Sometimes a period of 18 months for the performance to double is quoted, but this is to be attributed to Intel executive David House rather than Intel co-founder Gordon E. Moore [45].

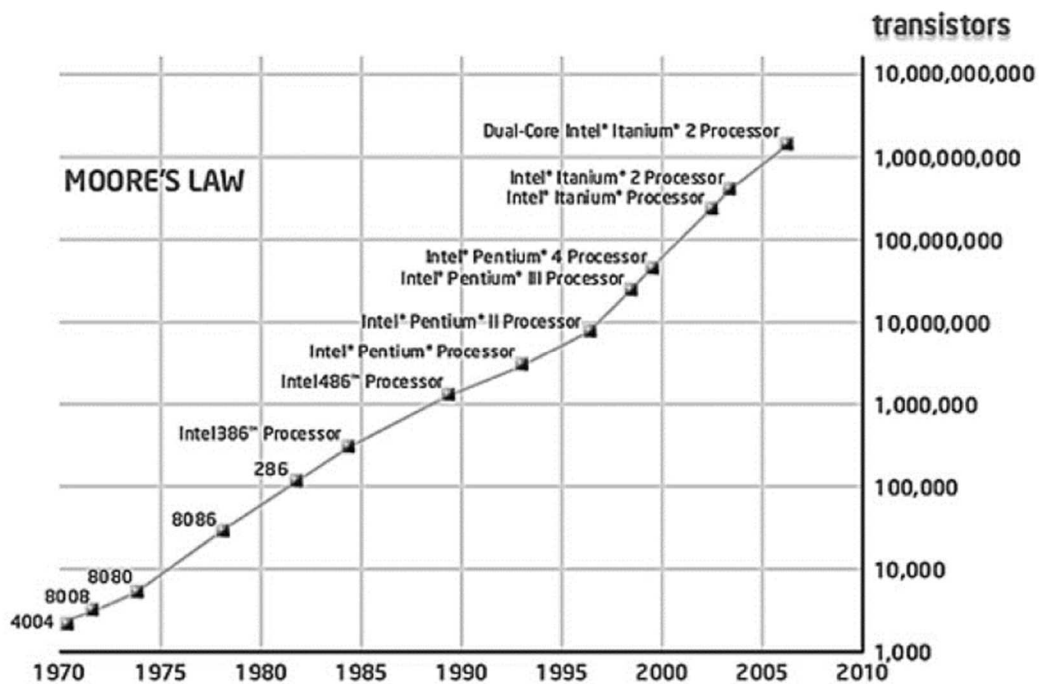


Figure 2.1. Representation of Moore's law, the transistor count is plotted against its year of introduction. The y axis is logarithmic so the law results to be exponential [46].

This exponential growth was determined by the miniaturization of the transistor size which led to transistors being almost omnipresent in everyday life. Metal-Oxide-Semiconductor Field-Effect-Transistors (MOSFETs) can be found in every digital circuit: thought they were first used in computers, they are now present in a variety of applications from digital wristwatches to console gaming, from communication devices to pocket calculators. As Colinge and Colinge say "*more MOSFETs have been fabricated during the last ten years than grains of rice have been harvested by humans since the dawn of mankind*" [47], but what exactly are transistors?

2.1 Origins of transistors

The first patent describing what we would nowadays call a FET dates back to 1926 when Julius E. Lilienfeld, a Polish-American physicist and inventor, filed a patent called "*Method and Apparatus for Controlling Electric Currents*" [48]. This patent granted in 1930 features a structure with three electrodes of a semiconductor material, copper-sulphide (Figure 2.2). This was soon to be followed by another patent always by Lilienfeld, this time featuring a MOSFET device (Figure 2.3). The 1933 patent reported a "*Device to control electrical current*" [49] where a dielectric layer appeared between the

copper sulphide layer and the aluminium one. A third theoretical patent [50] was filed in 1935 by Oskar Heil, a German inventor and electrical engineer. In it another fundamental working principle of transistors is addressed, which is how to control the electrical flow in a semiconductor material through a capacitive coupling at the electrode.

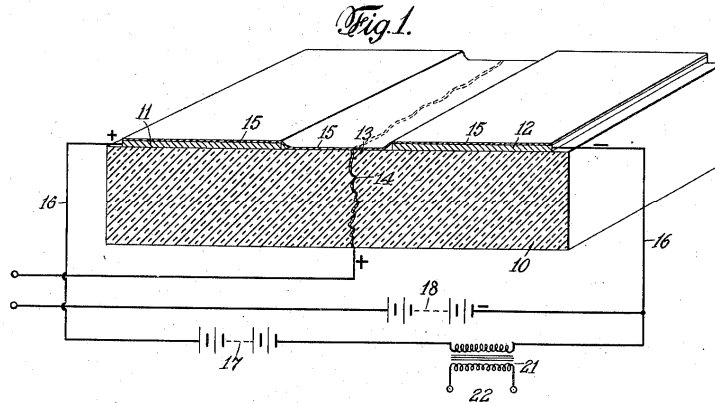


Figure 2.2. Perspective view of the three electrodes structure patented by Lilienfeld (1930) [48].

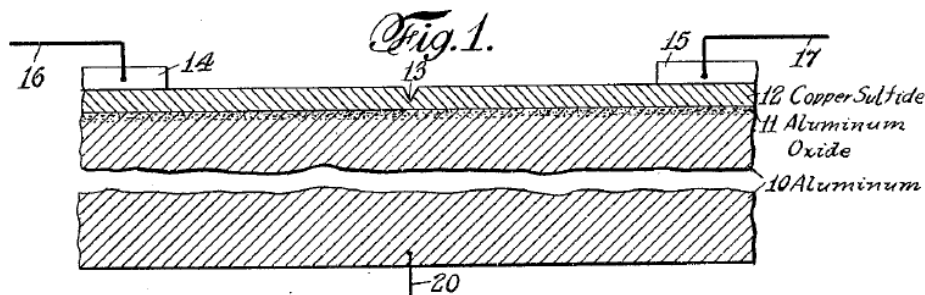


Figure 2.3. Vertical view of the device featured in Lilienfeld 1933 patent. A dielectric layer of aluminium oxide is featured between the semiconducting copper sulphide and the aluminium [49].

Whereas Lilienfeld's 1930 patent concerned a device in which there was the metal directly in contact with the semiconductor material, the kind of device we now call a metal semiconductor field effect transistor (MESFET), the patents of 1933 and 1935 both show the more common MOSFET device [51]. The main differences between those two kinds of devices can be seen in Figure 2.4. Nowadays MESFET devices are generally produced over a GaAs substrate and have a metal Schottky gate [52], whereas the substrate used for MOSFET devices is usually silicon and a dielectric layer acts is grown between the semiconducting substrate and the metallic gate. These two kinds of transistors are used for different applications: MESFET are used in microwave circuits thanks to the superior frequency they can achieve but have the drawback of the Schottky contact and cannot be scaled down. Instead MOSFETs can be used in integrated circuits but their fabrication is more complex.

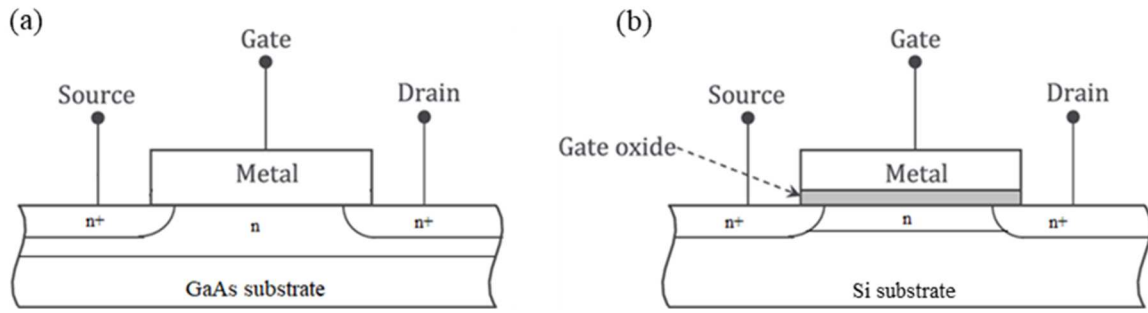


Figure 2.4. Structure of (a) a MESFET and (b) a MOSFET device.

However, there is no sign of these patents ever being applied by their inventors, probably due to technological limitations. One has to wait until the 1963 for the first working MOSFET [53] when Dawon Kahng and Martin Atalla, from the Bells Laboratories, patented the first insulated-gate field effect transistor (Figure 2.5). In the meantime, the physics behind the field effect had been discovered in 1948 by William Shockley and Gerald Pearson [54] and had since been applied to several amplifying devices. However, these devices operation was based on the flow of majority carriers and on its modulation due to a transverse electric field, a different mechanism that the one of the inversion channel now used.

The device of Kahng and Atalla was extremely modern and the basic morphology of MOSFETs hasn't much changed since. The substrate had been switched from aluminium to silicon and a layer of the passivation oxide SiO_2 was chosen as the gate insulator following some studies undertaken by Atalla's group at Bell Telephone Laboratories and a technical memorandum by Kahng [55]. In this memorandum Kahng demonstrated that it was possible to create a device with a $n-p-n$ junction on a silicon substrate with a thin silicon dioxide film. Further steps leading to the actual technologies were the achievement of passivation films sufficiently clean which ultimately led to the introduction of complementary metal oxide semiconductor device (CMOS) in which a n -unit and a p -unit transistors were combined, as will be explained in the next section [56].

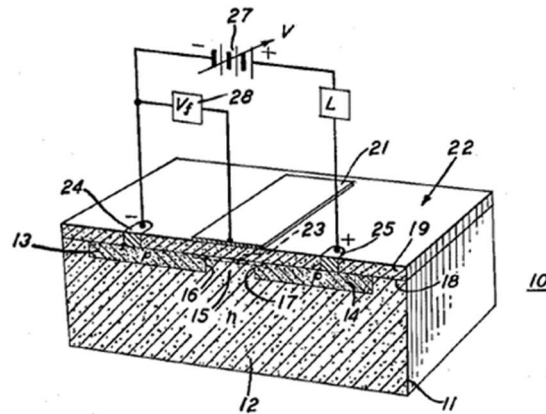


Figure 2.5. Perspective view of the electric field-controlled semiconductor device, as patented by Kahng (1963) [57].

2.2 Working principles

Depending on the kind of charge carrier that is responsible for the current flow, MOSFETs can be divided into two categories. When the electric current is due to electron transport the transistor is called n -channel transistor, whereas in p -channel transistors holes are responsible for the current flow. It is also

possible to find in literature devices in which both a n -channel and a p -channel transistor coexist. Those are called CMOS, as previously stated, and allow a reduction of power consumption and dissipation.

There are several kinds of transistor operations: accumulation, depletion and inversion. In the inversion type, n -channel transistors are built over a p -doped substrate. The analysis here reported will be focusing on n -channel transistors, but the description of p -channel operation is easily obtained mirroring the n -channel one and changing the polarities.

Transistors consist of a series of two junctions, meaning that we will have a succession of n - p - n semiconductors. In the case of an inversion transistor operation, as it is here the case, the source and drain will be $(n+)$ -doped, whereas the substrate will be p -doped. The inversion layer can be seen as a n -doped layer connecting the source and the drain (Figure 2.6).

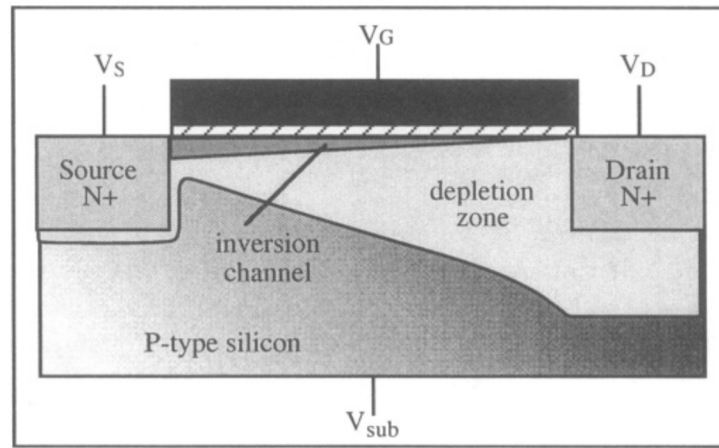


Figure 2.6. Cross section of a MOS transistor [47]. The bias resulting at the source, gate, drain and substrate electrodes are respectively V_S , V_G , V_D , V_{sub} .

When putting two different kinds of semiconductors in contact, as in a junction, the n -type and the p -type will show a different Fermi level, thus not being at equilibrium. Specifically, the Fermi level will be close to the valence band energy level in p -type semiconductors whereas it will be near the Conduction band energy level in n -type semiconductors. To restore equilibrium, the two semiconductors will bend their electronic bands to have continuity of the Fermi level (Figure 2.7). By doing so, electrons and holes will be able to diffuse from one zone to the other and a depletion zone will be formed at the centre of the junction.

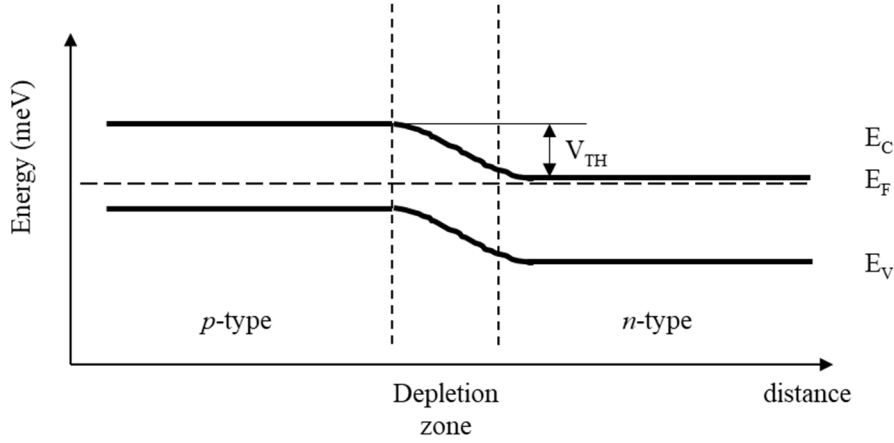


Figure 2.7. Schematic representation of the band structure of a junction. The Fermi levels E_F of the two components are aligned, giving rise to band curvature and the threshold voltage V_{TH} . E_C and E_V are respectively the Conduction and the Valence band.

The bending of the bands also creates a built-in voltage in the junction, called “threshold voltage”, which is provided in equation (2.1). The threshold voltage V_{TH} depends from both internal and external factors. Among the internal factors, the threshold voltage depends on the intrinsic density of charge carrier n_i , and both the donor and acceptor density, N_D and N_A , whereas the external parameters concerned are the temperature T , the Boltzmann constant k , equal to $1.38 * 10^{-23} \text{ m}^2 \text{ kg s}^{-2} \text{ K}^{-1}$ and the elementary charge q .

$$V_{TH} = \frac{k T}{q} \ln \left(\frac{N_D * N_A}{n_i^2} \right) \quad (2.1)$$

The three kinds of operation will now be explained, starting with the accumulation operation, which sees the application of a negative bias, and continuing with the depletion and inversion operations, in which an increasing positive bias is applied. The attention will then be focused on the current flowing in the junction and its different regimes.

2.2.1 Accumulation operation

If a negative bias is applied to the gate, a MOSFET behaves as a parallel-plate capacitor and is in the accumulation regime. Charges are then accumulated at the surface in a thin layer, whose thickness can be derived by integrating Poisson’s equation (2.2)

$$\frac{d^2 \Phi(x)}{dx^2} = -\frac{\rho}{\epsilon_{Si}} = -\frac{q}{\epsilon_{Si}} (p - n + N_D - N_A) \quad (2.2)$$

where $\Phi(x)$ is the potential in the silicon as a function of the depth.

Poisson’s equation states that the potential depends from the charge density ρ , the permittivity ϵ_{Si} of the silicon and the concentration of majority and minority carriers. Those are respectively given by equations (2.3) and (2.4)

$$p(x) = N_A \exp \left(-\frac{q \Phi(x)}{k T} \right) \quad (2.3)$$

$$n(x) = \frac{n_i^2}{N_A} \exp \left(-\frac{q \Phi(x)}{k T} \right) \quad (2.4)$$

Since in the accumulation layer holes become majority carriers and their concentration is higher than the one due to doping, by doing the hypothesis $n \ll p$ and $N_A \ll p$ equation (2.2) becomes (2.5)

$$\frac{d^2 \Phi(x)}{dx^2} \cong -\frac{q N_A}{\epsilon_{Si}} \left(-\frac{q \Phi(x)}{k T} \right) \quad (2.5)$$

By integrating equation (2.5) it is possible to finally obtain the thickness of the accumulation layer x_{acc} , which is shown in equation (2.6)

$$x_{acc} = \sqrt{2} L_D \cos^{-1} \left(\exp \left(\frac{q \Phi_S}{2 k T} \right) \right) \quad (2.6)$$

where L_D is the Debye length indicating the deepness of the electrical field influencing the sample, given by equation (2.7)

$$L_D = \sqrt{\frac{\epsilon_{Si} k T}{q^2 N_A}} \quad (2.7)$$

Nonetheless, since the hole concentration follows an exponential dependence from the potential, the charge can be considered as a surface charge because it is concentrated within a much smaller depth than the accumulation layer.

2.2.2 Depletion regime

When a small positive bias is applied to the gate, a positive charge appears at the metal-oxide interface and a negative one at the gate oxide. Whereas the first one is a surface charge, the second one is a bulk charge that gives rise to a depletion region. By using the Poisson equation (2.2) with the assumption that $n \ll p$ and $N_D \ll N_A$ one finds that the charge density in that region is constant and equal to $-qN_A$. The depletion depth x_d is given by equation (2.8)

$$x_d = \sqrt{\frac{2 \epsilon_{Si} \Phi_S}{q N_A}} \quad (2.8)$$

where Φ_S is the surface potential at the oxide/silicon interface.

2.2.3 Inversion regime

When a higher positive bias is applied the device can enter the inversion regime as the surface potential increases. Current will flow when the applied voltage becomes greater than the threshold voltage V_{TH} . Electrons are then thermally generated when the intrinsic Fermi level E_i becomes lower than the Fermi level E_F (**Figure 2.8**), thus resulting in the electron density exceeding the hole density near the surface and in the appearance of the inversion channel.

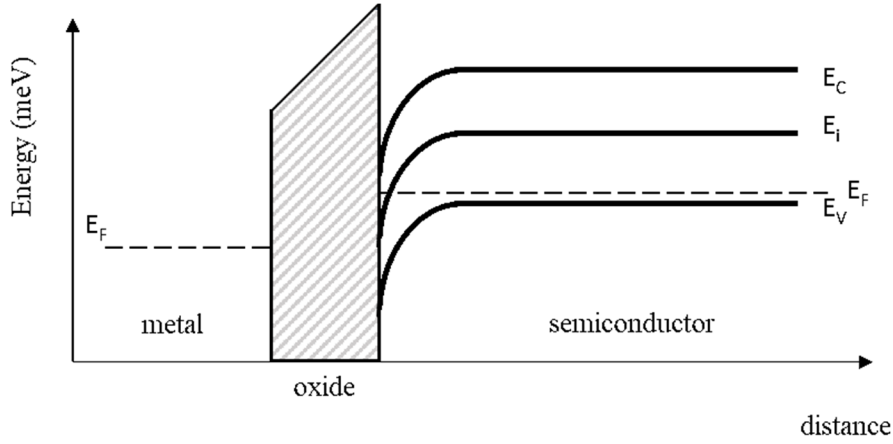


Figure 2.8. Schematic of the band curvature in the inversion regime.

The depth of the inversion channel is very small and comparable to the one of the accumulation layer of (3.6). It can then be considered as a surface charge. The device therefore operates with two transversal conducting electrodes, the metal gate and the electron-rich inversion layer.

2.2.4 Current in the MOS transistor

The current in the device is due to the drift of electrons in the channel between the source and the drain electrodes. Let us remember that the source is grounded, and a positive bias is applied at the drain. The drift current J_n in the channel is given by equation (2.9)

$$J_n = q \mu_n n \mathcal{E} = -q \mu_n n \frac{dV(y)}{dy} \quad (2.9)$$

where \mathcal{E} is the lateral electric field and μ_n is the mobility of the electrons in the channel. The drain current I_D , given in (2.10) can be derived from (2.9) as

$$I_D = -w \int_{x=0}^{\infty} J_n dx = -w Q_{inv}(y) \mu_n \frac{dV(y)}{dy} \quad (2.10)$$

where w is the width of the channel, and $Q_{inv}(y)$ the total inversion charge in the channel.

Now, let us apply Ohm's law to a small channel element of length dy and resistance $dR(y)$. Since the device operates as a parallel plate capacitor, as previously stated, it is possible to write equation (2.11)

$$Q_{inv}(y) = C_{ox} [V_G - V_{TH} - V(y)] \quad (2.11)$$

where C_{ox} is the capacitance of the oxide layer and the effective voltage applied is given by the difference between the gate voltage V_G , the threshold voltage V_{TH} and the local potential $V(y)$. By inserting equation (2.11) into (2.10) and by integrating along the whole channel one obtains equation (2.12) for the drain current:

$$I_D = \mu_n C_{ox} \frac{w}{l} \left[(V_G - V_{TH}) V_D - \frac{V_D^2}{2} \right] \quad (2.12)$$

where l is the channel length and V_D is the drain voltage.

The plot of the dependence of the drain current on the drain voltage can be seen in Figure 2.9, where the saturation regime is also highlighted. The saturation regime is a result of an increasing local potential. As $V(y)$ increases, the length of the channel decreases until V_D reaches a critical value $V_{Dsat} \sim V_G - V_{TH}$. This is when the channel can no longer be assured by the voltage and is said to be

“pinched off”. Although the channel is pinched off, the device will still conduct current, and its current will become constant and independent from the drain voltage. This current is called saturation drain current I_{Dsat} . This happens because a strong electrical field will arise between the drain junction and the pinch-off point, allowing the electrons to flow from one region to the other.

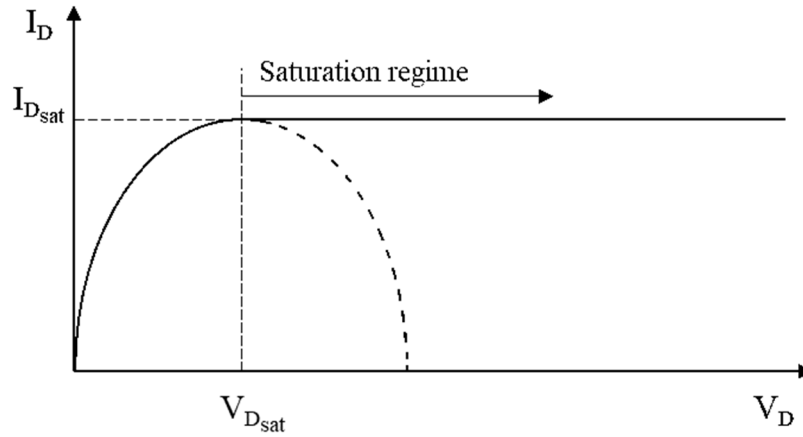


Figure 2.9. Evolution of the drain current I_D as a function of the drain voltage V_D .

Finally, it is possible to summarize the different MOSFET operations in Figure 2.10, [58], [59]:

- When $V_G < V_{TH}$ no current flows in the device
- When V_G reaches V_{TH} , the device operates in the triode regime. As V_D increases, I_D increases at a higher rate until the pinch off point is reached
- When the pinch off point is reached, $V_D = V_{Dsat}$ and the device enters into the saturation regime

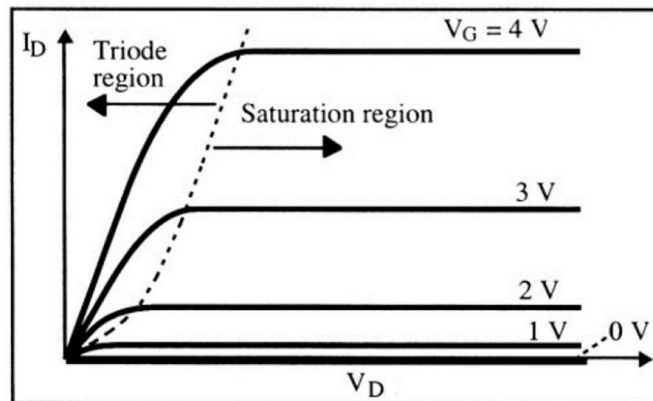


Figure 2.10. I-V characteristics for different values of applied gate voltage V_G [47]. As the applied V_G increases, one can see that the saturation region shifts to higher drain voltages V_D and that the slope of the I_D - V_D curve increases in the triode region.

3. Experimental methods

The samples prepared for this study were produced in different ways to test different properties of graphene. At first a batch of samples were prepared with mechanically exfoliated graphene directly deposited over a Si/SiO₂ wafer to test the properties of such conventional FETs. Such devices will be called Non-Suspended Graphene (NSG) samples. The successive step was to produce samples with mechanically exfoliated suspended graphene (SG), to check whereas the mobility of such samples was enhanced by limiting unintentional inhomogeneities as suggested by Bolotin et al. (2008) [10] and Kim (2014) [19]. In the following paragraphs the preparation of both devices will be addressed. Firstly, the preparation of NSG devices will be explained in detail, then the differences between NSG and SG devices preparation will be highlighted. The testing and measuring protocols will be then addressed.

3.1 Preparation of the mechanically exfoliated NSG samples

3.1.1 Preparation of the substrate

The substrate of the devices is a wafer of SiO₂ (300nm thick)/Si and was thus prepared:

- The wafer is initially cut by cleavage using a diamond indenter and a pair of pins. The cleaving directions of the Silicon wafer are $\langle 110 \rangle$, thus allowing a clean cut of the substrate in square samples.
- The substrate is then washed to eliminate any impurities in an ultrasonic bath: a first washing is conducted with Acetone, then eventually a second one may be done with Methanol. Both are done for 5 minutes in a Branson Yamato 2510J-DTH sonication machine working at 70 V, 42 kHz and 125 W. The substrate is dried with a N₂ gun as soon as it is removed from each bath because the solvents are volatile, followed by a heating at 110 °C for 5 minutes to eliminate any moisture on the surface.
- A spin coating of a hydrophobic substance is then applied to enhance the performance of the substrate [60], because both the substrate and the graphene targets easily adsorbs moisture. The role of this coating is then to reduce the amount of liquid that can come in contact with the substrate. Unfortunately, this also means that if its thickness is too high a successive coating of a liquid precursor like the resists for Electron Beam Lithography (EBL) won't be successful. The coating agent used is Hexa-Methyl-Di-Silazane (HMDS), also known as Bis(trimethylsilyl)amine and whose structure can be seen in Figure 3.1. The coating consists of two successive steps [61]: a first step at 500 rpm for 3 seconds, then a second one at 4000 rpm for 20 seconds. The substrate is then baked at 180 °C for 3 minutes.

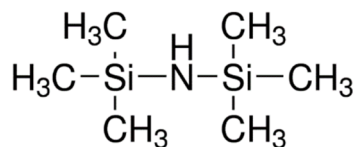


Figure 3.1. Chemical structure of HMDS.

3.1.2 Deposition of graphene

The deposition technique chosen for this work is mechanical exfoliation of graphite. This technique is also called scotch-tape technique because it is conducted by depositing a thin flake of highly oriented

pyrolytic graphite (HOPG) on a tape which is then exfoliated by folding and unfolding the tape about ten times to obtain few layers graphene. The graphene obtained is then transferred to the substrate by applying the tape on the substrate and rubbing it with a plastic tweezer for about 10 minutes. The choice of the 10 minutes rubbing was determined by experimental observations during previous studies conducted in Kubozono laboratory at Okayama University. Another possible way to transfer is to heat the tape applied to the substrate for about 1 minute at 100 °C [62]. However, this technique was used to prepare only two of the NSG devices and then abandoned since the quality of the flakes was lower than the ones obtained with the other technique. After removing the tape, the substrate is sunk in acetone for at least two hours to dissolve part of the residual tape on the surface in the NSG devices. In the case of SG devices, a sink in acetone would result in the dissolution of the hydrophobic coating and would thus destroy the device before its completion (see Supporting information 1. Solubility of three kind of resists for details).

A first manual mapping of the sample is then conducted with an Optimus BX51M optical microscope (OM). The morphology and position of the upper left corner and bottom right corner are checked, the precision of the rulers being $\pm 50 \mu\text{m}$. This will enable a complete mapping of the graphene flakes of the substrate when observations at the Scanning Electron Microscope (SEM) are conducted. Pictures of the corners are taken at x500 and x50 magnification. The sample is then manually scanned to find the graphene flakes deposited on the surface. Pictures of the target and its surroundings are taken at x50, x200 and x1000 magnification and the identification of the number of layers is conducted thanks to the optical contrast between graphene and the substrate, as suggested in [63], [64] and [65]. As can be seen in Figure 3.2 the more layers of graphene one has, the darker the flakes become.

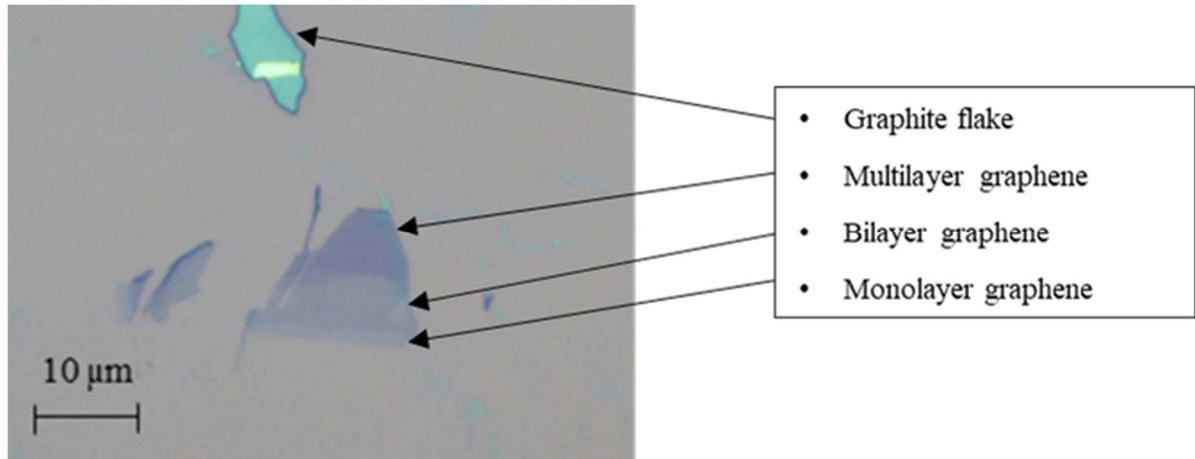


Figure 3.2. Samples of graphite and graphene with increasing thickness observed at OM x1000. The samples were produced by tape exfoliation and the “rubbing the tape” technique.

An easy and handful way to deduce the number of graphene layers samples deposited on a Si/SiO₂ substrate is by measuring their optical contrast arisen from the interference during observations at the OM. If observed under white light, both the graphene and the substrate present a peak in the green region of the visible spectrum. By measuring the position of this peak for the substrate and for the target and by calculating the Relative Green Shift (RGS) caused by the presence of the target, it is possible to obtain the number of additional layers of graphene. In this work the position of the peaks was recorded with the software ImageJ, and the RGS was calculated thanks to equation (3.1)

$$RGS = \frac{G_s - G_g}{G_g} \quad (3.1)$$

where G_s is the green peak of the substrate, whereas G_g is the one of the graphene target. From the value of RGS it is possible to deduce the number of layers of the graphene specimen from the experimental graph of Figure 3.3

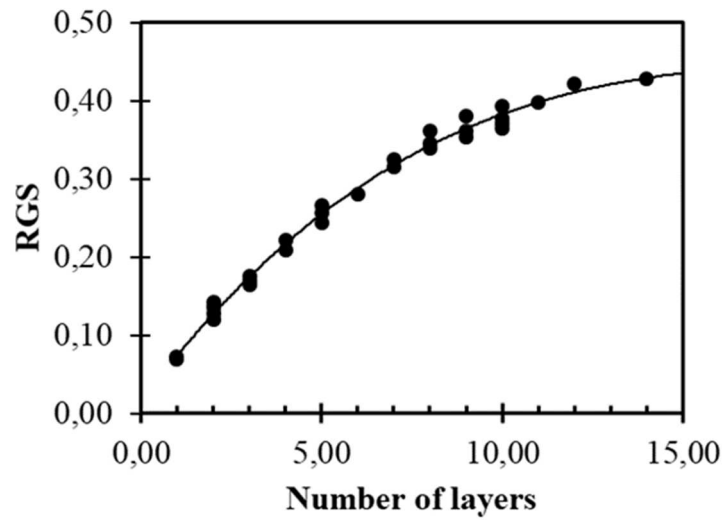


Figure 3.3. Plot of the evolution of RGS as a function of the number of layers in graphene (modified from [66]).

Only specimens of monolayer and bilayer graphene will be considered for further experiments. For each flake that will be considered, the position relative to the corners will be recorded to be able to find it in the SEM.

3.1.3 Etching of the samples by Electron Beam Lithography (EBL)

Before being inserted in the EBL machine, which also operates as SEM, the samples need to be coated with two layers of resist. The lithography used is a positive lithography (Figure 3.4) and the resists deposited are the copolymer 9% poly (Methyl MethAcrylate-co-Methacrylic Acid), dissolved in Ethyl Lactate (MMA 8.5 - MMA EL9) [67] and PolyMethyl MethAcrylate (PMMA).

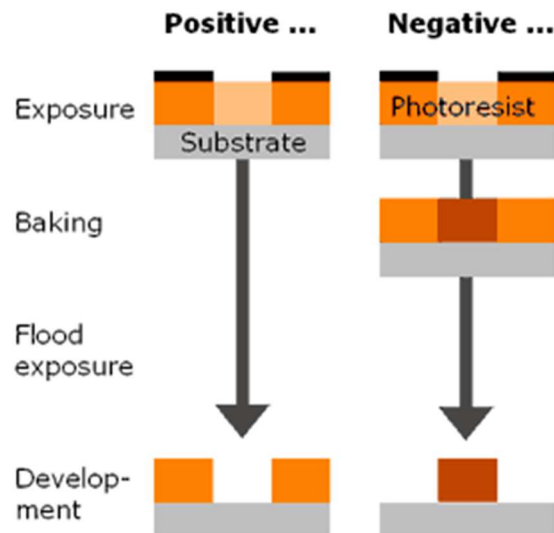


Figure 3.4. Difference between positive and negative photoresists for electron beam lithography. The ones used in this work are positive resists, meaning the part exposed is the one etched away, whereas the part underneath the mask (drawn in black) survives [68].

The choice of applying two different layers is thus motivated. The thickness of the resist must be sufficiently high so that the metal will be removed only where there is the resist and not also from the exposed electrodes shape. Unfortunately, if one was to use only a thick layer of resist there could be some reflection issues with the electron beam which would result in a modified shape of the etched part and in a non-uniform profile of the trenches.

By using two thinner layers of different coatings the beam reflection is suppressed, and the precision of the etched pattern is conserved. The first layer deposited is the copolymer which is more sensible to the etching: this will allow an easier removal of the resist in the last step as it will be more excavated than the PMMA (Figure 3.5). Both layers are spin coated with a protocol similar to the one used for HMDS: a first step of 3 seconds at 500 rpm followed by 20 seconds at 4000 rpm. The substrate is then baked at 180 °C for 1 minute before the second layer is spin coated.

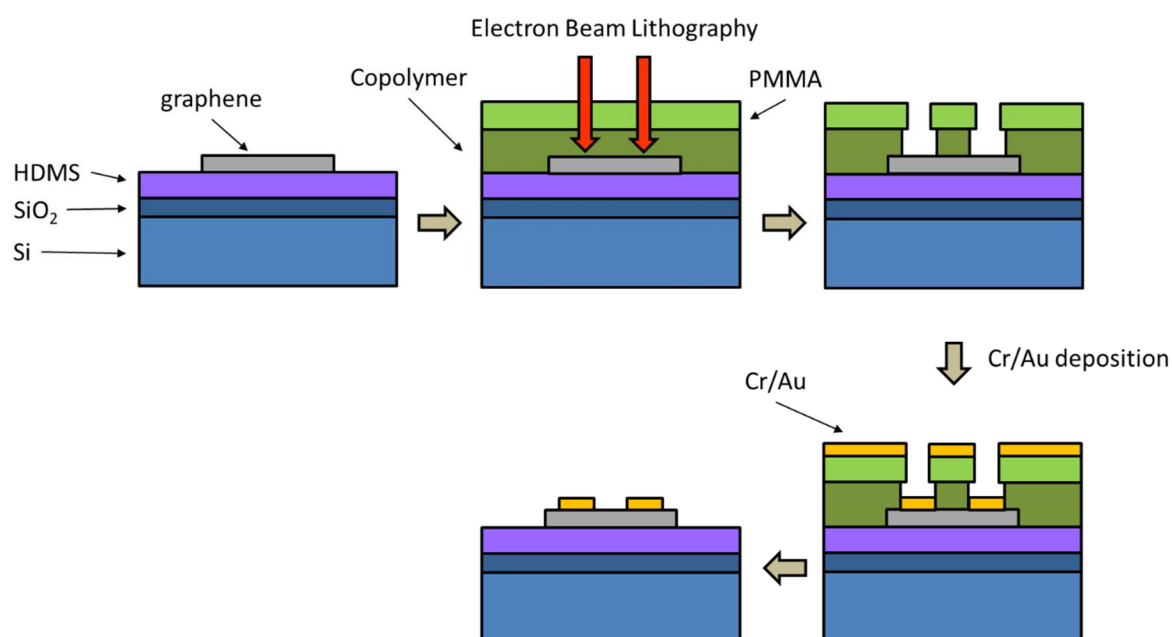


Figure 3.5. Schematic of the NSG sample preparation. It is possible to see that the copolymer layer is more etched than the PMMA layer during EBL thus allowing an easier lift-off after the deposition of the electrodes.

A new observation at the OM of the samples is necessary after the coating before going to the SEM. This is because the coating can change the morphology of the surface and some piece of the corners may have been torn during the operations, as can be seen in Figure 3.6.

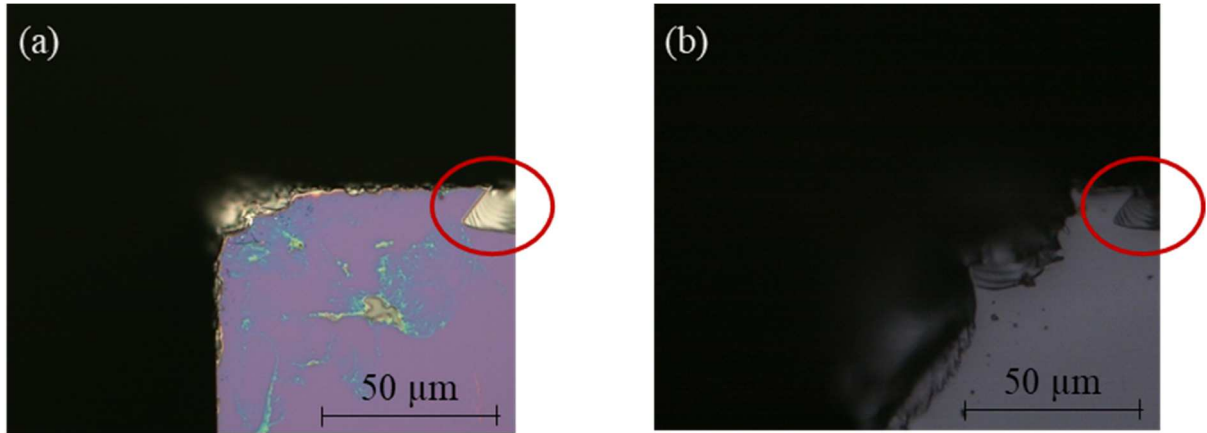


Figure 3.6. Observation at x500 of the upper left corner of a sample (a) before and (b) after the coating. The actual corner has been cleaved during the operations due to human manipulation, but the hole on the right can act as guidance to understand the original shape.

We then insert the samples in the EBL machine (Elionix ELS-S50) being careful to maintain their direction. We firstly observe the corners of the samples through the SEM comparing them with the pictures taken at the OM. By taking their positions in the SEM system it is possible to obtain the position of the corners and the targets in the Computer Aided Design (CAD) system, which will be used to design the electrodes, through a program (Sample Position) designed by Prof. H. Goto. By doing so one also obtain the “position shift” for each sample which is needed to launch the CAD layout from the right starting point.

A blue print of the patterns to be etched is then obtained with the software Draftsight. A sample of said blueprint can be seen in Figure 3.7: the shape of the chip is drawn with blue and green lines, whereas the yellow squares stand for the marks that will be etched on the sample.

There are two kinds of alignment marks: Reg-2 are single cross patterns indicating the corners of the sample with a field size of 250 nm, whereas Reg-3 are squares of 10x10 crosses to indicate the position of the graphene flakes with a field size of 500 nm. The Reg-2 are meant to take into account the positional deviation due to human handling, which could result in a non-correct etching of the sample.

To correct the deviation both linear and rotational thus caused, a registration of the marks is performed, and the exposure position is corrected using the coordinates of the two marks. The Reg-3 marks are similar to the Reg-2 marks but smaller and placed in the exposed field to allow a better precision without moving the stage [69]. The CAD model is then opened in the EBL machine with the software WeCas from where it is launched. The etching is conducted with a 100 pA gun beam current, under 30 keV and with a dose time of 0.75 and 3.0 $\mu\text{sec/dot}$ respectively for the Reg-2 and Reg-3 marks.

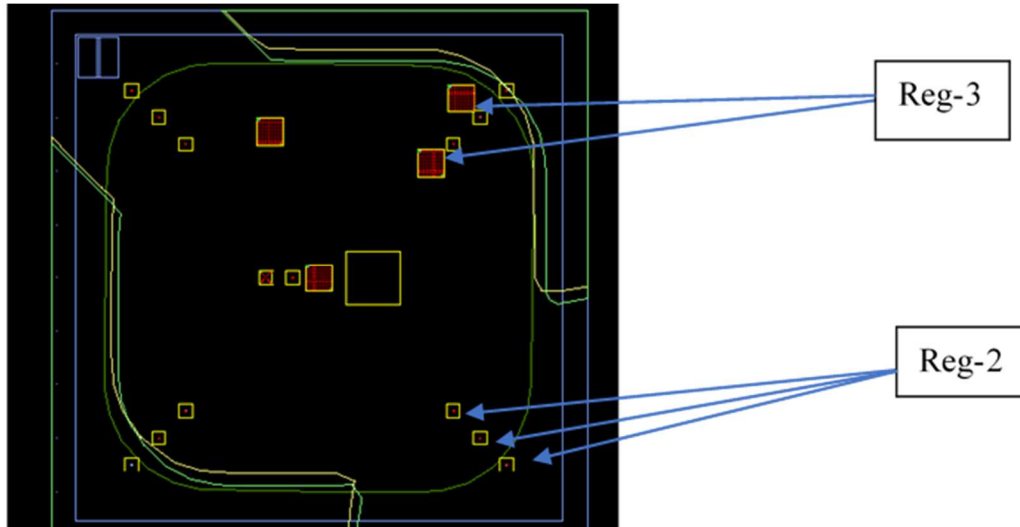


Figure 3.7. Blueprint of the chip with Reg-2 and Reg-3 marks. It is possible to see nine Reg-2 marks (three on each corner) and three Reg-3 marks. The marks at the centre of the chip are not etched and serve as template to build the blueprint.

After the etching the samples are washed in Methyl-Isobutyl Ketone (MIBK 1:3 IPA) for 1 minute and then rinsed in IsoPropanol (IPA) for 10 seconds. They are then spray dried with a N₂ gun [70].

An observation at the OM of the corners and patterns etched is then necessary to check whereas the etching was successful or not. Photos of the targets containing at least two Reg-3 correctly etched are taken at x1000 (Figure 3.8), x200 and x50 magnitude.

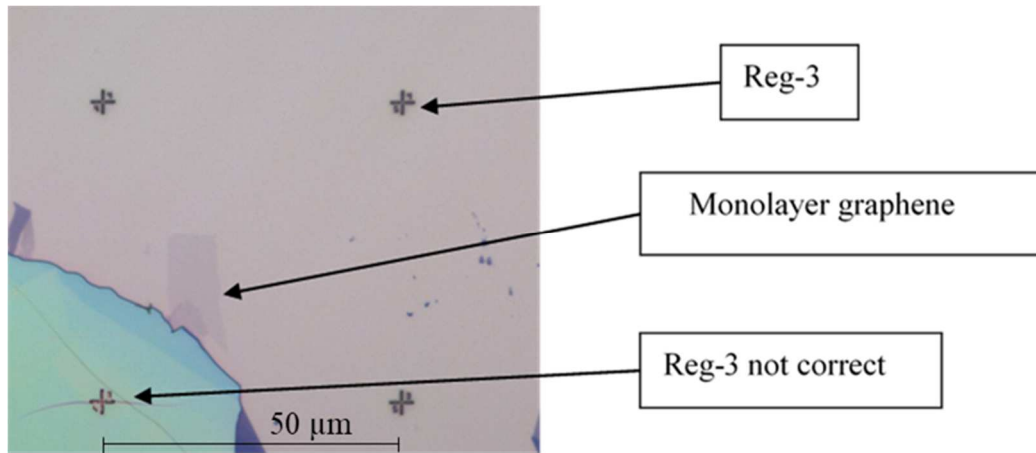


Figure 3.8. Target of graphene in the sample etched observed at OM (x1000). The Reg-3 mark in the left bottom of the picture cannot be taken as a reference because it is on a piece of graphite, the other three marks are correct. The space between two Reg-3 marks is 50 μm .

The electrodes are then designed with the software Draftsight. To design them one first need to attach the photos taken at the microscope in the blue print (Figure 3.9). The x1000 photo is attached to the Reg-3 and then the x50 photo under this one.

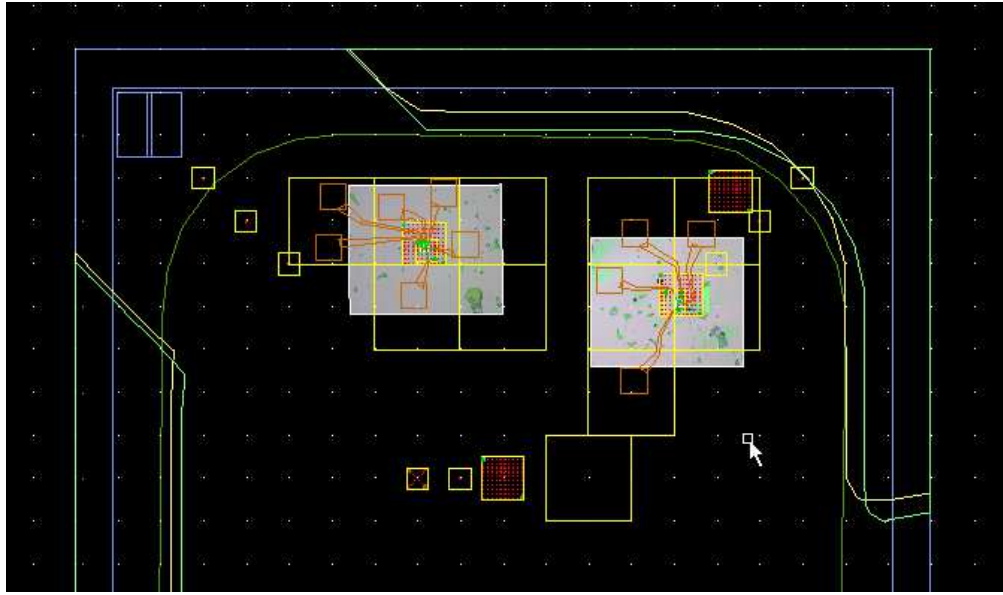


Figure 3.9. Blueprint of the sample with photos and electrodes attached.

In order to do a four-terminal measurement, we then need to draw at least four electrodes: the first and the last must cross the target, whereas the central ones must only make a bridge between the target and the substrate. The minimum width of the central is $0.5\ \mu\text{m}$, whereas for the external one is $1\ \mu\text{m}$ (Figure 3.10). Once the electrodes are done, we need to extend them first to the edge of the chip etched (in the “lead” layer) and then to some squares (in the “pad” layer). These connections must not intersect thick graphite layers.

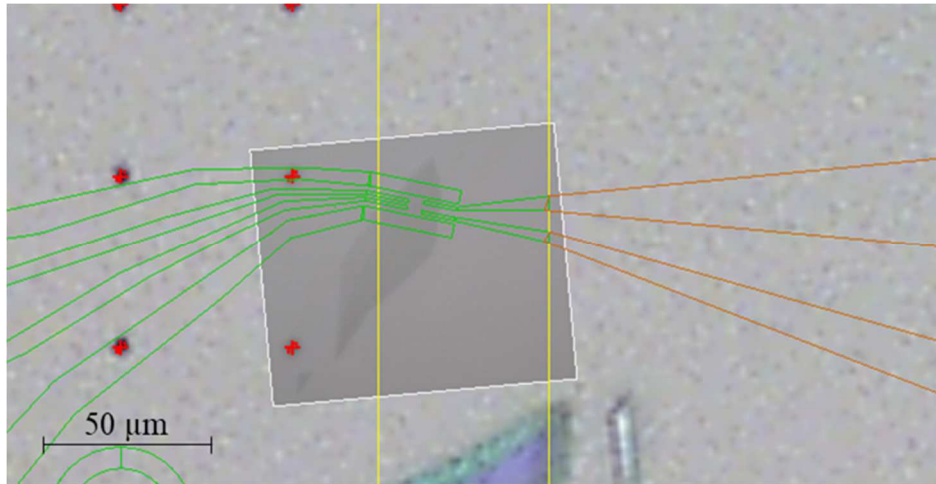


Figure 3.10. Detail of the chip with the electrodes. The photo taken at $\times 1000$ magnitude is applied on the one taken at $\times 50$ which has a less precise focus. The four terminals are drawn on each target and are extended to the end of the chip (lead layer, in green) where they are connected to the pad layer (in brown). The space between two Reg-3 marks is $50\ \mu\text{m}$.

The patterns of the electrodes are then etched by EBL under a $100\ \text{pA}$ gun beam and a dose time of $0.75\ \mu\text{sec/dot}$ for the lead layer and a $1\ \text{nA}$ gun beam and a dose time of $1.12\ \mu\text{sec/dot}$ for the pad layer.

The development of the etching is conducted with a wash in MIBK:IPA (1:3) for 1 minute followed by a wash in IPA for 10 seconds. The sample is then spray dried with a N₂ gun.

An observation at the OM is necessary after the etching. Its aim is to assess whether there are contacts between the electrodes, the electrodes are on the target and no graphite flake make bridges between them. If any of the above occurs in the sample, as in Figure 3.11, the target cannot be further tested. In order to avoid that, multiple images of the surrounding of the target must be taken with a magnitude of x50 in order to effectively map the area that will be etched.

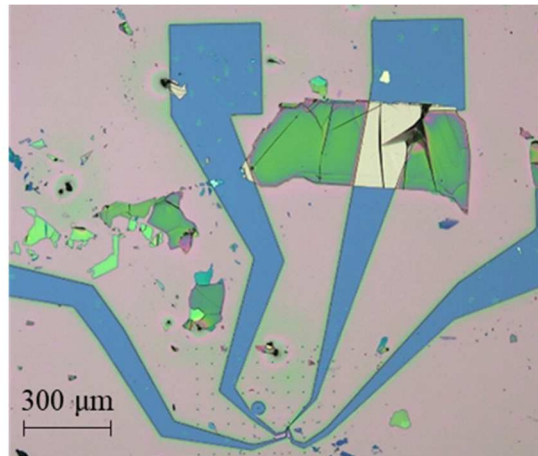


Figure 3.11. Example of electrodes connected by a flake of graphite, image taken at the OM at x50. This target cannot be further tested.

Before the deposition occurs, the sample must be scratched with a diamond indenter to create a point where the metals will be deposited directly over the substrate. This will enable the creation of a gate point, necessary to perform the electrical characterization of the devices. The deposition of the electrodes is then conducted by Physical Vapour Deposition (PVD) in high vacuum, about 10^{-7} Torr. Three pumps are involved in the process: a rotary pump for primary vacuum (until about 10^{-2} Torr), and two turbo pumps for secondary vacuum.

Two metals are chosen: chromium and gold, with respective thicknesses of 5nm and 100nm. The chromium layer acts as an adhesive layer for the gold one which is the real electrode with high conductivity but does not adhere well to silicon oxide. However, the chromium is easily oxidized when in contact with air, hence its thickness of only 5nm. After the deposition, the samples are kept in acetone for two hours to dissolve the resist, then washed with a syringe of acetone, rinsed in 2-Isopropanol to remove all the resist with the gold and spray dried with N₂.

After a last observation at the OM to check the electrodes, the device is ready to be tested. As in the observation of the electrodes after the etching, their continuity and integrity have to be checked. In Figure 3.12 two examples of electrodes can be seen: in the left image the electrodes are connected by some gold, the removal of the resist wasn't successful, whereas the electrodes on the right are correctly deposited.

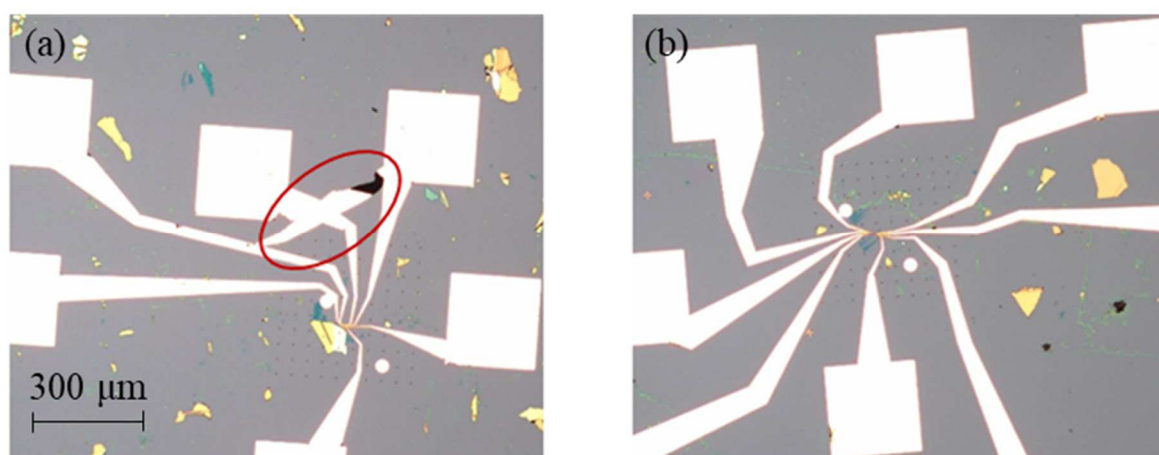


Figure 3.12. Observation at x50 of the electrodes after the deposition and lift off process. In (a) the electrodes are connected and cannot be further tested, in (b) the electrodes have been correctly deposited.

The samples are then ready to be have their FET properties checked. In order to check whereas they are working or not a first two-terminal or four-terminal measurement is performed under a controlled atmosphere of N_2 . If the device results functioning, further analyses are conducted, as will be explained in the following sections.

3.2 Preparation of the mechanically exfoliated SG samples

In the case of the samples with suspended graphene the initial washing operations of the substrate, points (a) and (b) of paragraph 3.1.1, are the same, whereas the deposition of the coating is different. The procedures were taken from a study published in 2011 [26], but the coating agent, deposited under yellow light because it will be etched by EBL, was changed to the lift-off layer LOL-2000, or polymethylglutarimide [71], due to laboratory availability. The coating is deposited in two successive steps, a first one of 3 seconds at 500 rpm and a second one of 40 seconds at 2000 rpm. The sample is then baked at 180°C for 3 minutes. Since in this case the coating is necessary to suspend the graphene over a trench its thickness is fundamental. We consequently performed five times the coating on each sample in order to have a thickness of about $1.3\ \mu\text{m}$. Nonetheless, the optimal thickness of this coating agent hasn't be determined yet.

The graphene deposition was also conducted by Scotch Tape technique, but the samples weren't sunk in acetone for two hours to remove tape residues. This would have resulted in the dissolution of the LOL coating previously deposited, thus making the samples useless (see Supporting information 1. Solubility of three kind of resists). An observation at the OM was then conducted, but the identification of the targets was more difficult due to the yellowish colour of the substrate and the number of layers couldn't be identified by a simple analysis of the RGS (Figure 3.13).

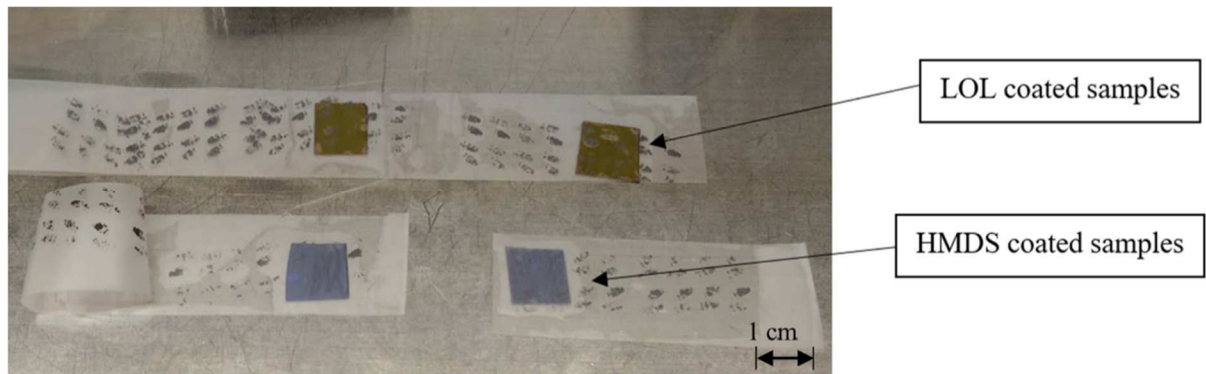


Figure 3.13. Comparison of the samples coated with LOL and destined to be SG devices (top) and the samples coated with HMDS destined to be NSG devices (bottom) during the deposition of graphene by scotch tape technique. One can see that the top samples present a yellowish surface whereas the bottom ones present a blueish-violet surface.

Targets were then chosen as the thinnest one could find while scanning the samples at the OM. The identification of the number of layers will be performed by Raman Scattering at the end of the process [36]. One could do it after the deposition of graphene, but the results could be misrepresentative because of the contribution of the LOL coating which is also an organic material. We then decided to perform it at the end of the fabrication process when the graphene target will be suspended so that the results will be representative. A consequence of this choice is that we won't be able to know beforehand whether the targets are monolayer, bilayer or few layer graphene, but the realisation of devices with different thicknesses will allow us to draw comparisons between them and to better understand the properties of suspended graphene.

The dose of exposure for the samples of suspended graphene was changed from the one used for NSG samples. In this case the dose time was $0.78 \mu\text{sec/dot}$ for the Reg-2 marks and $3.12 \mu\text{sec/dot}$ for the Reg-3 marks. The development after the etching was at first conducted as instructed in [26]. A first sample was sunk in xylene at room temperature for 4 minutes, rinsed in hexane and then spray dried with a N_2 gun. When observing the development at the OM, the marks weren't completely etched. We considered this the result of the etching of only the PMMA layer, since in [26] both layers were of PMMA of different molecular weight. Since in our case we have a copolymer layer and a PMMA layer we decided to develop again the samples at room temperature in MIBK and rinse in IPA, then spray dry with a N_2 gun. However since the PMMA layer was already etched we opted for an etching in MIBK:IPA (1:3) of only 25 seconds, which resulted a time long enough. This resulted in a correct development of the etched areas and allowed us to know that xylene did not attack the copolymer layer exposed to EBL. During the preparation of the successive devices, nonetheless, we decided to revert the developing of the etching to 1 minute of MIBK:IPA (1:3) at room temperature, a rinse of 10 seconds in IPA and a spray dry with a N_2 gun.

Since the graphene will be suspended at the end of the process and should not collapse on the substrate underneath it, the size of the electrodes should be carefully chosen. We decided to set the channel length to $2 \mu\text{m}$ based on [72], and to draw thicker lateral electrodes ($3\sim 4 \mu\text{m}$) in order to better support the suspended sheet as suggested in [10]. The dose times to draw the electrodes weren't changed from the NSG devices for these devices, remaining $0.75 \mu\text{sec/dot}$ for the lead layer and $1.12 \mu\text{sec/dot}$ for the pad layer.

The lift-off process for the mechanically exfoliated SG devices was conducted with hot xylene (80°C) as instructed in [26]. The samples were sunk in xylene until the complete removal of the gold layer was achieved. To achieve a complete removal of the gold layer the samples were sunk for about one hour and a half and rinsed with a syringe in the same bath, then spray dried with N_2 gun immediately after being removed from the hot xylene bath.

The samples were finally exposed to deep UV radiation in order to remove the LOL layer between the electrodes and suspend the targets of graphene. This exposure also allows a final removal of residues of copolymer after the earlier development in hot xylene. For this purpose, a mercury lamp was used, and the time of exposure was set to 10 minutes. The exposure time has not been optimized yet and if too long could result in a removal of the LOL under the electrodes, which would be responsible for the collapse of the devices. The final development was then conducted in ethyl lactate at room temperature for 1 minute and rinsed in hexane for 10 seconds, then spray dried with N₂ gun. The entire process of preparation of the mechanically exfoliated suspended graphene devices is summarized in Figure 3.14 and in Table 3.1 are summarized the main differences between the NSG and the SG devices.

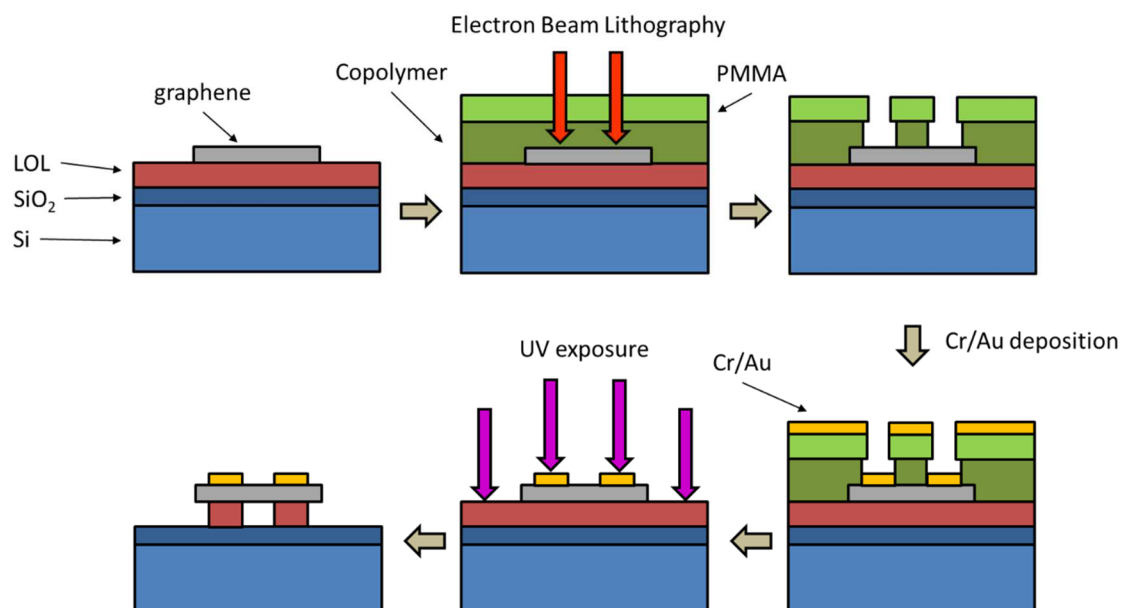


Figure 3.14. Schematic of the preparation steps for the mechanical exfoliated suspended graphene devices.

Table 3.1. Summary of the main characteristics and differences between NSG and SG devices.

	NSG	SG
Hydrophobic layer	HMDS	LOL
Deposition of graphene	Scotch tape technique	Scotch tape technique
Technique to determine the number of layers	Optical contrast	Raman spectroscopy
Dose time for exposure of Reg-2	0.75 $\mu\text{sec/dot}$	0.78 $\mu\text{sec/dot}$
Dose time for exposure of Reg-3	3.00 $\mu\text{sec/dot}$	3.12 $\mu\text{sec/dot}$
Dose time for exposure of lead layer	0.75 $\mu\text{sec/dot}$	0.75 $\mu\text{sec/dot}$
Dose time for exposure of pad layer	1.12 $\mu\text{sec/dot}$	1.12 $\mu\text{sec/dot}$
Development after etching processes	1 min MIBK:IPA (1:3) followed by 10 sec rinse in IPA	1 min MIBK:IPA (1:3) followed by 10 sec rinse in IPA
Lift-off process	Acetone	Hot xylene (80 °C)

3.3 Electrical measurements

Two different kinds of electrical measurements were conducted on the samples based on their nature. In the case of NSG devices four-terminal measurements under vacuum (10^{-7} Torr) were chosen because they were the most reliable and precise available. On the other hand, this kind of measurement didn't suit the geometry and the nature of the SG devices before and after the UV exposure because it required, amongst other things, the sample to be cut, which was a difficult operation to perform and could damage the suspended devices. A two-terminal measurement was then chosen as the testing method for this kind of devices and was conducted in a glovebox filled with argon gas.

3.3.1 Four-terminal measurements

The setup of the four-terminal measurement can be seen in Figure 3.15. During the four-terminal measurement the gate voltage varies from -50 V to $+50$ V with an interval of 1V whereas the drain voltage will vary between -1 mV to 1 mV with intervals of 0.1 mV. The samples were placed in a vessel connected to two rotary pumps and a turbo pump. The measures were conducted with Agilent Technologies B1500A Semiconductor Device Analyzer and the software Easy Expert to do a first measurement of the properties of the sample as obtained after its preparation. The samples were then annealed for one hour at 100 °C under vacuum (10^{-7} Torr) and then cooled down naturally with a Model 9700 by Scientific Instruments.

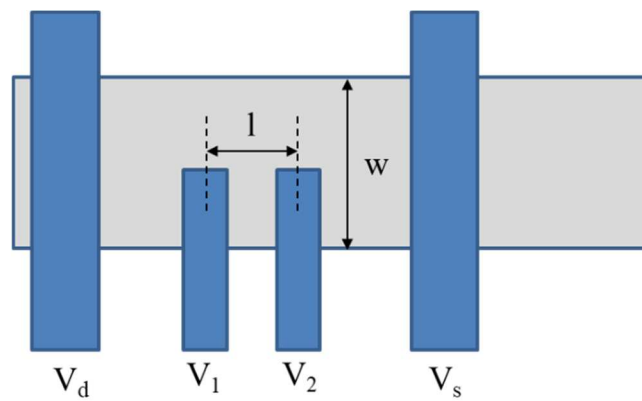


Figure 3.15. Experimental setup of a four-terminal measurement. The graphene target is grey, whereas the blue rectangles are the four electrodes: drain, measurement probe 1, measurement probe 2, source. l stands for channel length and w for the channel width.

Each registered value provides an ohmic curve so that the evolution of the conductance G of the sample as a function of the gate voltage can be obtained. Through equation (3.2) it is possible to then deduce the values of conductivity.

$$\sigma = G * \frac{l}{w} \quad (3.2)$$

Where l is the channel length, measured between the middle points of the two internal electrodes and w is the width of the channel, measured in the middle of the device.

The curve of the conductivity of the samples presents a minimum corresponding to the Dirac point of graphene. Theoretically the Dirac point should be at ~ 0 V but it can be shifted to positive values (as in Figure 3.16) or to negative values if the sample results to be doped. In case of positive shifts, the sample is p -doped, whereas in case of negative shifts the sample is n -doped. This involuntarily doping can be determined by the adsorption of electron donor molecules, such as water, (in case of p -doping) or electron acceptor donor molecules (in case of n -doping). The samples prepared in this study result

mostly *p*-doped due to water adsorption [3] and possible traces of lithographic resist [60], thus needing an annealing to observe their actual properties.

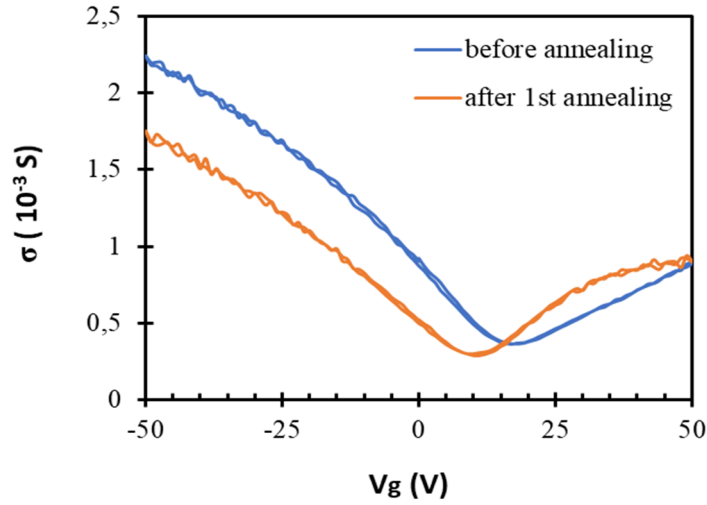


Figure 3.16. Conductivity curves of a *p*-doped sample before (blue line) and after a first annealing conducted at 100 °C for one hour (orange line). The Dirac point shift appears to be reduced from 19 V to 9 V but the mobility (proportional to the slope of the curve near the Dirac point) isn't much improved.

3.3.2 Two-terminal measurement

In the case of a two-terminal measurement, the electrodes considered are only the source and the drain. Whereas the four-terminal measurement provides a more accurate value of the properties measured, a two-terminal one can be more easily conducted if the device has a complicated shape or in the case of the suspended graphene devices, where the bending resistance of the sheet is strained by the presence of several electrodes. In the case of the two-terminal measurement, the gate voltage varies from -40 V to 40 V with steps of 1 V whereas the drain voltage will vary between -1 mV to 1 mV with intervals of 0.1 mV. The measures were conducted with Agilent Technologies B1500A Semiconductor Device Analyzer and the software Easy Expert. The experimental setup for the measurements can be seen in Figure 3.17.

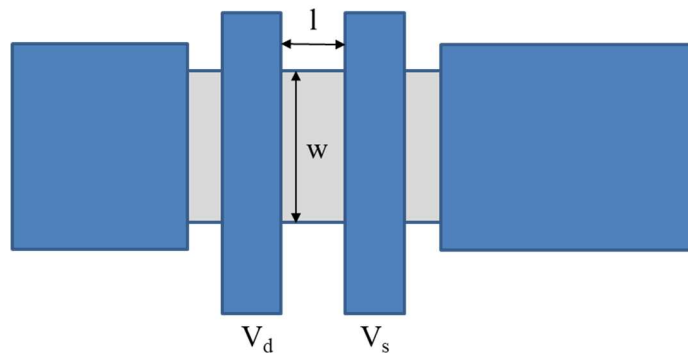


Figure 3.17. Experimental setup for the two-terminal measurements of the SG devices. The graphene target is grey, whereas the blue rectangles are the two electrodes, source and drain, and the masks for supporting it mechanically on the sides. *l* stands for channel length and *w* for the channel width.

4. Results and discussion

Several kinds of NSG devices were realized in this work in order to be able to draw a comparison between them. The first devices were produced with a standard protocol, which is mechanically exfoliating the graphene by a scotch tape technique and depositing it over a silicon/silicon oxide wafer coated with HMDS. These devices will be from now on called “NSG standard devices” and their characteristics are listed in Table 4.1. A second kind of NSG devices are the one obtained in the process of the SG devices, before the UV exposition (see paragraph 3.2 for details on the preparation). These devices, called “LOL-NSG devices”, present the graphene mechanically exfoliated deposited over a coating of LOL instead of the HMDS. Their characteristics are listed in Table 4.8.

4.1 NSG standard devices

The NSG standard devices were tested with four-terminal electrical measurements under high vacuum (10^{-7} Torr), as explained in paragraph 3.3.1. The data obtained from the electrical measurements were analysed in order to obtain the FET parameters. The conductivity was obtained from equation (3.2), by inserting the channel length and width of the device analysed. The mobility was then obtained by equation (4.1) where C_{sub} is the capacitance of the silicon substrate coated with a 300 nm layer of silicon dioxide, equal to $11.5 * 10^{-9} \frac{F}{cm^2}$, and $\left| \frac{d\sigma}{dV_g} \right|$ is obtained as the slope of the conductivity curve near the Dirac point.

$$\mu = \frac{1}{C_{sub}} * \left| \frac{d\sigma}{dV_g} \right| \quad (4.1)$$

Finally, the amount of impurities released after performing an annealing treatment was obtained through equation (4.2), where ΔV_g is the shift of the Dirac point subsequently to the annealing and q is the elemental charge, equal to $1.6 * 10^{-19} C$ [73]

$$n = \frac{C_{sub} * \Delta V_g}{q} \quad (4.2)$$

The mechanically exfoliated NSG samples were produced as described in paragraph 3.1. They were then tested with a four-terminal measurement before and after being annealed under high vacuum (10^{-7} Torr). A general prospectus of the devices tested with four-terminal measurements is reported in Table 4.1, a more detailed one is available in Supporting information 2. Infographic of the mechanically exfoliated NSG devices. Three monolayers and one bilayer devices were considered for this study, with similar channel lengths. Of the four devices considered, only one resulted to be slightly n -doped, whereas the other three resulted to be p -doped, as it is more usually the case. It is generally acknowledged that traces of water and O_2 can be easily adsorbed during the preparation of the devices [3], [73] and traces of resist can still be present even after the lift-off processes [60], resulting in an apparent p -doping of the device. According to [74] a thin continuous layer of resist persists to remain over the devices even after the lift-off procedures, and could be removed only with an annealing at $400^\circ C$. The device that results slightly n -doped reflects a better quality of the preparation of the sample, as showed also by a higher mobility. After a first comparison of the three monolayer devices characteristics, a more detailed analysis of each device will be conducted to better understand the physics behind their behaviour.

Table 4.1. General prospectus of the characteristics of the mechanically exfoliated NSG devices obtained from four-terminal measurements. The mobility taken into consideration is the electron mobility (μ_e). The annealing conducted was of 1 hour at 100°C.

Sample #	Number of layers	Channel length, μm	Channel width, μm	Doping type	μ_e before annealing, (cm^2/Vs)	μ_e after annealing (cm^2/Vs)
3	Monolayer	2.00	3.04	P	1739	2609
14	Monolayer	2.00	2.06	N	6957	8696
15.2	Monolayer	1.00	1.96	P	2609	3478
15.1	Bilayer	2.00	7.11	P	3478	4348

A comparison of the behaviour of the three monolayer devices before and after the annealing treatment is reported in Figure 4.1. One can see that whereas the holes conductivity values are quite similar for the three devices both before and after the annealing, the values of the electron conductivity greatly differ between the different samples. On the other hand, one can also see that whereas the electron conductance value of each device does not change much before and after the annealing, the one of the holes decreases of about 10^{-3} S in each of the devices. It is also possible to notice that whereas the curves of monolayer graphene should be linear and have a very sharp Dirac point, this is not the case with our devices.

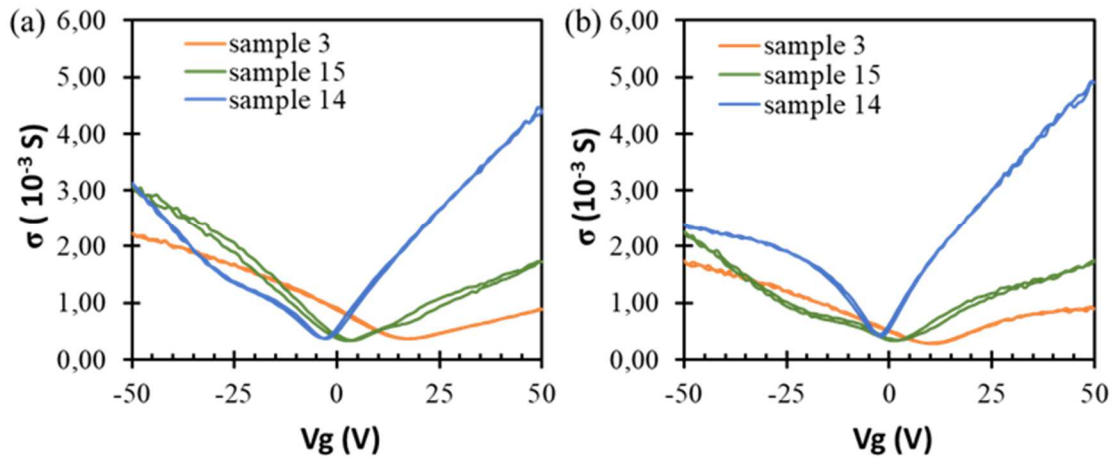


Figure 4.1 Comparison of the conductivity curves of the monolayer devices (a) before the annealing and (b) after completing the annealing of 1 hour at 100 °C.

Focusing on the effect of the annealing of the devices (Table 4.2), one can see that almost all the devices, monolayer or bilayer, follow the same behaviour after having undertaken the post-treatment of annealing, regardless of its temperature. The only device differentiating itself is the device realized on sample 14 which shows an increase in both the electron (μ_e) and hole mobility (μ_h) and a Dirac point shift of only 0.5 V in the negative voltages, which can be attributed to its higher quality. The higher quality is also reflected in its higher values of mobility and in the symmetry of the carrier mobilities values. All the other samples present a decrease in the hole mobility and an increase in the electron mobility.

A correlation between the post-treatment and this variation does not appear evident, but at the same time some recurrent values can be noticed when looking at the data of Table 4.2. As a matter of fact, the hole mobility drops to 2609 cm^2/Vs in the case of the annealing of 1 hour at 100 °C for both the monolayer devices of sample 3 and 15 though the initial values for the two devices are significantly

different, as underlined by the difference in the reduction of the value. However, this behaviour is not observed in the electron mobility data.

Another interesting data is the fact that both the devices on sample 3 and sample 14 after a first annealing show a symmetry between the two carrier mobility, although the one of device 14 is almost four times the one of device 3. However, in the first case the value of the common mobility is achieved by levelling the two initial mobilities, whereas in the second case both mobilities are increased to reach the final value, thus resulting in an overall improvement of the device. In addition to this, one can also see that in the case of the device of sample 3 a further annealing only resulted in lowering more the value of the hole mobility, further damaging the overall mobility. One can also see, from the results of the second annealing performed on sample 3 and the annealing performed on sample 15, that the amount of impurities released is proportional to the shift of the Dirac point independently from the temperature at which the annealing is performed (see equation 4.2).

Table 4.2. Characteristics of the mechanically exfoliated NSG devices after the annealing treatment. For each treatment the shift of the Dirac point, the amount of impurities released, the final mobilities and the variation of the electron (μ_e) and holes mobilities (μ_h) are considered.

Sample #	Shift in Dirac point [V]	Impurities released [cm^{-2}]	$\Delta\mu_e$ [%]	Final μ_e [cm^2/Vs]	$\Delta\mu_h$ [%]	Final μ_h [cm^2/Vs]
3	- 10	7.19 E+11	+ 50 %	2609	- 25 %	2609
3 (at 110 °C)	- 2	1.44 E+11	0	2609	- 33 %	1739
14	+ 0.5	3.59 E+10	+ 25 %	8696	+ 67 %	8696
15 (MLG)	- 2	1.44 E+11	+ 33 %	3478	- 50 %	2609
15 (BLG)	- 13	9.34 E-11	+ 25 %	4348	- 77 %	609

Each device will now be taken into further consideration, starting with the three monolayer devices and then moving on to the bilayer device. The device realized on sample 3 resulted to be *p*-doped and presented a ribbon shape, the optimal shape for this kind of applications. Nevertheless, it wasn't isolated but was "extruding" from a thicker flake of about three layers, as can be seen in Figure 4.2.

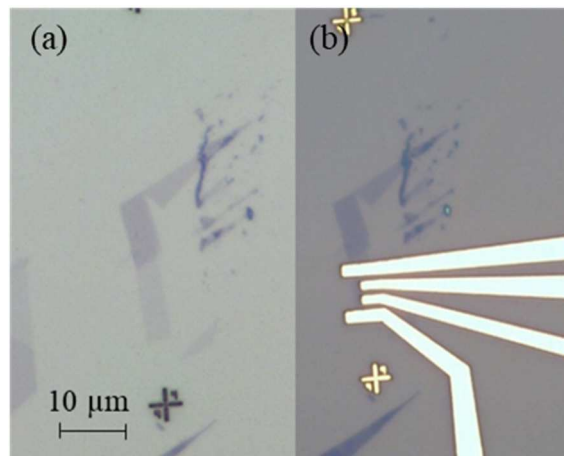


Figure 4.2. Details of the device realized on sample 3 at the OM x1000. (a) the target as seen after the etching of the Reg marks, (b) the device after the deposition of the electrodes before being tested.

A first measure was conducted on the sample and the mobility was recorded, then a first annealing was conducted to reduce its apparent doping. The sample was heated for 1 hour at 100 °C then let cool down naturally. The four-terminal measurement was then run again (orange curve in Figure 4.3). Whereas the annealing appeared to have been successful, the Dirac point having shifted from 19 V to 9 V (Table 4.3) and the electron mobility having increased from 1739 cm²/Vs to 2609 cm²/Vs, the sample still resulted *p*-doped. A second annealing was then performed at 110 °C for another hour after which the conductivity was tested again (grey curve in Figure 4.3). The second annealing resulted in a smaller shift of the Dirac point, this time from 9 V to 7 V, but didn't improve the electron mobility. In addition to these two effects, the second annealing accentuated the saturation of the electrons that was initiated during the first annealing. The reasons of this saturation of the mobility of the carriers has yet to be determined and will be later analysed.

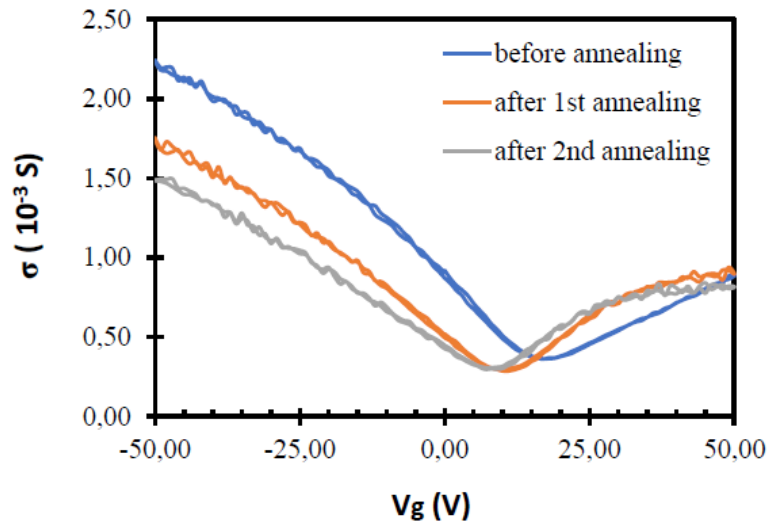


Figure 4.3. Conductivity curves of the device realized on sample 3 before the annealing (blue line), after a first annealing at 100 °C for 1 hour (orange line) and after a second annealing at 110 °C for 1 hour (grey line). It is possible to see that whereas the Dirac point appears to be shifted after the annealing, the mobility of the electrons seems to saturate at high voltages.

Table 4.3. Characteristics of the device realized on sample 3 before the annealing, after the first annealing of 1 hour at 100 °C and after the second annealing of 1 hour at 110 °C.

	Before annealing	After 1h at 100°C	After 1h at 110°C
μ_e [cm ² /Vs]	1739	2609	2609
μ_h [cm ² /Vs]	3478	2609	1739
Dirac point [V]	19	9	7
Impurities released [cm ⁻²]		7,19E+11	1,44E+11

The lower mobility of this sample compared to the other analysed can be partly attributed to it being one of the first chronologically produced samples, when the correct protocol wasn't fully assimilated. Whereas studies such as [75] suggest that the dominant scattering factor are charged impurities, studies such as [76] argue that for higher gate voltages the contribution of the scattering due to charged impurities should decrease. Additionally, according to [77] and [78] the mobility of graphene over silicon-silicon dioxide substrate should not be mainly influenced and limited by the presence of charged impurities, which would be mainly responsible only for the shift of the neutrality point of the specimens. Instead, for devices which a mobility higher than $1000 \text{ cm}^2/\text{Vs}$, such as the devices here analysed, long-range scattering of flexural phonons is suggested to influence the mobility. Those flexural phonons could arise within ripples which are often present in mechanically cleaved graphene [79]. These ripples are supposedly created during the micromechanical cleavage when the graphene flake is not able to remain completely flat during the transfer from the tape to the silicon substrate. In the case of flakes attached to thicker flakes, as is the case with this sample, its ability to flatten itself could be further compromised, thus leading to lower mobility values. These ripples could also have been accentuated by the roughness of the spin-coated HMDS, to which the graphene would be accommodating as reported in [74], which could be more pronounced in the first samples realized, and which cannot be precisely controlled using a technique such as spin coating.

The device realized on sample 14 resulted to be of higher quality, as can be seen from the fact it was only slightly *n*-doped (the Dirac point initially was at -3 V) and presented a much higher mobility. It was isolated but presented a more triangular shape (Figure 4.4).

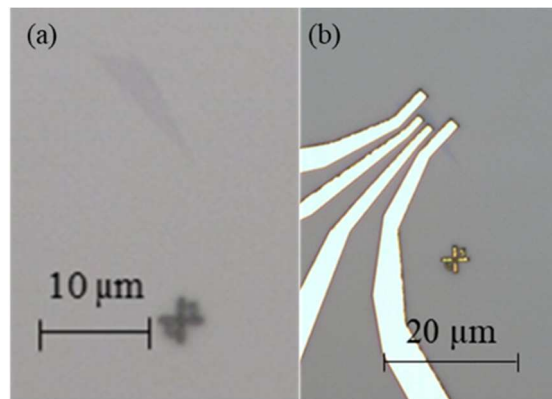


Figure 4.4. Details of the device realized on sample 14 at the OM. (a) the target as seen after the etching of the Reg marks, (b) the device after the deposition of the electrodes before being tested.

After the first measurement (in blue in Figure 4.5) it is reasonable to think that there were some electron donor impurities absorbed due to the bulge present in the *n*-branch of the conductivity curve. Nevertheless, the mobility recorded for this sample was already much higher than the one recorded in the other samples, both for holes and electrons (Table 4.4). An annealing of 1 hour at 100°C was then performed after which the measurement was run again.

One can see in Figure 4.5 (orange line) that after the annealing the Dirac point was slightly shifted, being now at -2 V, and that the concavity of the curve was restored, meaning the impurities were eliminated from the surface of the device. Furthermore, the device now presented a symmetrical mobility for holes and electrons, as theoretically predicted for graphene [77], [80]. Unfortunately, one can also see that the device seems to saturate at low voltages after the annealing, maybe because of a slight degradation of it. This particularity of having a saturation of the carriers in the majority region was shown by almost all the devices tested and will be further analysed, taking into consideration all samples.

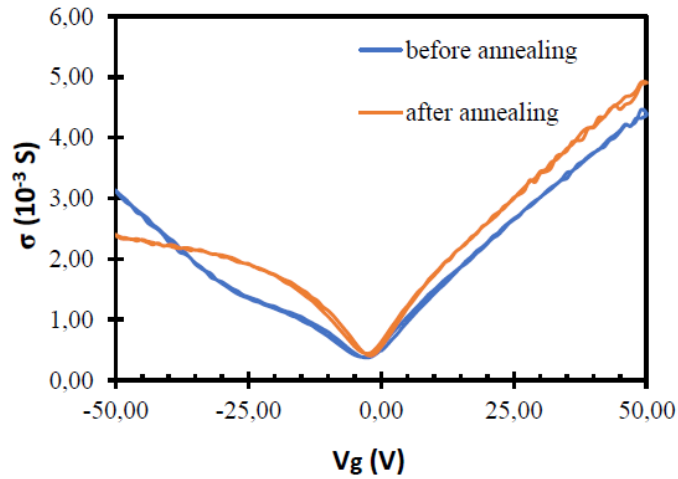


Figure 4.5. Conductivity curves of the device realized on sample 14 before the annealing (blue line), after an annealing at 100 °C for 1 hour (orange line). One can see that the concavity of the curve is restored after the annealing, this having resulted in the desorption of some electron donor impurities.

Table 4.4. Characteristics of the device realized on sample 14 before the annealing and after the annealing of 1 hour at 100 °C.

	Before annealing	After 1h at 100°C
μ_e [cm ² /Vs]	6956	8696
μ_h [cm ² /Vs]	5217	8696
Dirac point [V]	-3	-2.5
Impurities released [cm ⁻²]		3,59E+10

The devices realized on sample 15 were respectively monolayer (Figure 4.6) and bilayer (Figure 4.8) and both were isolated from any graphite flake. The particularity of these two devices is that after being annealed, both devices showed a shift of the Dirac point to lower voltages and an increase of the mobility of the electrons, indicating the annealing was conducted successfully, but at the same time the mobility of the holes that was quite high before the annealing was greatly decreased, almost to half of its original value (see Table 4.5 and Table 4.6).

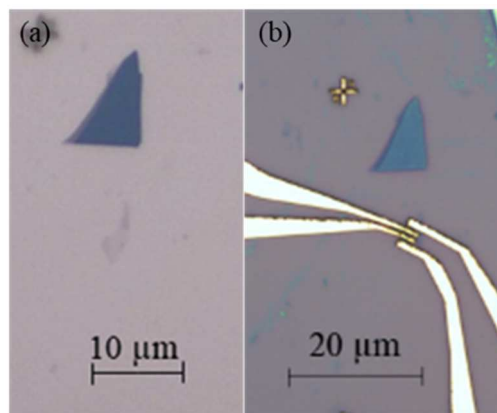


Figure 4.6 Details of the monolayer device realized on sample 15 at the OM. (a) the target as seen after the etching of the Reg marks, (b) the device after the deposition of the electrodes before being tested.

The conductivity curves of the monolayer device are shown in Figure 4.7. One can see that before the annealing both curves (in blue) present a bulge in the positive voltages region, which is more evident in the two-terminal measurement curve than in the four-terminal one, which is eliminated after the annealing. However, this bulge appears in the negative voltages region after the annealing with the same intensity as before the annealing. This could suggest that some electron acceptor impurities that were desorbed during the annealing were re-absorbed during the same annealing or during the cooling down of the sample as electron donor impurities, resulting in the lowering of the hole mobility. However, since the treatment was performed under high vacuum (10^{-7} Torr) it is unknown why such impurities should have been re-absorbed and why on the other branch of the curve, since theoretically nothing was present or introduced in the chamber that could have modified said impurities.

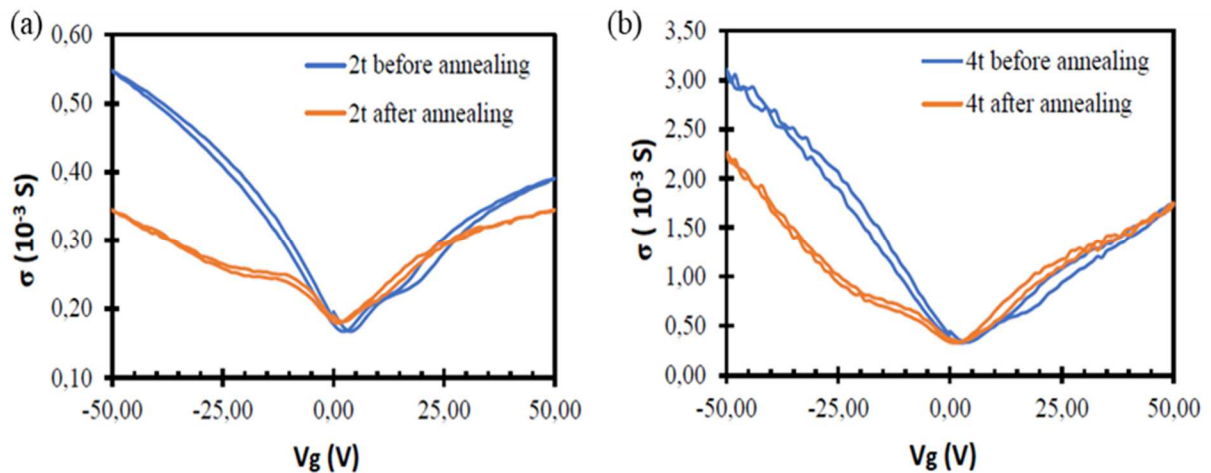


Figure 4.7. Conductivity curves of the monolayer device realized on sample 15 from (a) two-terminal and (b) four-terminal measurements before the annealing (blue line), after an annealing at 100 °C for 1 hour (orange line). One can see that whereas the mobility of the electrons increases after the annealing, the one of holes greatly decreases and the bulge passes from the positive voltages region to the negative voltages region.

Table 4.5. Characteristics of the monolayer device realized on sample 15 before the annealing and after the annealing of 1 hour at 100 °C from the two-terminal and the four-terminal measurements.

	Before annealing (4t measurement)	After 1h at 100°C (4t measurement)	Before annealing (2t measurement)	After 1h at 100°C (2t measurement)
μ_e [cm ² /Vs]	2609	3478	435	435
μ_h [cm ² /Vs]	5217	2609	870	522
Dirac point [V]	3.5	1.5		
Impurities released [cm ⁻²]		1,44E+11		

We now go on analysing the BLG device that was realized on sample 15. The graphene flake was isolated, as it is preferable, but presented quite an irregular shape (Figure 4.8). Nevertheless, electrodes were drawn to assimilate it to a rectangular shape.

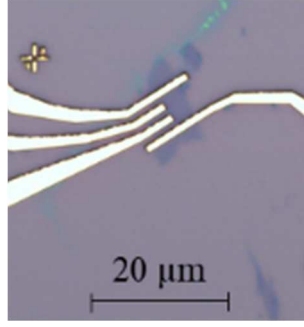


Figure 4.8. Detail at the OM of the bilayer device realized on sample 15.

The same behaviour of the monolayer device was observed on the bilayer device realized on the same sample (Figure 4.9), thus confirming the hypothesis about the re-absorbance of some of the impurities released during the annealing of the sample. One can also see that in the case of bilayer graphene the curve is not as sharp as the monolayer case but presents a more parabolic shape, as theoretically predicted [12], [8].

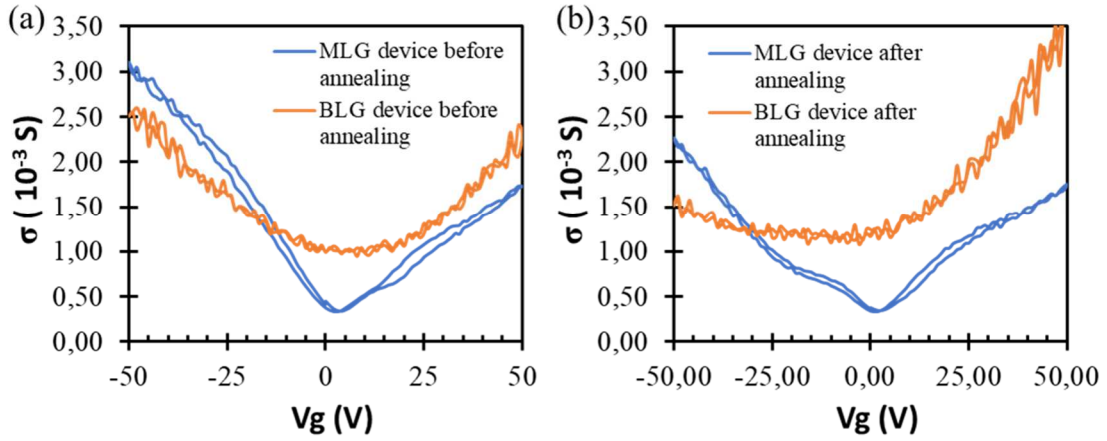


Figure 4.9. Comparison of the conductivity curves of the MLG and BLG devices realized on sample 15 (a) before and (b) after the annealing treatment at 100°C for 1 hour. One can see that during the annealing some impurities were absorbed in both samples, thus decreasing the conductivity values.

Let us introduce the crystal structure of the bilayer graphene to better understand where this shape arises from. The crystal structure of bilayer graphene consists of two coupled monolayers of honeycomb arranged carbon atoms. Each unit cell contains not two, as in the monolayer case, but four atoms: in the Figure 4.10 atoms A1 and B1 are on the lower layer whereas A2 and B2 are on the upper layer. One can see that whereas A2 and B1 are directly one above each other, the same cannot be said about A1 and B2. This gives rise to a strong interlayer coupling for the first pair, whose sites are called a “dimer sites”, differently from the other pair whose sites are called “non-dimer sites”.

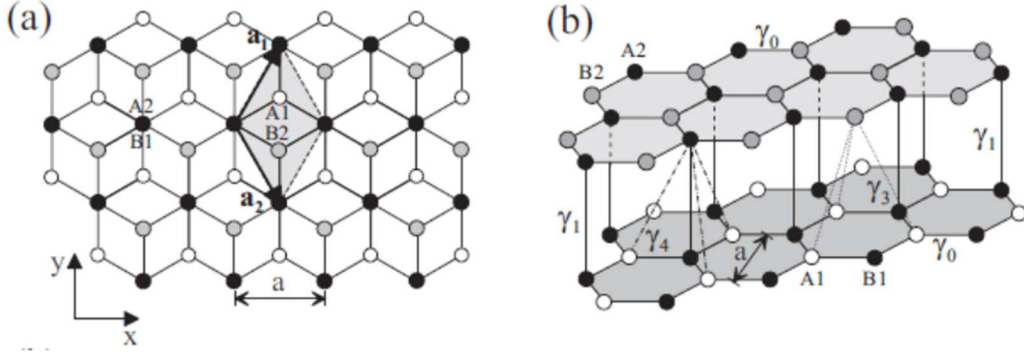


Figure 4.10 (a) Plan and (b) side view of the graphene bilayer structure. The lower layer sites are called A1 and B1, whereas the upper layer sites are called A2 and B2. One can see that A2 and B1 sites, in black circles, lie directly one under the other, whereas the atoms A1 and B2, indicated in white and grey circles respectively, are shifted from one another. The shaded rhombus in (a) indicates the unit cell, whereas γ_{0-4} are the coupling parameters [81].

This asymmetry between the two layers causes the appearance of non-diagonal terms both in the low-energy Hamiltonian transfer integral matrix and in the overlap integral matrix of the tight-binding model [20], [81], [82]. By solving the secular equation, one obtains the band structure of bilayer graphene reported in Figure 4.11. One can see that there are four bands present, a couple of valence bands and a couple of conduction bands which are mostly spaced by an energy of the same order of the interlayer spacing. The quadratic dispersion of energy of bilayer graphene can be explained with massive chiral quasiparticles, instead of massless ones like in monolayer graphene. The chirality of the charge carriers also gives rise to an anomalous quantum Hall effect in bilayer graphene which is different from the monolayer case. In the bilayer case there is an eightfold degeneracy of the zero-energy Landau-level, which had been anticipated in paragraph 1.2.2.

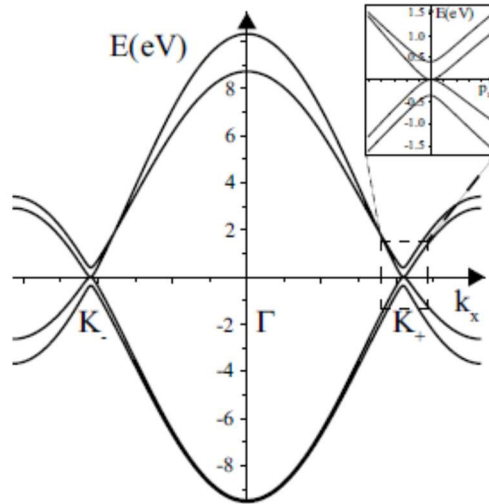


Figure 4.11. Low-energy bands of bilayer graphene, Γ is the centre of the Brillouin zone whereas K_+ and K_- are the two inequivalent points at the border of the Brillouin zone. The inset shows the vicinity of the K_+ point [81].

Going back to the curves obtained for the conductivity measurements of the bilayer samples of Figure 4.12, one can see that the curves present a parabolic shape, which is more evident in the two-terminal

measurement than in the four-terminal. It is possible to see that after the annealing the shift of the Dirac point was significantly reduced, even placing it to negative voltages, passing from +10 V to -3 V (Table 4.6). Furthermore, one can see the asymmetry between the electron and the holes branch, which is more accentuated than in the monolayer cases. This asymmetry arises directly from the interlayer coupling between non-dimer and dimer sites [81]. The reason of such a decrease of the hole mobility after the annealing treatment, which almost seems a rotation of the curve, however, is an anomaly that we are not currently able to explain.

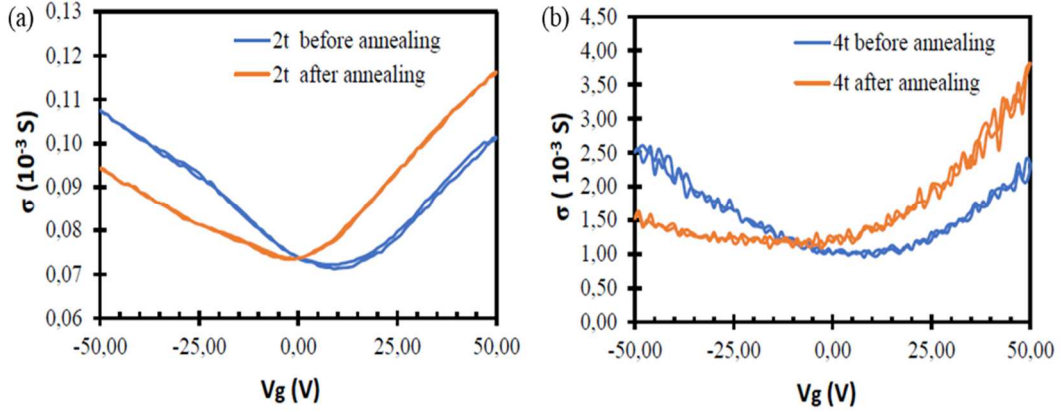


Figure 4.12. Conductivity curves of the bilayer realized on sample 15 from (a) the two-terminal and (b) the four-terminal (right) measurements before the annealing (blue line), after an annealing at 100 °C for 1 hour (orange line).

Table 4.6. Characteristics of the bilayer device realized on sample 15 before the annealing and after the annealing of 1 hour at 100 °C from the two-terminal and the four-terminal measurements.

	Before annealing (4t measurement)	After 1h at 100°C (4t measurement)	Before annealing (2t measurement)	After 1h at 100°C (2t measurement)
μ_e [cm ² /Vs]	3478	4348	78	78
μ_h [cm ² /Vs]	2609	609	70	35
Dirac point [V]	10	-3		
Impurities released [cm ⁻²]		9,34E+11		

Lastly, let us consider the saturation of the conductivity that all the devices presented for the majority carriers. All the monolayer devices analysed presented this kind of saturation which can be more or less pronounced, but always present, whereas in the bilayer device one could not spot it. This saturation is well known in the literature, as shown by the results of [83] in which a pronounced saturation of the conductivity in monolayers graphene is treated as a normal phenomenon. Studies like [75] assert that for high quality samples, the mobility should be limited by the presence of point defects. In such a case, the conductivity should become almost constant, differently from when the charged impurities are the limiting scattering factor causing an almost linear conductivity. However, this hypothesis does not seem in agreement with the fact that all our samples show this saturation of the conductivity after the annealing, and not only the high-quality devices realized on sample 14. The asymmetry of the two branches of the conductivity curves in the monolayer samples could be explained according to [76] with the difference between attractive and repulsive scattering of the massless Dirac fermions. Another factor that needs to be taken into account is the influence of the electrodes and the metal contact with the graphene specimens that could cause a charge transfer from the electrodes to the target. According to [84] and [85] in the case of metal contacts of relative big dimensions, which is the case of our devices, a carrier injection from the edge of the contacts to the graphene target can occur. If some electron acceptor

molecules are included at the interface between the target and the metal layer a charge density depinning can cause the distortion seen in the positive gated region. This effect is mostly seen in invasive electrodes both in a two-terminal and in a four-terminal geometry.

4.2 LOL-NSG devices

The SG devices were tested before exposing them to UV light in order to see whether it was possible to draw a comparison between devices in which only the hydrophobic coating over the gate oxide was different. After conducting the first two-terminal measurements we noticed that all of the devices realized over the LOL coating layers seem to be heavily *p*-doped, thus resulting in a Dirac point shifted to voltages higher than 40 V (Figure 4.13). This seemed in accordance with what was observed in [26], from which the proceedings are taken, and in [30], where graphene in contact with a photoresist layer resulted heavily *p*-doped. Nevertheless, we weren't able to assess at that point whether the devices were actually heavily doped, the presence of the resist induced the shift of the Dirac point, or both factors had to be weighted.

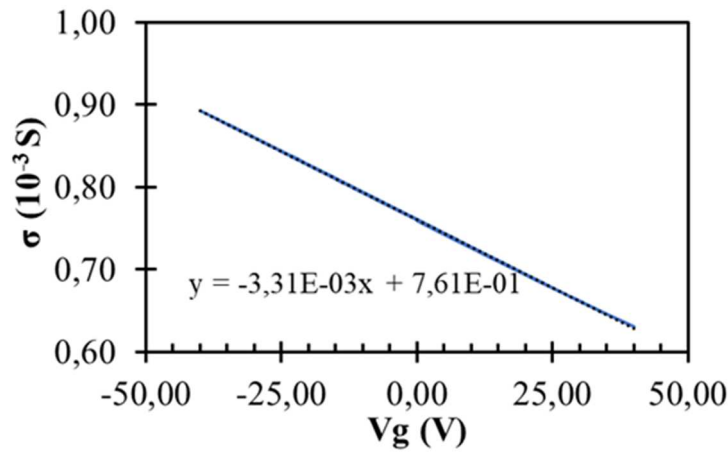


Figure 4.13. Conductivity curve of one of the devices tested before being suspended. One can see that the Dirac point does not appear in the range of voltage tested, thus resulting in a heavily *p*-doped device.

In order to draw a comparison between the NSG devices and the LOL-NSG devices one has to take into account the same kind of measurements for both kind of samples. This is because the results can vary for the same measurement if one considers a four-terminal or a two-terminal measurement due to the influence of the contact resistance which is not taken into account in two-terminal measurements. Hopefully one can obtain both four-terminal and two-terminal outputs when performing a four-terminal measurement. One can see in Figure 4.14 that based on the type of measurement the results obtained for the same sample can vary of almost one order of magnitude, being 3478 cm²/Vs and 783 cm²/Vs the hole mobilities obtained respectively from the four-terminal and the two-terminal measurements on the NSG device on sample 3. The results of the two-terminal measurements on the NSG devices are listed in Table 4.7.

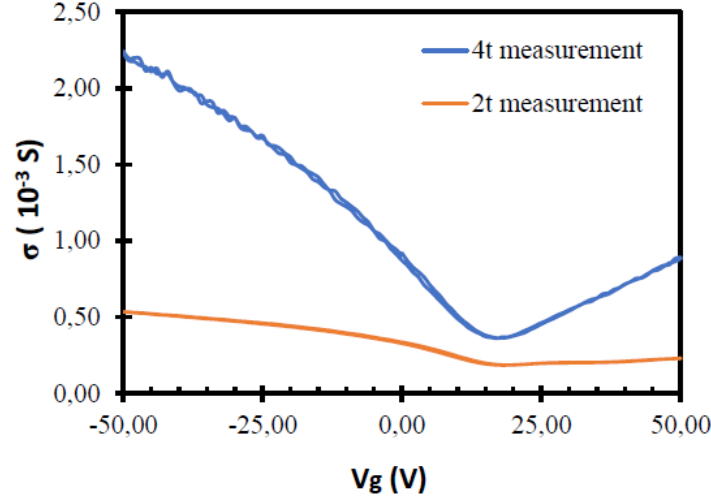


Figure 4.14. Comparison between the results of the two-terminal (in orange) and the four-terminal (in blue) measurements of the same sample. One can see that there can be more than one order of magnitude of difference due to contact resistance which is not taken into account in the two-terminal measurement.

Table 4.7. Characteristics of the mechanically exfoliated NSG devices obtained from two-terminal measurements. The hole mobility data are considered before the annealing to draw a more effective comparison with the LOL-NSG devices.

Sample #	Number of layers	Channel length, μm	Channel width, μm	$\left \frac{d\sigma}{dV_g} \right $	Mobility (cm^2/Vs)
3	Monolayer	5.00	3.04	9.00 E-6	783
14.3	Monolayer	5.00	2.06	3.00 E-5	2609
15.2	Monolayer	2.50	1.96	1.00 E-5	870
15.1	Bilayer	5.00	7.11	8.00 E-7	70

The results from the two-point measurements on the suspended devices before the suspension are listed in Table 4.8. One can see that a high dispersion is displayed as far as the value of mobility is concerned. Two main causes can be accounted for this result, the first being the fact that the number of layers of the LOL-NSG devices is not known at the stage of the measurement, and the second being the high influence of the contact resistance in this kind of measurement. The totality of the conductivity curves for each sample is presented in the Supporting information 4. Infographic of the mechanically exfoliated LOL-NSG devices

For each measurement the value of $\left| \frac{d\sigma}{dV_g} \right|$ and a mobility were recorded. The values of mobility were first calculated with the capacitance of the substrate of silicon coated with 300 nm of silicon dioxide, as was done for the NSG devices. However, due to the thickness of the LOL coating, which should be around 1.3~1.5 μm one should also consider its contribution to the overall capacitance of the system. The thickness of the LOL layer was then measured with a surface profiler and resulted to be equal to 1.3 μm . The relative permittivity of the LOL coating was calculated from the refractive index for UV light reported on the datasheet of the compound and resulted to be equal to 2.5. The capacitance of the LOL layer on the silicon substrate was then calculated to be equal to $1.70 \times 10^{-9} \text{ F cm}^{-2}$.

The overall capacitance of the LOL and oxide layer was then calculated with the equation (4.3) since the two layers appear to be in series and resulted to be equal to $1.48 \times 10^{-9} \text{ F cm}^{-2}$, which is of the

same order of magnitude of what reported in [26]. We then decided to list both the values of the slope of the conductivity curves and the mobilities resulting from this gate capacitance.

$$C_{tot} = \frac{C_{LOL} * C_{ox}}{C_{LOL} + C_{ox}} \quad (4.3)$$

Table 4.8. Characteristics of the 26 LOL-NSG devices obtained from two-terminal measurements. Whenever it was possible to draw two different sets of two-terminal measurement electrodes, multiple measurements were performed. Those are specified in parenthesis.

Sample #	Channel length, μm	Channel width, μm	$\left \frac{d\sigma}{dV_g} \right $	Mobility (cm^2/Vs)
6.1	0.88	6.51	2.98 E-11	0.02
6.2	1.99	23.60	2.31 E-07	156
6.3	1.92	14.67	4.43 E-07	299
6.4	1.94	48.08	9.78 E-09	7
7.1	10.50	23.33	3.03 E-07	205
7.2	2.00	15.72	5.54 E-07	375
7.3	9.77	9.78	3.31 E-06	2236
7.4	7.68	11.19	4.08 E-10	0.27
8.1	7.41	8.47	4.30 E-07	290
8.2	6.00	14.94	1.48 E-07	101
8.3	7.06	5.84	1.05 E-07	71
9.1 (1)	1.50	4.39	1.89 E-07	128
9.1 (2)	1.00	4.93	1.36 E-07	92
9.3	1.00	5.60	3.32 E-07	224
9.4	1.50	9.89	4.20 E-07	284
9.5	1.00	2.30	1.77 E-07	120
9.6	2.00	7.25	3.45 E-07	233
9.7	1.50	5.34	2.31 E-07	156
9.8	1.00	1.95	2.11 E-07	143
9.9 (1)	1.50	15.79	3.71 E-07	251
9.9 (2)	1.00	9.78	2.40 E-07	162
9.10	1.44	6.78	2.05 E-07	139
10.1	1.50	3.33	4.02 E-07	272
10.2	1.60	60.00	9.73 E-07	657
10.3	1.50	17.56	1.31 E-06	886
10.3b	1.00	7.18	1.81 E-06	1222
10.4	1.00	2.22	1.74 E-07	118
10.5 (1)	2.00	4.49	9.36 E-09	6
10.5 (2)	2.00	2.82	1.95 E-08	13

While looking at the values of the slope of the conductivity curves, a few recurrent values can be recognized. These are summarized in Table 4.9, although the values that were accounted as being unreliable (lower than 10^{-8}) were not taken into consideration. One could be led to think that those values are each to be accounted for a specific number of layers of the specimen, but the measures of the NSG devices which were more precise showed how much dispersion of data can be encountered even in samples with the same number of layers, so this kind of identification cannot be performed. Furthermore, the optical contrast between the various samples was not as marked to as to suggest such a high variety

of thickness of the targets. As a term of comparison, one can see in Figure 4.15 the optical image of the devices 7.3, 8.1 and 10.5 (at the top of the image) which present respectively $\left| \frac{d\sigma}{dV_g} \right|$ of 3.00 E-06, 4.00 E-07 and 2.00 E-08 but that from the optical contrast would seem almost the same thickness.

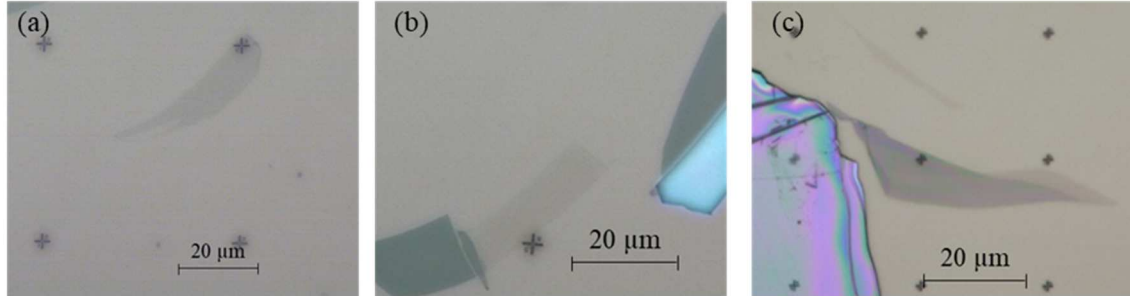


Figure 4.15. Optical images of the LOL-NSG devices (a) 7.3, (b) 8.1 and (c) 10.5.

Nevertheless, one can see in Table 4.9 that even the higher values that supposedly could be of the monolayer devices still are considerably smaller than those reported for NSG devices measured with a two-terminal measurement.

Table 4.9. Distribution of the slope of the conductivity curves of the mechanically exfoliated LOL-NSG devices.

$\left \frac{d\sigma}{dV_g} \right $	1E-8	2E-8	1E-7	2E-7	3E-7	4E-7	6E-7	1E-6	2E-6	3E-6
count	1	1	3	8	3	5	1	2	1	1

These results could lead to the conclusion that LOL is a good hydrophobic layer only if one wants to later suspend the devices. Otherwise the mobility of the graphene is decreased, sometimes by more than one order of magnitude, the Dirac point appears to be shifted to voltages higher than 40V and one cannot assess the number of layers of the targets by using the optical contrast.

However, in order for such a statement to acquire some foundation one should first measure, amongst others, the roughness of the LOL layer. In fact, since the LOL coating is performed in five spin-coating steps, one can reasonably assume that the surface will present quite a pronounced roughness that is likely to greatly influence the value of the mobility of the targets. Since this kind of measurements and assessments were beyond our possibilities during the work related in this paper, we will limit ourselves to notice the recurrence of the values of the slope of the conductivity curves. Ellipsometry was envisioned as a possible technique to determine the thickness and roughness, although one has to be careful when measuring the thickness of the LOL due to its layered structure. It is indeed possible that during the baking of each successive coating some impurities may have been absorbed, thus resulting buried in the LOL thickness at the end of the process. Such inclusions in the layered material could cause some interference and some difficulty could arise in the measuring of the thickness of the hydrophobic layer [84].

4.3 SG devices

Several problems arose during the preparation of the suspended devices, leading to the conclusion that an analysis of the problems and complications of their realization could be more time efficient and helpful to the laboratory for their craft in a near future than the successful realization of those samples in such a short period of time.

After the preparation of the first suspended devices we realized that the preparation of a four-terminal suspended device was too difficult in a first stage and switched to two-terminal devices. This was because in the four-terminal configuration one was not able to assess whether the device had been successfully suspended or not (Figure 4.16).

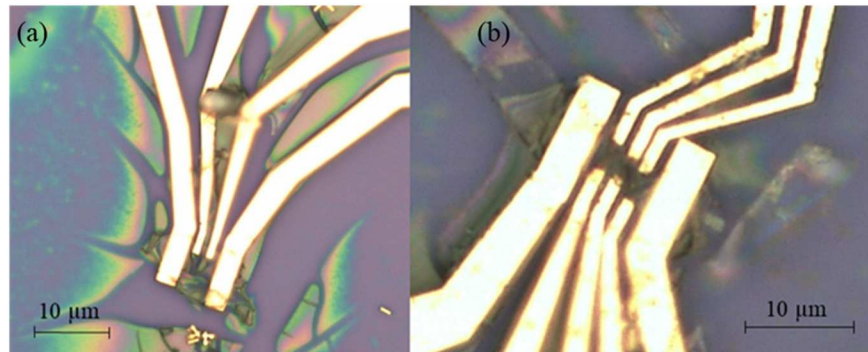


Figure 4.16. Details at x1000 of two devices of SG with the initial electrodes geometry after being suspended. From an observation at the OM one is not able to determine whether the suspension was successful or not due to the collapse of the flake at the edges.

Two-terminal measurements do not provide information as precise nor reliable as the four-terminal ones but can be a useful tool to assess whether or not the devices were realized successfully and to have a first indicative idea of the mobility of said devices. The final goal still was to complete four-terminal suspended devices. In this configuration, further supports for the suspended part were drawn next to the electrodes to mask the LOL underneath the graphene from the UV exposure, as in Figure 4.17.

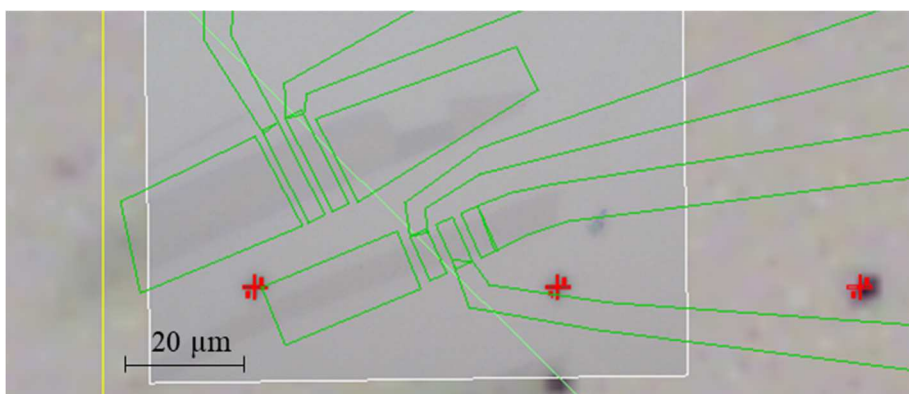


Figure 4.17. Detail of the CAD file of one of the mechanically exfoliated SG samples. We can see that the configuration is for a two-terminal measurement and that aside from the electrodes some masks are drawn to cover the rest of the graphene specimen from the UV radiation. This is done to improve the strength of the graphene flake and reduce the probability of collapse. The space between two Reg-3 marks is 50 μm .

The lateral masks should increase the flexural strength of the graphene flake. As can be seen in Figure 4.18, the graphene flake tends to bend and to collapse onto the silicon layer when it is suspended as a result of the flexural bend induced by its own weight. The lateral supports should prevent or at least reduce the risk of collapsing by relieving some of the flexural stress supporting most part of the graphene flake and should also prevent the crippling of the graphene edges.

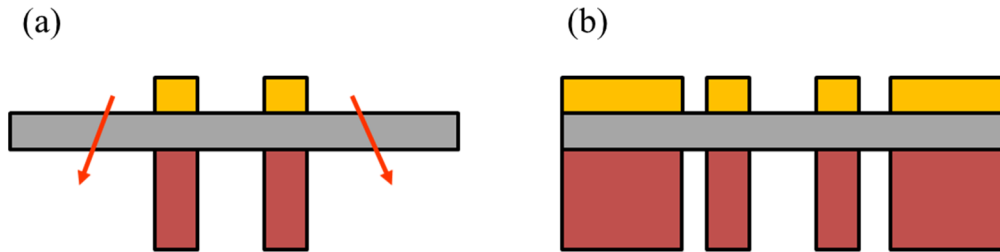


Figure 4.18. Schematic of the behaviour of the graphene flake suspended. In (a) the graphene bends and collapses due to its own weight, in (b) the lateral supports prevent part of the collapse.

Another problem that arose during the preparation of the mechanically exfoliated SG devices was the complete removal of the photoresist by mean of UV exposure. Some of the samples, being subjected to the same preparation of the devices, the same deposition of the electrodes and the same UV exposure parameters did not present a complete etching of the LOL layers. Instead they presented a cracked surface of remaining LOL degraded, as can be seen in Figure 4.19, thus preventing further analysis of the devices.

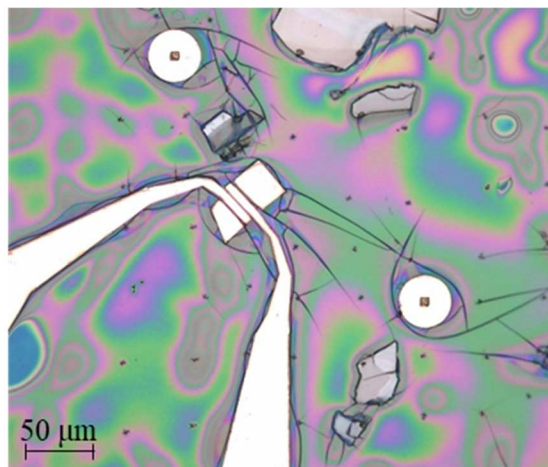


Figure 4.19. Picture taken at the OM with a magnitude of x200 of one of the samples where the etching of the LOL layers was not complete.

Several possible causes of such effect were taken into account in order to prevent it from happening to the other devices.

At first a degradation of the LOL layers was considered due to the long time that had passed between the first realization of the sample and the UV exposure. As a matter of fact, the sample had been prepared several weeks prior to the deposition of the electrodes and the subsequent lift-off and UV exposure. However, the observation of the sample after the deposition of the electrodes and before the UV exposure did not show any of the aforementioned cracks and presented a perfectly clear surface (Figure 4.20).

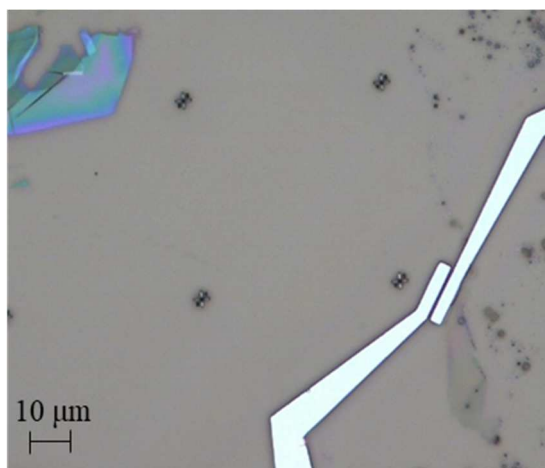


Figure 4.20. Details at the OM with a magnitude of x500 of one of the devices after the deposition of the electrodes and the lift-off process but before the UV exposure. One can see that the surface of LOL is smooth, and no cracks appear to be present. The space between two Reg-3 marks is 50 μm.

A blank sample was then prepared to definitely assess whether the LOL could be degraded due to the waiting time before its etching. A new substrate was consequently sonicated in acetone and methanol like the samples and coated with five layers of LOL, then exposed to UV light with a mask made of aluminium foil. The observation of the same crevices in the blank sample (Figure 4.21) just prepared allowed us to rid the long waiting time as the cause of cracks.

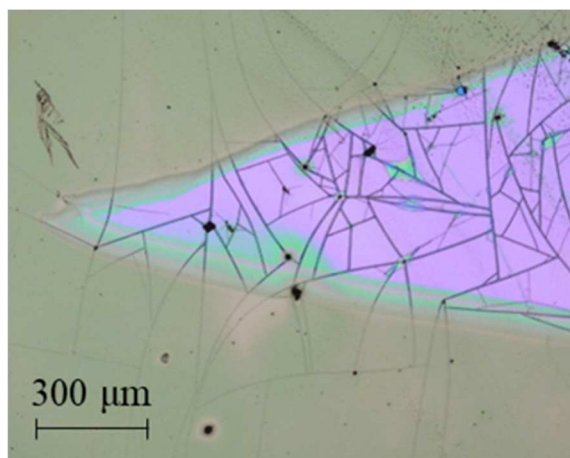


Figure 4.21. Observation at the OM with a magnitude of x50 of the blank sample after the exposure. One can see that the pattern exposed by the mask has changed colour becoming reddish instead of yellow and is only partially etched (otherwise we could see the silicon substrate). The crevices are both present in the exposed part and in the non-exposed part.

A second factor that was taken into account was the exposure time. The 10 minutes had been successfully used for previous samples such as the first attempts at realizing suspended devices, but several factors could have influenced it like a reduction of the power of the lamp or a reduction of the sensibility of the resist used. Several blank samples were consequently realized and exposed for increasing amounts of time in order to assess which exposure time could be optimal for the current situation (see Supporting information 5. Study of the exposure time). A first sample was exposed for only 5 minutes, following the supposition that the exposure time could be too long. This seemed unrealistic since, if that had been the case, one should have observed no resist left at all on the sample, even under the electrodes of the devices which were masked by the chromium and gold electrodes.

Nevertheless, observations were conducted to draw a comprehensive study of the exposure time. The observations at the OM before and after the development and allowed us to determine that the cracks were indeed present after the development (Figure 4.22) and the resist was still remaining.

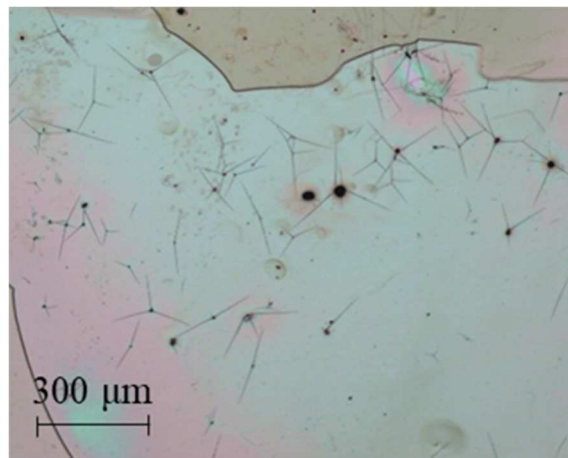


Figure 4.22. Observation at the OM with a magnitude of x50 of the blank sample after the exposure. One can see the beginning of the cracks both in the part etched and in the one not etched.

Longer exposure times were consequently taken into consideration. After assessing that 15 minutes was a long enough time to remove the LOL layers and reveal the silicon underneath (Figure 4.23 b), leaving only the non-exposed part with cracks, an intermediate time of 12 minute was tested (Figure 4.23 a). This resulted in a not ideal etching of the pattern, though the last coating of resist seemed really thin almost revealing the blue substrate underneath.

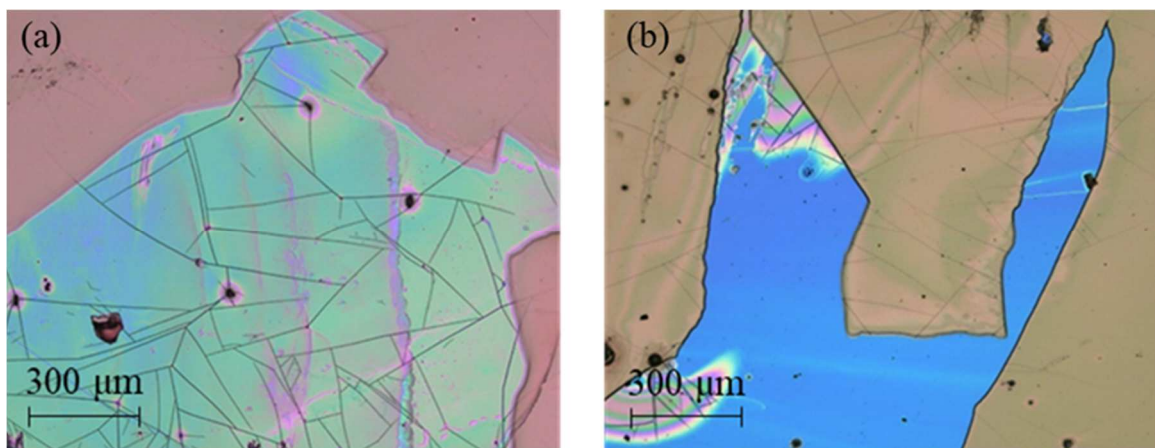


Figure 4.23. Observation at x50 at the OM of the blank samples exposed to UV for (a) 12 minutes and (b) 15 minutes. One can see that for 12 minutes cracks appear on the thin remaining resist layer, whereas for 15 minutes the resist is completely removed.

A second exposure of 5 additional minutes was then attempted on the samples already exposed for 10 and 12 minutes to assess whether the sample already exposed could be further tested. During this second exposure a different mask was used than the one for the first exposure (Figure 4.24). This allowed us to notice that in both samples the part completely etched was all the one of the first exposure, even if masked the second time, and not only the one subjected to the second exposure (Figure 4.25).

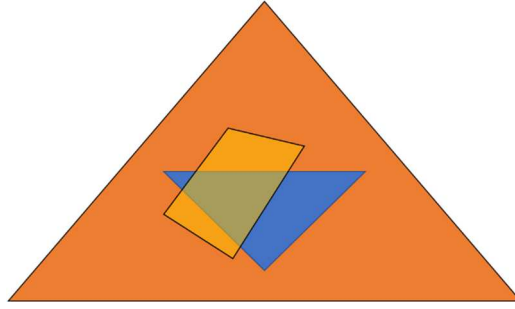


Figure 4.24. Schematic of the sample initially exposed for 10 minutes and later exposed for 5 additional minutes, with the colours observed at the OM. The mask used for the first exposure is drawn in blue, whether the one used for the second exposure is drawn in in yellow. After the development all the blue part was completely etched, while the yellow part was only partially etched.

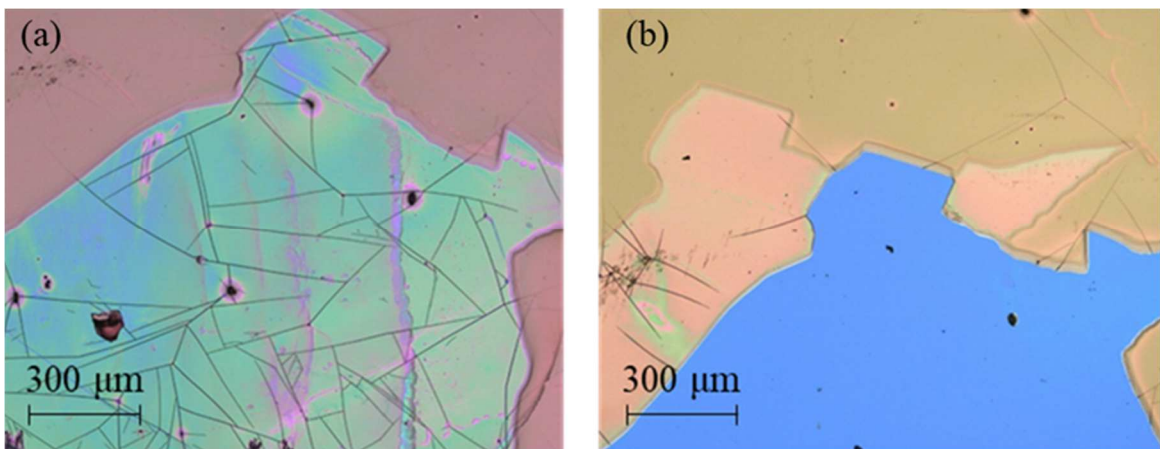


Figure 4.25. Observation at x50 at the OM of the blank sample exposed to UV for (a) 12 minutes and (b) 12 minutes plus 5 additional minutes. One can see that in the second case the shape of the first mask is completely etched even in the parts that were covered during the second exposure (whose shape is only partly etched).

The effect of the development time was subsequently taken into consideration, since a second development resulted in the complete etching of the samples previously exposed. The sample with the devices was then washed again in ethyl lactate for 1 minute and for 30 seconds in hexane. This resulted in a better etching of the resist, particularly near the devices and the electrodes, but most part of the resist still remained (Figure 4.26).

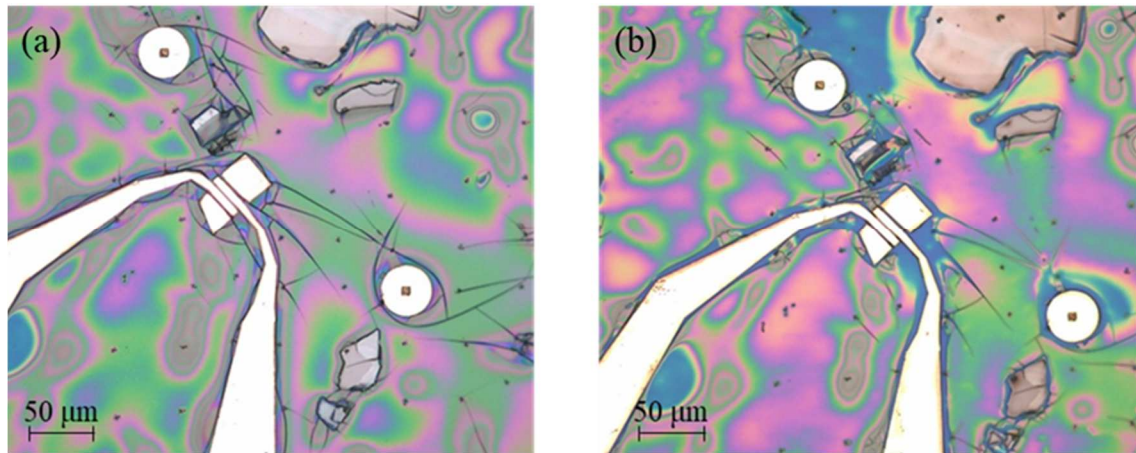


Figure 4.26. Observation at x200 at the OM of the sample after (a) the first exposure and development and (b) a second development. One can see that after the second development the resist appears to be more etched and the zones in the proximity of the electrodes are more etched.

A last blank sample was exposed for 12 minutes and then developed two times to assess the optimal exposure and development time for the present conditions of the equipment. The exposure time of 12 minutes was chosen after seeing that 10 minutes weren't enough in the sample and that the blank sample prepared earlier presented a very thin layer of residual coating. One can see in Figure 4.27 that after the first development the sample still presented a thin layer of resist, as previously observed in Figure 4.23, but that after a second exposure the resist was completely removed and the substrate exposed. The optimal protocol for exposure was then determined to be an exposure time of 12 minutes and a development time of 2 minutes in ethyl lactate and 1 minute in hexane.

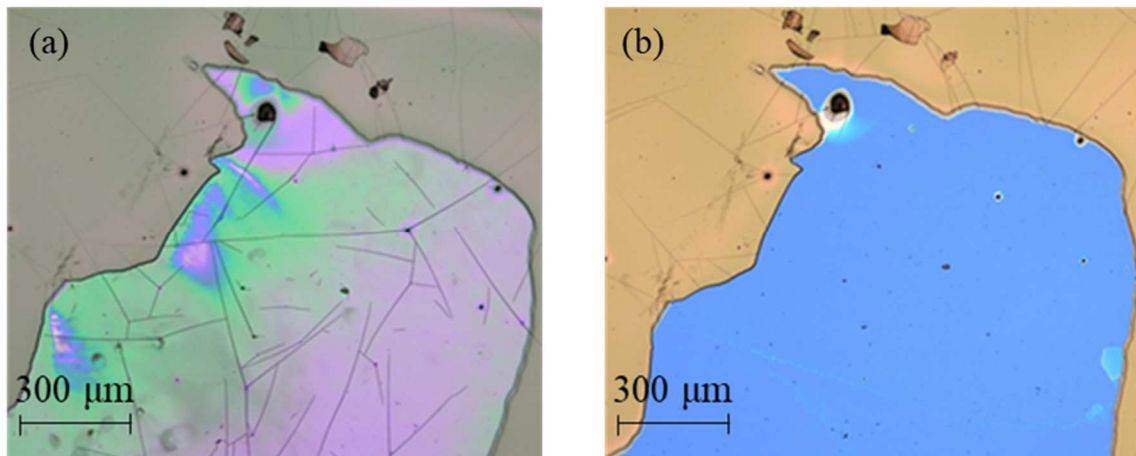


Figure 4.27. Observation at x50 at the OM of the blank sample exposed to UV for 12 minutes after (a) the first development and (b) a second development. One can see that in the second case the resist has been completely removed.

Since the development time seemed to have a bigger influence than the exposure time we attributed these effects mainly to a loss of sensitivity of the resist. Unfortunately, when the next sample was exposed and develop with what we thought was the optimized protocol, the resist wasn't completely removed and still remained near the devices, thus preventing us to assess whether the device was correctly suspended or not. Some of the devices, like the one in Figure 4.28, seemed to be isolated from the resist but the remaining resist distorted the contrast, thus resulting in us not being able to determine whether it was actually suspended, or some resist was supporting it.

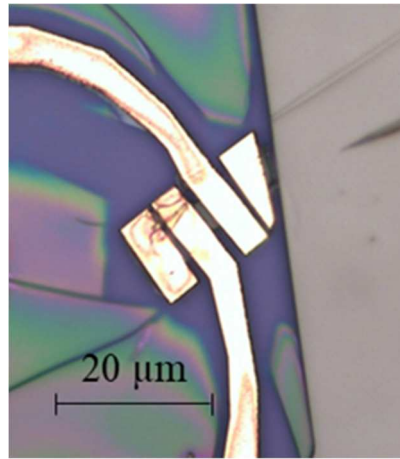


Figure 4.28. OM observation at x100 of one of the devices from the sample exposed for 12 minutes and subjected to a development of 2 minutes in ethyl lactate and 1 min in hexane. From the contrast one is not able to say whether the device has been successfully suspended or some resist still remains underneath the graphene.

In addition to that, the electrodes appear not to be planar anymore, but present some kind of valleys and ripples (Figure 4.29). The motive of such appearances has yet to be determined. At first one could think that those were caused by the removal of the resist underneath the electrode and a subsequent collapse of the metallic layer, but the wrinkles seemed to be higher than the level of the electrodes and one would think that the resist would be removed firstly from the edges and then in the centre of the electrodes. Another hypothesis taken into consideration was that an amount of resist was showed at the centre of the electrodes following the development. The cause of the ripples has yet to be determined.

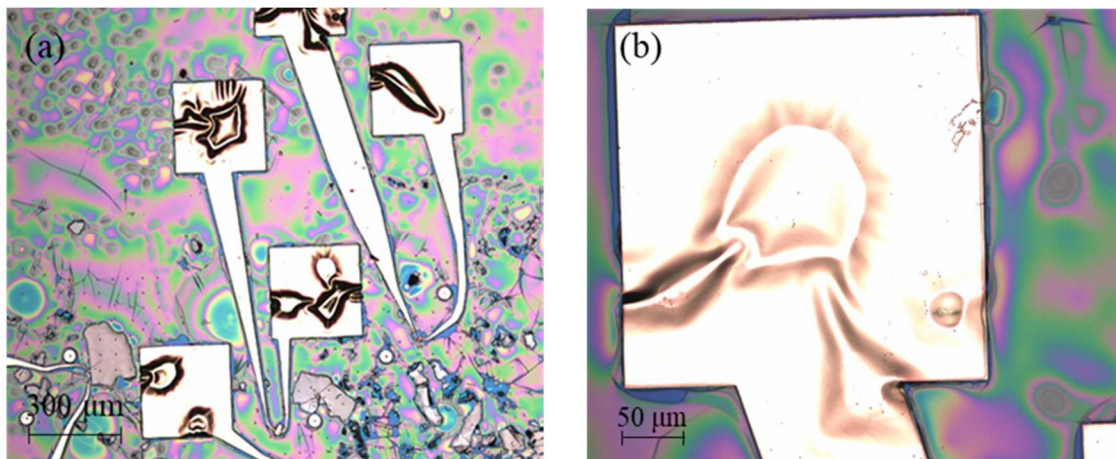


Figure 4.29. (a) OM observation at x5 of the devices after being exposed for 12 minutes and subjected to a development of 2 minutes in ethyl lactate and 1 min in hexane. One can see that the polymeric resist still remains present and that the electrodes present some deep wrinkles. (b) detail at x20 of one of the electrodes wrinkled.

5. Conclusions

The peculiar properties presented by graphene make it a very interesting subject for the electronic industry and are responsible for the steady interest in this 2D material which hasn't decreased in the almost 15 years since its discovery. In particular, one can remember the presence of massless chiral fermions in monolayer samples which can approach ballistic transport and the presence of anomalous half integer and integer quantum Hall effect respectively in monolayer and bilayer samples.

However, the realization of high quality devices is still subjected to high variables depending on the way the device is realized and of the synthesis technique applied to obtain graphene. In this work, several kinds of devices were realized with graphene mechanically exfoliated using the Scotch-tape technique, which is up-to-date the technique allowing one to reach the highest quality samples.

At first study was successfully conducted on traditional non-suspended devices. Those were realized by depositing graphene flakes over a hydrophobic layer of HMDS on a Si/SiO₂ 300 nm thick substrate previously washed by sonication. Three monolayer and a bilayer devices were prepared and then tested in a four-terminal configuration before and after undertaking an annealing treatment at 100°C in order to assess the evolution of their properties.

Although the quality of the monolayer samples was not homogeneous, the device realized on sample 14 being the one of highest quality and the only one presenting a slight *n*-doping, one can see in Figure 5.1 that the annealing was successful in all three cases and resulted in an improvement of the electron mobility of all three devices. A mobility as high as 8696 cm²/Vs was reached in sample 14 both for electrons and holes after the annealing treatment, thus showing the symmetry theoretically predicted for the two kinds of carriers and which is motivated by the presence of massless chiral fermions ([77], [80]). As for the smaller values of mobility for the other devices, several hypotheses were taken into consideration, ranging from the presence of ripples which would induce some kind of flexural phonons scattering [79], [74], to scattering of charged impurities [75], to human error during the preparation of the first samples. However, a univocal cause could not be determined, and further studies should be conducted in order to better assess these influences. Unfortunately, the annealing also resulted in a decrease of the holes mobility in the case of samples 3 and 15 and in the appearance of some saturation phenomenon in the case of all samples, which could result from a charge transfer from the electrodes to the graphene target [84], [85].

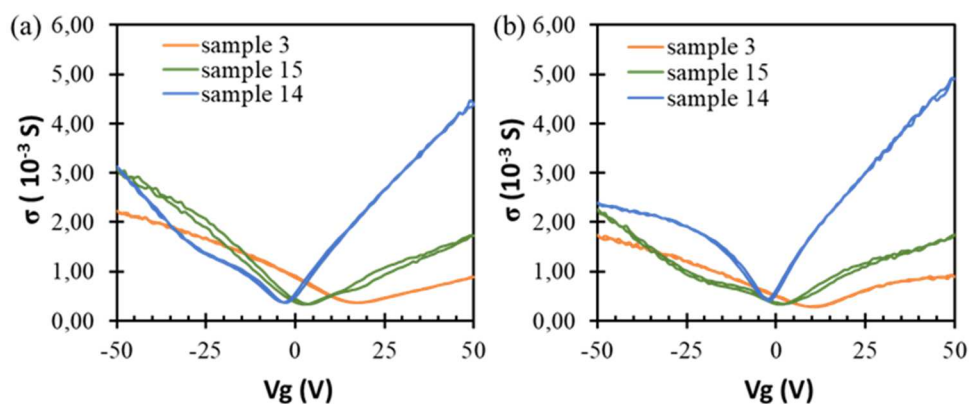


Figure 5.1. Comparison of the conductivity curves of the monolayer devices (a) before the annealing and (b) after completing the annealing of 1 hour at 100 °C.

A comparison between the behaviour of monolayer and bilayer devices was also conducted by analysing the two devices realized on sample 15 (Figure 5.2). We could then confirm that BLG devices present a parabolic curve instead of the linear one of the MLG devices in the vicinity of its Dirac point as theoretically predicted by [12] and [8]. Unfortunately, the annealing treatment of this sample resulted only in a partial improvement of the electron mobility and in a degradation of the other characteristics, as can be seen by the shape of the curves which is deformed and partially rotated in the case of the BLG device. This was attributed to the re-adsorption of some impurities released during the annealing. An absorption of some contaminants present in the chamber was also taken into consideration, but it seemed unlikely since during all the measurements and treatment the sample was under high vacuum.

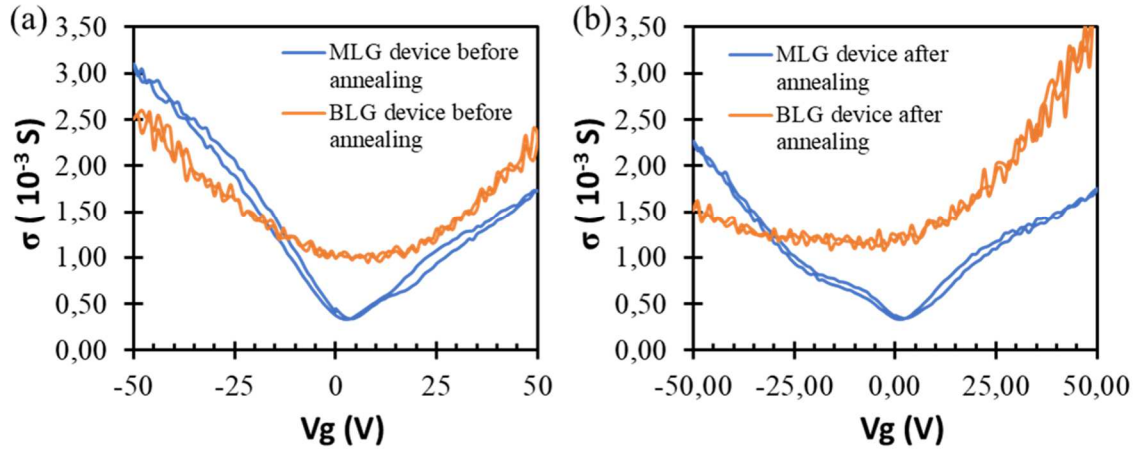


Figure 5.2. Comparison of the conductivity curves of the MLG and BLG devices realized on sample 15 (a) before and (b) after the annealing treatment at 100 °C for 1 hour. One can see that during the annealing some impurities were absorbed in both samples, thus decreasing the conductivity values.

The preparation of suspended graphene devices proved to be more difficult than expected and resulted in several unsuccessful attempts at realizing this kind of devices. Although the actual SG devices were not realized, several LOL-NSG devices were realized and tested to draw a comparison with the traditional NSG devices. Those were prepared by depositing the graphene flakes over a coating of LOL photolithographic resist instead of a layer of HDMS.

The testing of 26 LOL-NSG devices that presented different shapes and thicknesses of the graphene flakes allowed us to state that in the case of LOL-NSG devices the Dirac point of the devices is shifted to gate voltages higher than 40 V. However, we were not able to assess whether this shift was to be attributed to the presence of the thick layer of resist near and underneath the graphene specimens or was specific to the graphene flake in contact with it.

When comparing the mobilities of the NSG devices and the ones of the LOL-NSG devices, after having estimated the gate capacitance of the LOL layer on top of the oxide layer, we noticed that the values of the gate capacitances of the two kinds of devices were of the same order of magnitude. The mobilities of the NSG ones were higher than the LOL-NSG ones, at most of one order of magnitude, but not very far from the values of the medium quality devices. However, several factors were not taken into account and would thus need further analysis.

First of all, the number of the graphene layers of the LOL-NSG devices is unknown because we cannot determine it with the optical contrast due to the yellowish colour of the LOL layer. Raman spectroscopy had been considered as a way to assess it, but the presence of the organic layer underneath could influence the results. Further tests should also be conducted in order to estimate the roughness of the LOL layer. Ellipsometry was considered to evaluate it together with the thickness of the layer, to confirm the values obtained by surface profiler. A study on the thickness of the LOL layer could also provide some information on the role of the LOL layer in the shift of the Dirac point in this kind of devices. By

measuring the conductance of samples with variable LOL thicknesses one could be able to determine if the shift is due to the thickness of resist or not. The roughness of the LOL layer is a key factor of this analysis, since the layer is the result of five successive spin coating depositions and could highly influence the mobility of the carriers in the graphene due to the appearance of ripples and consequent flexural phonons.

Lastly, the LOL-NSG devices were exposed to deep UV violet to finalize suspended graphene devices. Unfortunately, the preparation of such devices was not successful but allowed us to optimize some of the steps of their realization. First of all, a new shape of the electrodes was designed in order to reduce the strains on the graphene flakes. The new design comprises two electrodes and some lateral masks to support the edges of the flakes and avoid the insurgence of ripples and folding (Figure 5.3).

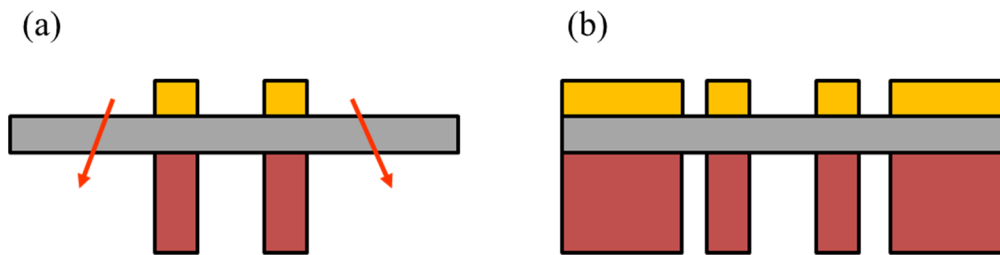


Figure 5.3. Schematic of the behaviour of the graphene flake suspended. In (a) the graphene bends and collapses due to its own weight, in (b) the lateral supports prevent part of the collapse.

A study was then undertaken to determine the optimal exposure time and development protocol after the first samples didn't respond to the previous protocol as they should have. After several trials on blank samples, the new protocol was determined to be an exposure of 12 minutes followed by a development of 2 minutes in ethyl lactate at room temperature, a rinse in hexane for 1 minute and a spray dry with a N_2 gun. Unfortunately, when applied to the samples of LOL-NSG devices this protocol was not successful, and we were not able to determine if the devices had been suspended or some resist was still underneath them. Furthermore, the electrodes appeared to be damaged by the appearance of some ripples and waves on their surface (**Figure 5.4**). The cause of these reliefs should be further analysed and a new and more accurate study on the suspension protocol should be conducted.

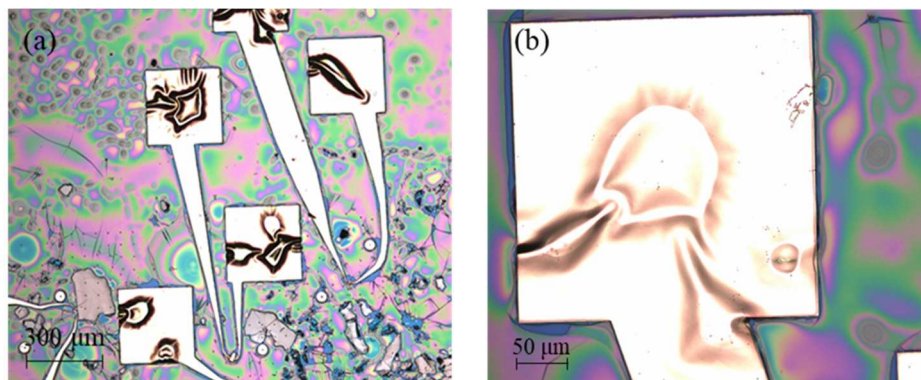


Figure 5.4. (a) OM observation at x5 of the devices after being exposed for 12 minutes and subjected to a development of 2 minutes in ethyl lactate and 1 min in hexane. One can see that the polymeric resist still remains present and that the electrodes present some deep wrinkles. (b) detail at x20 of one of the electrodes wrinkled.

The study of the two different kinds of devices allowed us to point out some of the properties that mostly appeal to the electronic industry. Although the realization of suspended graphene devices proved to be unsuccessful we were able to study the devices on the LOL layers and establish that the mobility of such non-suspended devices was not too far from the one of the more traditional NSG devices. The values reached in the LOL-NSG devices were nevertheless promising in the case of successful suspension of those devices. Therefore we believe that there is a need for further analysis and optimisation of the production process of suspended devices, whose architecture will have a fundamental role in the graphene research in the near future.

List of acronyms

Acronym	Full letter explanation
2-D	Two-Dimensional
AFM	Atomic Force Microscopy
Au	Gold
B	Magnetic Field, [T]
BLG	Bi-Layer Graphene
c	Speed of Light, [m s^{-1}]
C	Carbon
CAD	Computer Aided Design
CMOS	Complementary Metal Oxide Semiconductor
CNTs	Carbon Nanotubes
C_{ox}	Capacitance of the oxide, [F cm^{-2}]
Cr	Chromium
C_{sub}	Capacitance of the substrate, [F cm^{-2}]
CVD	Chemical Vapour Deposition
D peak	Raman peak from transversal optical phonons scattering
\mathcal{E}	Electrical field, [V m^{-1}]
ϵ_{Si}	Permittivity of Silicon, [F m^{-1}]
e, q	Elementary charge, [C]
EBL	Electron Beam Lithography
E_{C}	Conduction Band, [eV]
E_{F}	Fermi Level, [eV]
E_{i}	Intrinsic Fermi Level, [eV]
EL	Ethyl Lactate
E_{V}	Valence Band, [eV]
FET	Field Effect Transistor
FLG	Few Layer Graphene
FWHM	Full Width at Half Maximum
g	Additional system degeneracy
G	Conductance, [S]
G peak	Raman peak from in-plane vibration of high frequency phonons, [cm^{-1}]
G' peak	Raman peak from second order zone-boundary scattering phonons, [cm^{-1}]
Γ	Gamma point, centre of the Brillouin Zone
γ	Coupling parameter
G_{g}	Green peak of the graphene flake
GIC	Graphite Intercalated Compounds
GO	Graphite Oxide
G_{s}	Green peak of the substrate
H	Hydrogen
h	Planck constant, [$\text{m}^2 \text{kg s}^{-1}$]
HMDS	Hexa Methyl Di Silazane

HOPG	Highly Oriented Pyrolytic Graphite
I_D	Drain current, [A]
I_{Dsat}	Saturation drain current, [A]
I_G/I_G	Ratio of the intensities of the Raman peaks
IPA	Iso Propyl Alcohol
IQHE	Integer Quantum Hall Effect
ITO	Indium Tin Oxide
J_n	Drift current, [$A\ cm^{-2}$]
k	Boltzmann constant, [$m^2\ kg\ s^{-2}\ K^{-1}$]
K_+ , K_-	Dirac Points, inequivalent corners of the Brillouin Zone
l	Length, [μm]
L_D	Debye Length, [μm]
LOL	Lift-off layer, polymethylglutarimide
LOL-NSG	Non-Suspended Graphene over a LOL Coating
M	Centre of each rectangular face of the Brillouin Zone
m	Mass, [kg]
μ	Mobility, [$cm^2\ V^{-1}\ s^{-1}$]
μ_e	Electrons mobility, [$cm^2\ V^{-1}\ s^{-1}$]
μ_h	Holes mobility, [$cm^2\ V^{-1}\ s^{-1}$]
m_0	Effective mass, [kg]
MESFET	MEtal Semiconductor Field Effect Transistor
MIBK	Methyl IsoButyl Ketone
MLG	MonoLayer Graphene
MMA 8.5-MMA EL9	Copolymer 9% poly (Methyl MethAcrylate-co-Methacrylic Acid), dissolved in Ethyl Lactate
MOS	Metal Oxide Semiconductor
MOSFET	Metal Oxide Semiconductor Field Effect Transistor
MWNT	Multi Wall Nanotubes
n	Electrons concentration, [cm^{-3}]
N	Nitrogen
N_A	Acceptors density, [cm^{-3}]
N_D	Donors density, [cm^{-3}]
n_i	Intrinsic carrier concentration, [cm^{-3}]
NSG	Non-Suspended Graphene
O_2	Oxygen
OM	Optical Microscope
p	Holes concentration, [cm^{-3}]
PECVD	Plasma Enhanced Chemical Vapour Deposition
PMMA	Poly-Methyl-MethAcrylate
PVD	Physical Vapour Deposition
QHE	Quantum Hall Effect
Q_{inv}	Total inversion charge, [C]
R	Resistance, [Ω]
ρ	Charge density, [$C\ cm^{-3}$]
RGS	Relative Green Shift

RT	Room Temperature
σ	Conductivity [S]
SEM	Scanning Electron Microscope
SG	Suspended Graphene
Si	Silicon
Si/SiO ₂	300 nm Silicon Dioxide over a Silicon substrate
SiC	Silicon carbide
SiO ₂	Silicon dioxide
SWNT	Single Wall Nanotubes
T	Temperature, [°C]
T _c	Critical Temperature, [°C]
TEM	Transmission Electron Microscopy
TO	Transversal Optical
UHV	Ultra-High Vacuum, [Torr ⁻¹]
UV	Ultraviolet
V _D	Drain Voltage, [V]
V _{Dsat}	Saturation Drain Voltage, [V]
v_F	Fermi velocity, [m s ⁻¹]
V _G	Gate Voltage, [V]
V _S	Source voltage, [V]
V _{sub}	Substrate Voltage, [V]
V _{TH}	Threshold Voltage, [V]
w	Width, [μm]
x _{acc}	Accumulation depth, [μm]
x _d	Depletion depth, [μm]
φ	Flux quantum
Φ	Electric potential
Φ _s	Surface potential

References

- [1] “The Nobel Prize in Physics 2010 - Press Release,” Nobelprize.org, 05 10 2010. [Online]. Available: https://www.nobelprize.org/nobel_prizes/physics/laureates/2010/press.pdf. [Accessed 24 10 2017].
- [2] Class for Physics of the Royal Swedish Academy of Sciences, “Scientific Background on the Nobel Prize in Physics 2010 - Graphene,” The Royal Swedish Academy of Sciences, 5 10 2010. [Online]. Available: https://www.nobelprize.org/nobel_prizes/physics/laureates/2010/advanced-physicsprize2010.pdf. [Accessed 24 10 2017].
- [3] K. Novoselov, A. Geim, S. Morozov, D. Jiang, Y. Zhang, S. Dubonos, I. Grigorieva and A. Firsov, “Electric Field Effect in Atomically Thin Carbon Films,” *Science*, vol. 306, no. 5696, pp. 666-669, 22 10 2004.
- [4] “This Month in Physics History, October 22, 2004: Discovery of Graphene,” *APS News*, p. 2, 10 2009.
- [5] “It's still all about graphene,” *Nature Materials*, vol. 10, no. 1, p. 1, 01 2011.
- [6] A. Geim, “Graphene: Status and Prospects,” *Science*, vol. 324, pp. 1530-1534, 19 06 2009.
- [7] V. Singh, D. Joung, L. Zhai, Das S., S. Khondaker and Seal, “Graphene based materials: Past, present and future,” *Progress in Materials Science*, no. 56, pp. 1178-1271, 2011.
- [8] A. Castro Neto, F. Guinea, N. Peres, K. Novoselov and A. Geim, “The electronic properties of graphene,” *Reviews of Modern Physics*, vol. 81, pp. 109-162, 2009.
- [9] M. Goerbig and G. Montambaux, “Dirac Fermions in Condensed Matter and Beyond,” *Matière de Dirac, Séminaire Poincaré XVIII (Paris)*, pp. 23-49, 2014.
- [10] K. Bolotin, K. Sikes, Z. Jiang, M. Klima, G. Fudenberg, J. Hone, P. Kim and H. Stormer, “Ultrahigh electron mobility in suspended graphene,” *Solid State Communications*, vol. 146, pp. 351-355, 2008.
- [11] X. Du, I. Skatchko, A. Barker and E. Andrei, “Approaching ballistic transport in suspended graphene,” *Nature Nanotechnology*, vol. 3, pp. 491-495, 2008.
- [12] H. Goto, E. Uesugi, R. Eguchi and Y. Kubozono, “Parity Effects in Few-Layer Graphene,” *Nano Letters*, no. 13, pp. 5153-5158, 2013.
- [13] D. Thong, “The Quantum Hall effect - TIFR Infosys Lectures,” 20 09 2016. [Online]. Available: <https://arxiv.org/abs/1606.06687v2>. [Accessed 23 10 2017].
- [14] A. Di Bernardo, O. Millo, M. Barbone, H. Alpern, Y. Kalcheim, U. Sassi, A. Ott, D. De Fazio, D. Yoon, M. Amado, A. Ferrari, J. Linder and J. Robinson, “p-wave triggered superconductivity in single-layer graphene on an electron-doped oxide superconductor,” *Nature Communications*, vol. 8, no. 14024, 2017.
- [15] H. Kroto and D. Walton, “Fullerene,” Encyclopædia Britannica, inc., 09 06 2017. [Online]. Available: <https://www.britannica.com/science/fullerene>. [Accessed 24 10 2017].
- [16] G. Ren, “Carbon Nanotube,” Encyclopædia Britannica, 19 01 2017. [Online]. Available: <https://www.britannica.com/science/carbon-nanotube>. [Accessed 24 10 2017].

- [17] A. Geim and K. Novoselov, "The Rise of Graphene," *Nature Materials*, vol. 6, no. 3, pp. 183-191, 7 03 2007.
- [18] Y. Ohashi, T. Koizumi, T. Yoshikawa, Hironaka T. and K. Shiiki, "Size Effect in the In-plane Electrical Resistivity of Very Thin Graphite Crystals," *Tanso*, no. 180, pp. 235-238, 1997.
- [19] P. Kim, "Graphene and Relativistic Quantum Physics," *Matière de Dirac, Séminaire Poincaré XVIII (Paris)*, pp. 1-21, 2014.
- [20] E. McCann, "Electronic properties of monolayer and bilayer graphene," in *Graphene Nanoelectronics: Metrology, Synthesis, Properties and Applications*, Springer, Berlin, Heidelberg, 2011, pp. 235-275.
- [21] J. McChesney, A. Bostwick, T. Ohta, T. Seyller, K. Horn, J. Gonzalez and E. Rotenberg, "Extended van Hove Singularity and Superconducting Instability in Doped Graphene," *Physical Review Letters*, vol. 104, no. 136803, 2010.
- [22] A. C. Ferrari, F. Bonaccorso, V. Fal'ko, K. Novoselov, S. Roche, P. Boggild, S. Borini, F. Koppens, V. Palermo and N. Pugno, "Science and technology roadmap for graphene, related two-dimensional crystals, and hybrid systems," *Nanoscale*, vol. 7, pp. 4598-4810, 2015.
- [23] L. Chen and S. Kumar, "Thermal Transport in Graphene Supported on Copper," *Journal of Applied Physics*, vol. 112, no. 043502, 2012.
- [24] W. Cai, A. Moore, Y. Zhu, X. Li, S. Chen, L. Shi and R. Ruoff, "Thermal Transport in Suspended and Supported Monolayer Graphene Grown by Chemical Vapor Deposition," *Nano Letters*, vol. 10, pp. 1645-1651, 2010.
- [25] S. Ghosh, W. Bao, D. Nika, S. Subrina, E. Pokatilov, C. Lau and A. Balandin, "Dimensional Crossover of Thermal Transport in Few-Layer Graphene," *Nature Materials*, vol. 9, pp. 555-558, 2010.
- [26] N. Tombros, A. Veligura, J. Junesch, J. van der Berg, P. Zomer, M. Wojtaszek, I. Vera Marun, H. Jonkman and B. van Wees, "Large yield production of high mobility freely suspended graphene electronic devices on a polydimethylglutarimide based organic polymer," *Journal of applied physics*, vol. 109, no. 093702, 2011.
- [27] K. Novoselov, A. Geim, S. Morozov, D. Jiang, M. Katsnelson, I. Grigorieva, S. Dubonos and A. Firsov, "Two-dimensional gas of massless Dirac fermions in graphene," *Nature*, vol. 438, pp. 197-200, 10 11 2005.
- [28] L. Ju, Z. Shi, N. Nair, Y. Lv, C. Jin, J. J. Velasco, C. Ojeda-Aristizabal, H. Bechtel, M. Martin, A. Settl, J. Analytis and F. Wang, "Topological Valley Transport at Bilayer Graphene Domain Walls," *Nature*, vol. 520, pp. 650-655, 2015.
- [29] J. Li, K. Wang, K. McFaul, Z. Zern, Y. Ren, K. Watanabe, T. Taniguchi, Z. Qiao and J. Zhu, "Gate-controlled Topological Conducting Channels in Bilayer Graphene," *Nature Nanotechnology*, vol. 11, pp. 1060-1065, 2016.
- [30] H. Goto, E. Uesugi, R. Eguchi, A. Fujiwara and Y. Kubozono, "Edge-Dependent Transport Properties in Graphene," *Nano Letters*, vol. 13, pp. 1126-1130, 2013.
- [31] Y. Zhang, Y.-W. Tan, H. Stormer and P. Kim, "Experimental Observation of Quantum Hall Effect and Berry's Phase in Graphene," *Nature*, vol. 438, pp. 201-204, 2005.

- [32] K. Novoselov, E. McCann, S. Morozov, V. Fal'ko, M. Katsnelson, U. Zeitler, D. Jiang, F. Schedin and A. Geim, "Unconventional quantum Hall effect and Berry's phase of 2π in bilayer graphene," *Nature Physics*, vol. 2, pp. 177-180, 2006.
- [33] A. Ferrari and D. Basko, "Raman spectroscopy as a versatile tool for studying the properties of graphene," *Nature Nanotechnology*, vol. 8, pp. 235-246, 2013.
- [34] A. Ferrari, J. Meyer, V. Scardaci, C. Casiraghi, M. Lazzeri, F. Mauri, S. Piscanec, D. Jiang, K. Novoselov, S. Roth and A. Geim, "Raman Spectrum of Graphene and Graphene Layers," *Physical Review Letters*, vol. 97, no. 18, pp. 187401-4, 2006.
- [35] I. Childres, L. Jauregui, W. Park, Cao H. and Y. Chen, "Raman Spectroscopy of Graphene and Related Materials," in *New Developments in Photon and Materials Research*, Binghamton, NY, USA, Nova Science Publishers, Incorporated, 2013.
- [36] J. Park, A. Reina, R. Saito, J. Kong, G. Dresselhaus and M. Dresselhaus, "G' band Raman spectra of single, double and triple layer graphene," *Carbon*, vol. 47, pp. 1303-1310, 2009.
- [37] S. Ulonska, "Raman Spectroscopy of graphene," Visuals of a lecture at Free University of Berlin, 14 01 2014. [Online]. Available: http://www.physik.fu-berlin.de/einrichtungen/ag/ag-reich/lehre/ws2013_plasm_nanostructres/06-SERS.pdf. [Accessed 14 11 2017].
- [38] M. Bhuyan, M. Uddin, M. Islam and e. al, "Synthesis of graphene," *International Nano Letters*, vol. 6, pp. 65-83, 2016.
- [39] F. Bonaccorso, A. Lombardo, T. Hasan, Z. Sun, L. Colombo and A. Ferrari, "Production and Processing of Graphene and 2D Crystals," *Materials Today*, vol. 15, no. 12, pp. 564-589, 2012.
- [40] Q. Zheng and J.-K. Kim, "Synthesis, Structure and Properties of Graphene and Graphene Oxide," in *Graphene for Transparent Conductors. Synthesis, Properties and Applications*, Springer, 2015, pp. 29-38.
- [41] M. Fernández-Merino, L. Guardia, J. Paredes, S. Villar-Rodil, P. Solís-Fernández, A. Martínez-Alonso and J. Tascón, "Vitamin C Is an Ideal Substitute for Hydrazine in the Reduction of Graphene Oxide Suspensions," *Journal of Physical Chemistry C*, vol. 114, pp. 6426-6432, 2010.
- [42] J. Nam, D.-C. Kim, H. Yun, D. Shin, S. Nam, W. Lee, J. Hwang, S. Lee, H. Weman and K. Kim, "Chemical Vapor Deposition of Graphene on Platinum: Growth and Substrate Interaction," *Carbon*, vol. 111, pp. 733-740, 2017.
- [43] Y. Gao, T. Cao, F. Cellini, C. Berger, W. de Heer, E. Tosatti, E. Riedo and A. Bongiorno, "Ultrahard Carbon Film from Epitaxial Two-Layer Graphene," *Nature Nanotechnology*, vol. 13, pp. 133-138, 2018.
- [44] The Editors of Encyclopaedia Britannica, "Moore's law," 21 07 2011. [Online]. Available: <https://www.britannica.com/topic/Moores-law>. [Accessed 20 10 2017].
- [45] KTH Royal Institute of Technology, "Moore's Law," [Online]. Available: <https://www.kth.se/social/upload/507d1d3af276540519000002/Moore%E2%80%99s%20law.pdf>. [Accessed 20 10 2017].
- [46] "Feature - Keeping up with Moore's Law," 3 10 2007. [Online]. Available: <http://archive.isgtw.org/images/mooreslaw.jpg>. [Accessed 1 11 2017].

- [47] J. Colinge and C. A. Colinge, "The MOS transistor," in *Physics of Semiconductor devices*, Kluwer Academic Publishers, 2000, pp. 165-235.
- [48] J. Lilienfeld, "Method and Apparatus for Controlling Electric Currents". United States Patent US1745175, 28 1 1930.
- [49] J. Lilienfeld, "Device for controlling Electrical Current". United States Patent US1900018, 7 03 1933.
- [50] "1926: Field Effect Semiconductor Device Concepts Patented," Computer History Museum, [Online]. Available: <http://www.computerhistory.org/siliconengine/field-effect-semiconductor-device-concepts-patented/>. [Accessed 20 10 2017].
- [51] L. Lukasiak and A. Jakubowski, "History of Semiconductors," *Journal of Telecommunication and Information Technology*, 01 2010.
- [52] J. Colinge and C. A. Colinge, "JFET and MESFET," in *Physics of Semiconductor Devices*, Kluwer Academic Publishers, 2000, pp. 153-165.
- [53] "1960: Metal Oxide Semiconductor (MOS) Transistor Demonstrated," Computer History Museum, [Online]. Available: <http://www.computerhistory.org/siliconengine/metal-oxide-semiconductor-mos-transistor-demonstrated/>. [Accessed 20 10 2017].
- [54] W. Shockley and G. Pearson, "Modulation of Conductance of Thin Films of Semiconductors by Surface Charges," *Physical Reviews*, vol. 74, pp. 232-233, 1948.
- [55] D. Kahng, "Silicon-Silicon Dioxide Surface Device," 1960, Technical memorandum of the Bell Laboratories reprinted in Sze, S.M. "Semiconductor Devices: Pioneering Papers", Singapore: World Scientific Publishing Co. Pte. Ltd. 1991, pp. 583-596.
- [56] D. Kahng, "A Historical perspective on the Development of MOS Transistors and Related Devices," *IEEE Transactions on Electron Devices*, vol. 23, no. 7, pp. 655-657, 1976.
- [57] D. Khang, "Electric Field controlled semiconductor device". United States Patent US3102230, 27 08 1963.
- [58] D. J. Walkey, "Physical Electronics Lecture 21: MOSFET Operation," Slides of a lecture at Carleton University, Canada. [Online]. Available: www.doe.carleton.ca/~tjs/21-mosfetop.pdf. [Accessed 27 11 2017].
- [59] T. Ytterdal, Y. Cheng and T. Fjeldly, "MOSFET Device Physics and Operation," in *Device Modeling for Analog and RF CMOS Circuit Design*, John Wiley & Sons, Ltd., 2003, pp. 1-15.
- [60] M. Lafkioti, B. Krauss, T. Lohmann, U. Zschieschang, H. Klauk, K. v. Klitzing and J. Smet, "Graphene on a Hydrophobic Substrate: Doping Reduction and Hysteresis Suppression under Ambient Conditions," *Nano Letters*, vol. 10, pp. 1149-1153, 2010.
- [61] M. Tyona, "A Theoretical Study on Spin Coating Technique," *Advances in Materials Research*, vol. 2, no. 4, pp. 195-208, 2013.
- [62] Y. Huang, E. Sutter, N. Shi, J. Zheng, T. Yang, D. Englung, H.-J. Gao and P. Sutter, "Reliable Exfoliation of Large-Area High-Quality Flakes of Graphene and Other Two-Dimensional Materials," *ACS Nano*, vol. 9, no. 11, pp. 10612-10620, 2015.
- [63] P. Blake, E. Hill, A. Castro Neto, K. Novoselov, D. Jiang, R. Yang, T. Booth and A. Geim, "Making Graphene Visible," *Applied Physics Letters*, vol. 91, no. 063124, 2007.

- [64] J. Oostinga, H. Heersche, X. Liu, A. Morpurgo and L. Vandersypen, "Supplementary information: Gate-induced Insulating State in Bilayer Graphene Devices," *Nature Materials*, vol. 7, pp. 151-157, 2008.
- [65] S. Rahman, A. Hashim and S. Kasai, "Identification of Graphene Layer Number from Color Combination Contrast Image for Wide-Area Characterization," *Japanese Journal of Applied Physics*, vol. 51, no. 06FD09, 2012.
- [66] E. Uesugi, "Study on electronic properties of graphene with electrostatic carrier doping," Master Thesis in Surface Chemistry, Okayama University 2013.
- [67] MicroChem, "Copolymer MMA(8.5)MAA(EL9) Material Safety Data Sheet," 19 04 2012. [Online]. Available: <http://nano.pse.umass.edu/sites/default/files/MMA%208.5%20MSDS.pdf>. [Accessed 22 12 2017].
- [68] "Photoresists," Microchemicals GmbH, [Online]. Available: <http://www.microchemicals.com/products/photoresists.html>. [Accessed 19 10 2017].
- [69] Elionix Inc, *ELS-Series Overlay Exposure (Registration) Instruction Manual. Instruction Training Course Handbook*.
- [70] MicroChem, "NANO™ PMMA and Copolymer," 2001. [Online]. Available: http://microchem.com/pdf/PMMA_Data_Sheet.pdf. [Accessed 22 12 2017].
- [71] The Dow Chemical Company, "Microposit LOL 1000 and 2000 Liftoff Layers," 03 2014. [Online]. Available: http://microchem.com/PDFs_Dow/MICROPOSIT_LOL1000-2000%20Dow.pdf. [Accessed 2 11 2017].
- [72] A. Mayorov, D. Elias, I. Mukhin, S. Morozov, L. Ponomarenko, K. Novoselov, A. Geim and R. Gorbache, "How Close Can One Approach the Dirac Point in Graphene Experimentally?," *Nano Letters*, vol. 12, pp. 4629-4634, 2012.
- [73] Z. Ni, H. Wang, Z. Luo, Y. Wang, T. Yu, Y. Wu and Z. Shen, "The effect of vacuum annealing on graphene," *Journal of Raman Spectroscopy*, vol. 41, pp. 479-483, 2010.
- [74] M. Ishigami, J. Chen, W. Cullen, M. Fuhrer and E. Williams, "Atomic Structure of Graphene on SiO₂," *Nano Letters*, vol. 7, no. 6, pp. 1643-1648, 2007.
- [75] E. Hwang, S. Adam and S. Das Dharma, "Carrier Transport in Two-Dimensional Graphene Layers," *Physical Review Letters*, vol. 98, no. 186806, 2007.
- [76] J.-H. Chen, C. Jang, S. Adam, M. Fuhrer, E. Williams and M. Ishigami, "Charged-Impurity Scattering in Graphene," *Nature Physics*, vol. 4, pp. 377-381, 2008.
- [77] S. Morozov, K. Novoselov, M. Katsnelson, F. Schedin, D. Elias, J. Jaszczak and A. Geim, "Giant Intrinsic Carrier Mobilities in Graphene and Its Bilayer," *Physical Review Letters*, vol. 100, no. 016602, 2008.
- [78] L. Ponomarenko, R. Yang, T. Mohiuddin, M. Katsnelson, K. Novoselov, S. Morozov, A. Zhukov, F. Schedin, E. Hill and A. Geim, "Effect of High-k Environment on Charge Carrier Mobility in Graphene," *Physical Review Letters*, vol. 102, no. 206603, 2009.
- [79] S. Morozov, K. Novoselov, M. Katsnelson, F. Schedin, L. Ponomarenko, D. Jiang and A. Geim, "Strong Suppression of Weak Localization in Graphene," *Physical Review Letters*, vol. 97, no. 016801, 2006.
- [80] V. Dorgan, M.-H. Bae e E. Pop, «Mobility and saturation velocity in graphene on SiO₂,» *Applied Physics Letters*, vol. 97, n. 082112, 2010.

- [81] E. McCann and M. Koshino, "The Electronic Properties of Bilayer Graphene," *Reports on Progress in Physics*, vol. 75, no. 056503, 2013.
- [82] E. McCann, D. Abergel and V. Fal'ko, "Electrons in Bilayer Graphene," *Solid State Communications*, vol. 143, pp. 110-115, 2007.
- [83] J. Ye, M. Craciun, M. Koshino, S. Russo, S. Inoue, H. Yuan, H. Shimotani, A. Morpurgo and Y. Iwasa, "Accessing the Transport Properties of Graphene and Multilayers at High Carrier Density," *Proceedings of the National Academy of Sciences*, vol. 108, no. 32, pp. 13002-13006, 2011.
- [84] R. Nouchi and K. Tanigaki, "Path of the Current Flow at the Metal Contacts of Graphene Field-Effect Transistors with Distorted Transfer Characteristics," *Applied Physics Letters*, vol. 150, no. 033112, 2014.
- [85] B. Huard, N. Stander, J. Sulpizio and D. Goldhaber-Gordon, "Evidence of the Role of Contacts on the Observed Electron-Hole Asymmetry in Graphene," *Physical Review B*, vol. 78, no. 121402(R), 2008.
- [86] K. Hinrichs and K.-J. Eichhorn (eds), "Ellipsometry: A Survey of Concept," in *Ellipsometry of Functional Organic Surfaces and Films*, Springer-Verlag Berlin Heidelberg, 2014.

	LOL			PMMA			Copolymer		
	Baked	Baked + UV	Baked + deep UV	Baked	Baked + EB	Baked + deep UV	Baked	Baked + EB	Baked + deep UV
Acetone	-/+			+	+		+	+	
MIBK	-			-	+		-	+	
O-xylene (RT)				-	+		-		
O-xylene (80 °C)				+	+		-/+		
EL	-	-	+	-		+			+
IPA				-	-		-	-	

Acronyms used:

LOL: polymethylglutarimide
PMMA: polymethyl methacrylate
Copolymer: MMA (8.5) MAA
MIBK: methyl isobutyl ketone
EL: ethyl lactate
IPA: isopropyl alcohol

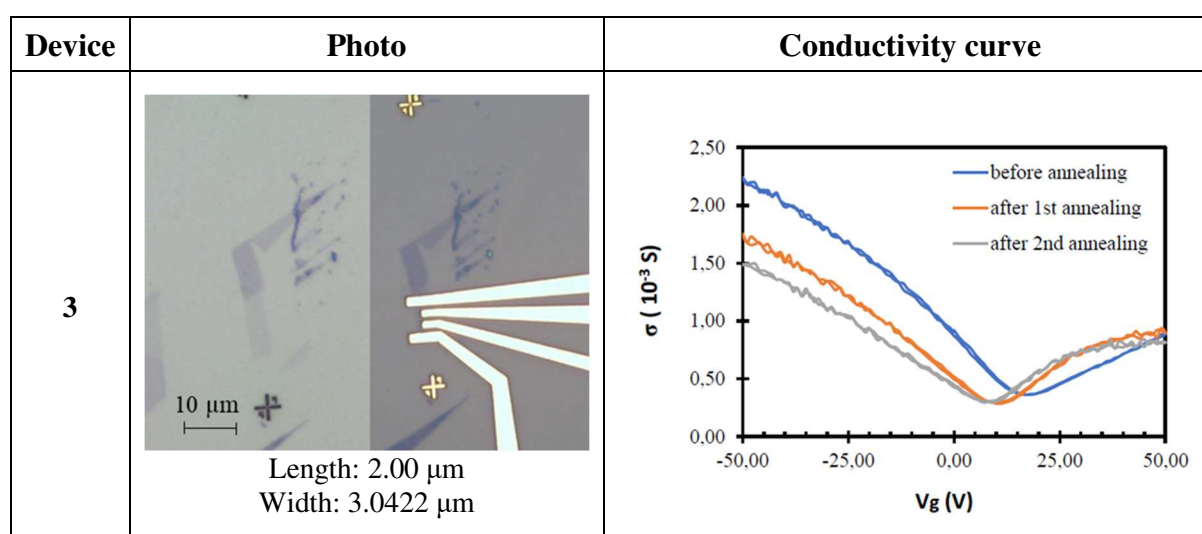
Legend

+: completely soluble
-/+ : partially soluble
- : completely insoluble

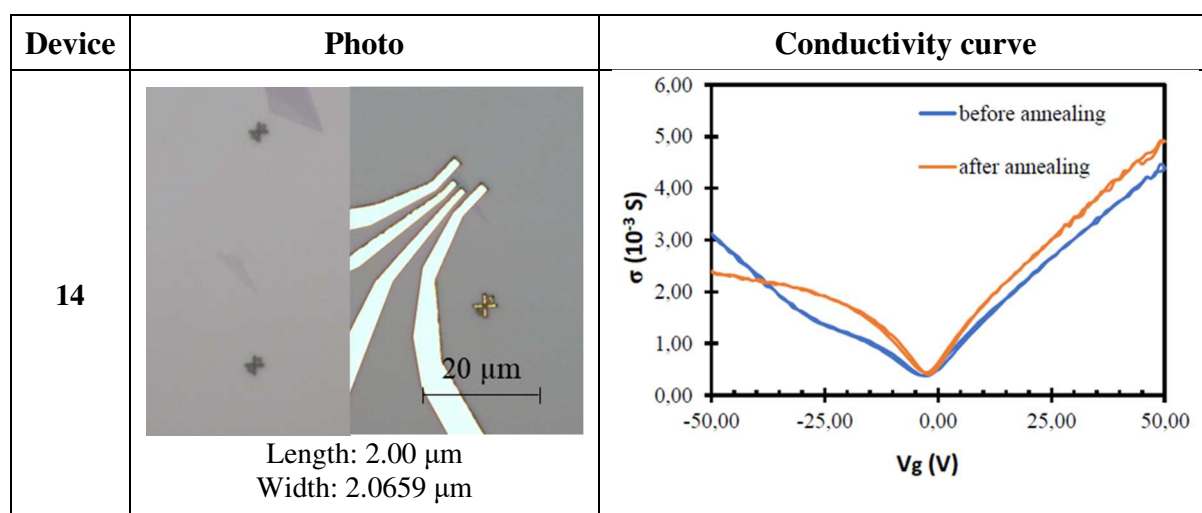
Supporting information 2. Infographic of the mechanically exfoliated NSG devices

In the following supporting information, one can see all the mechanically exfoliated NSG devices whose results were used in this work. A picture of every devices at x1000 is taken after the deposition of the electrodes, an inset of the target before the realization of the electrodes is showed whenever the electrodes do not allow an easy recognition of the target. Besides the photo of the device is shown its conductivity curve.

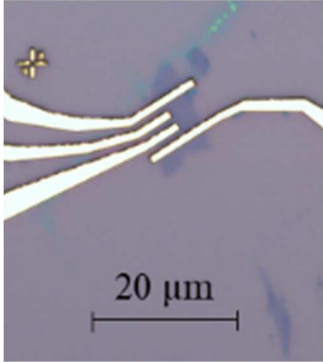
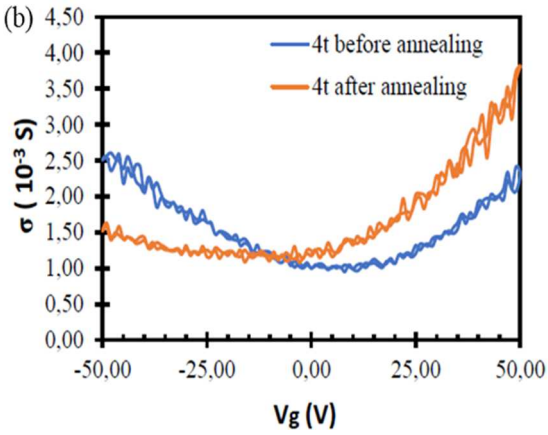
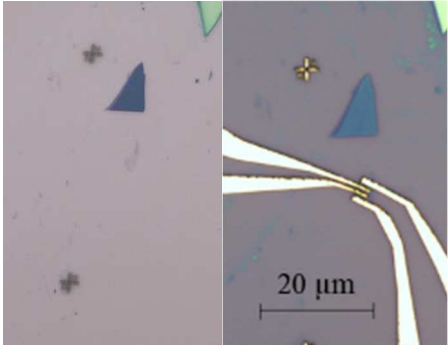
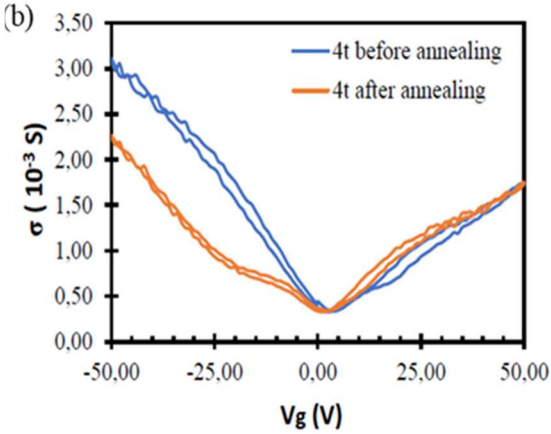
Device realized on sample 3



Devices realized on sample 14



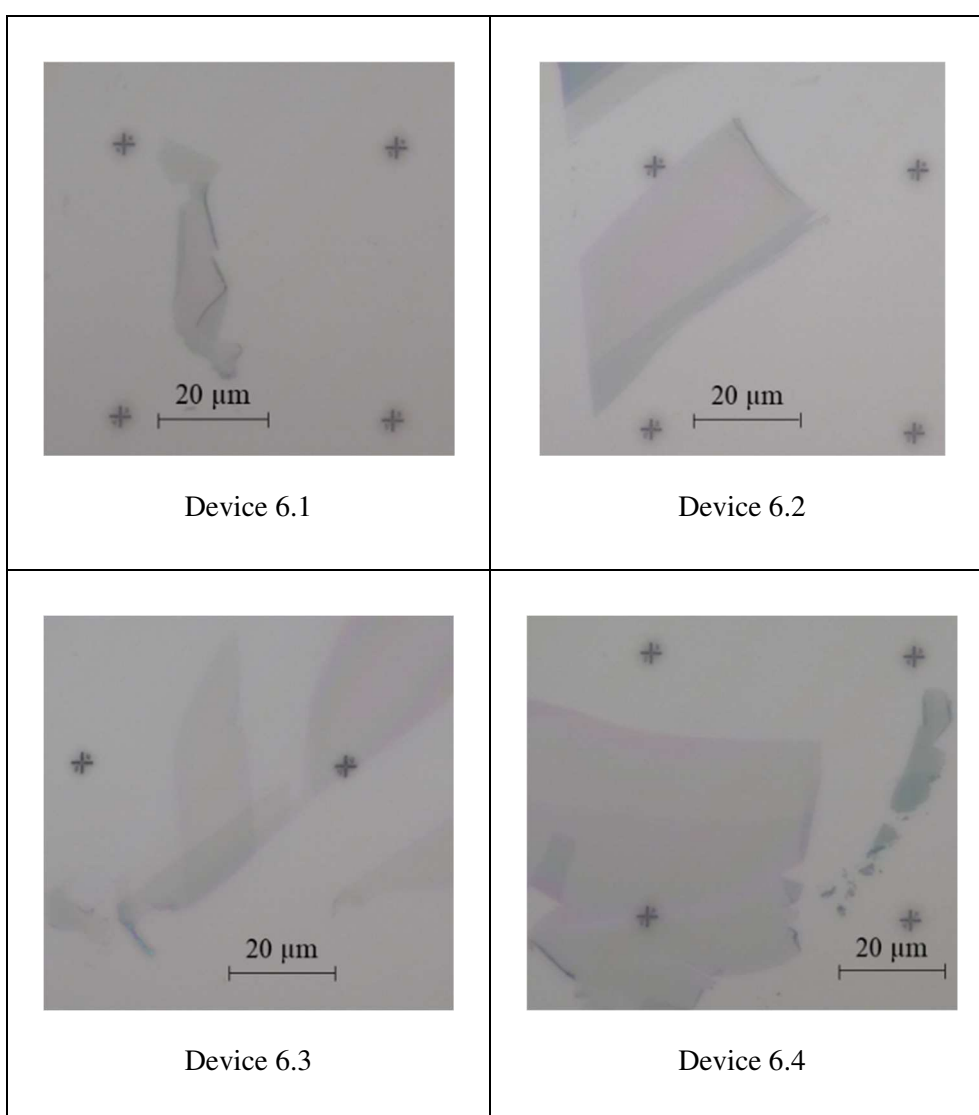
Devices realized on sample 15

Device	Photo	Conductivity curve
15.1	 <p>Length: 2.00 μm Width: 7.1115 μm</p>	
15.2	 <p>Length: 1.00 μm Width: 1.9590 μm</p>	

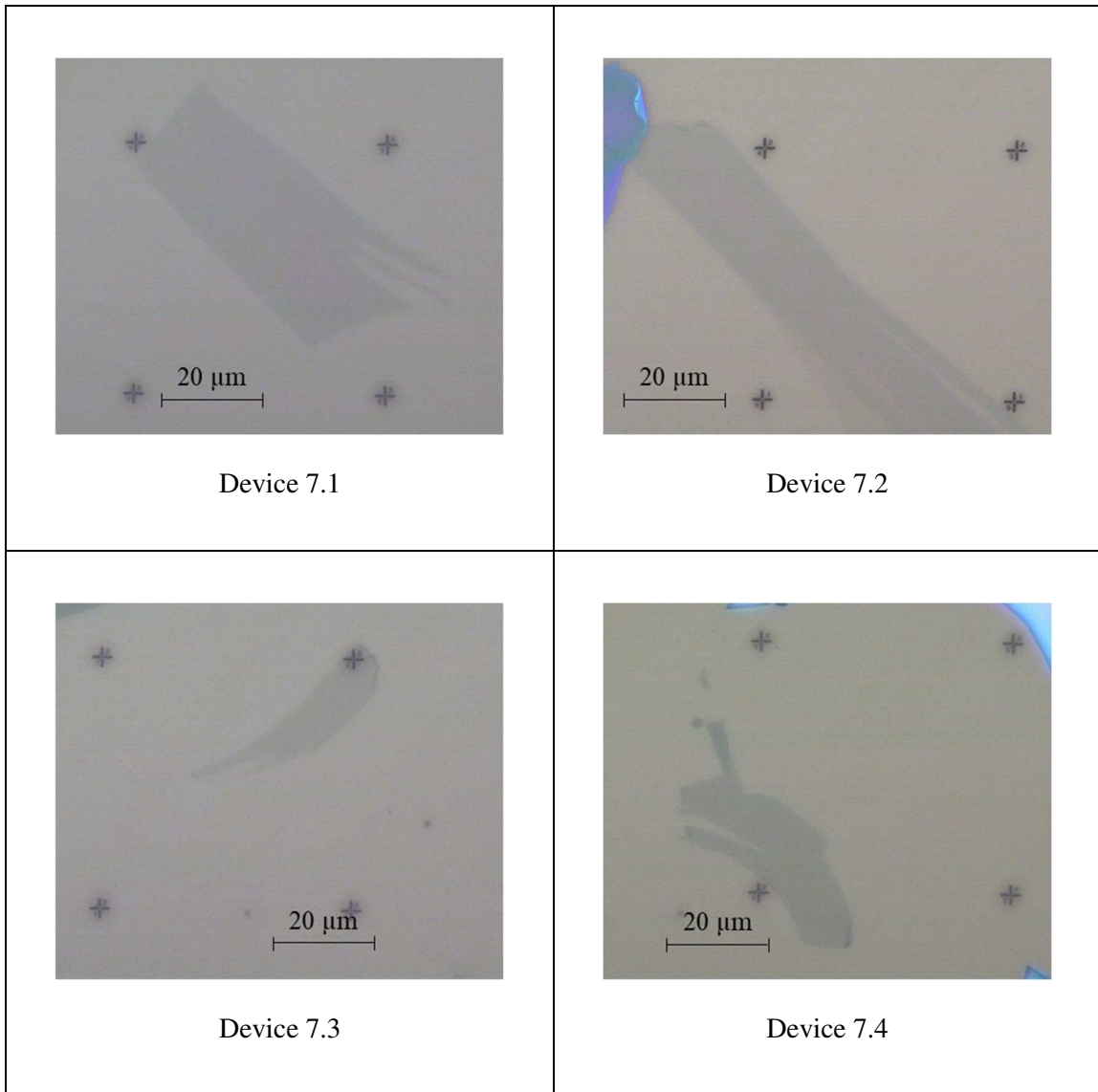
Supporting information 3. Optical microscopy images of the LOL-NSG devices before the realization of the electrodes

The following supporting information contains pictures of each of the LOL-NSG devices before the realization of the electrodes. The pictures were taken at the optical microscope after the etching of the Reg-marks with a magnification of $\times 1000$. Since the identification of the number of layers was not possible to during the OM observation, the criteria with which the samples were chosen was “the thinner the better”.

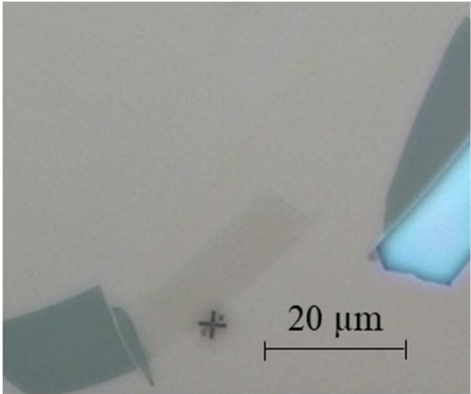
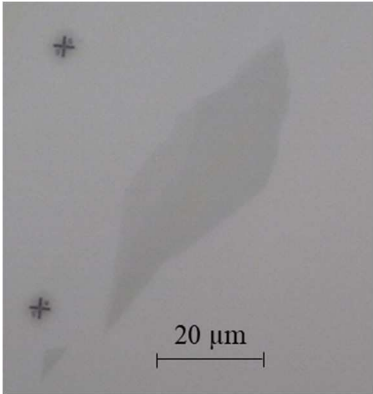
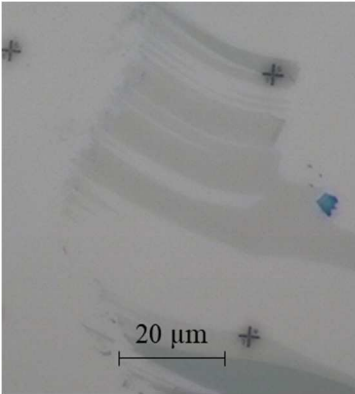
Devices realized on sample 6



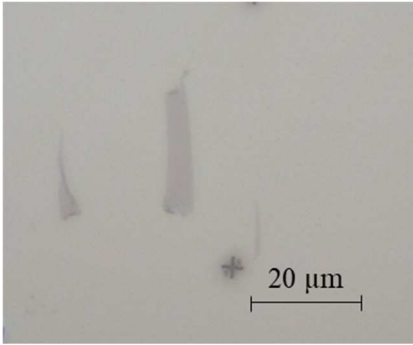
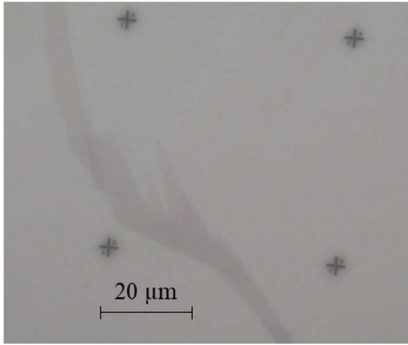
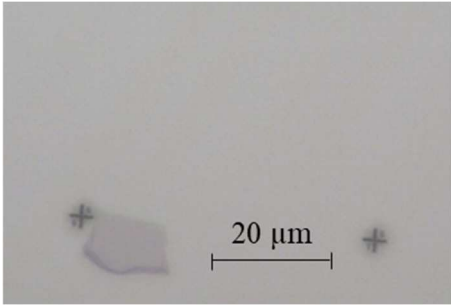
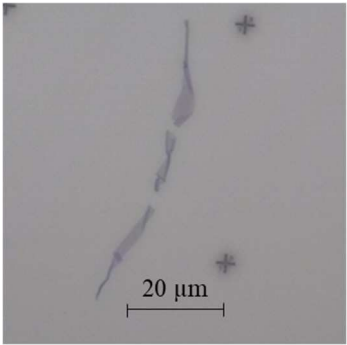
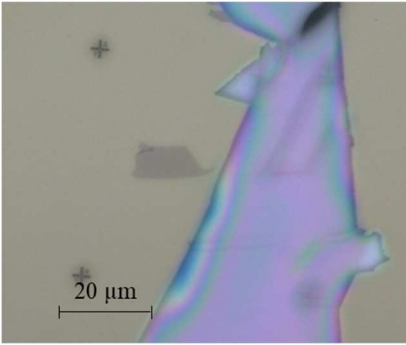
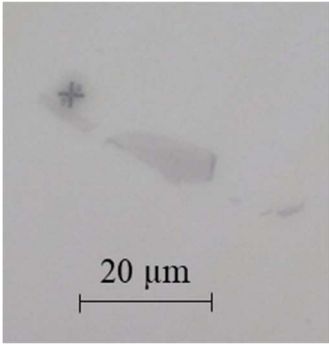
Devices realized on sample 7

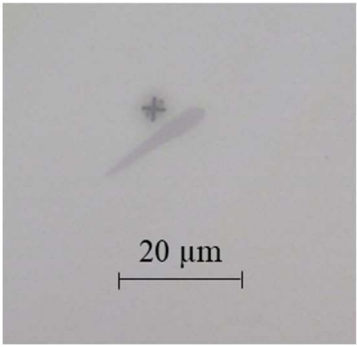
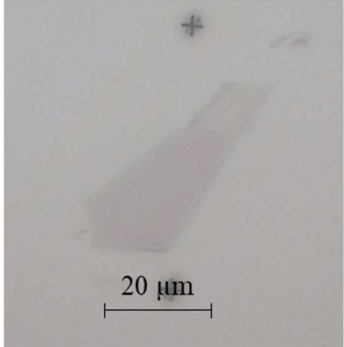
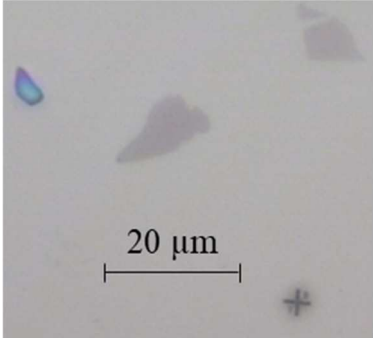


Devices realized on sample 8

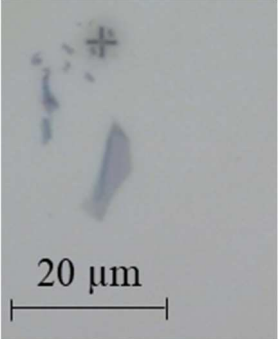
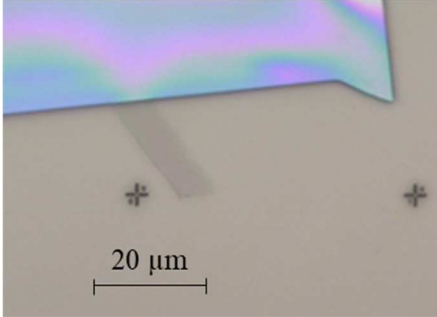
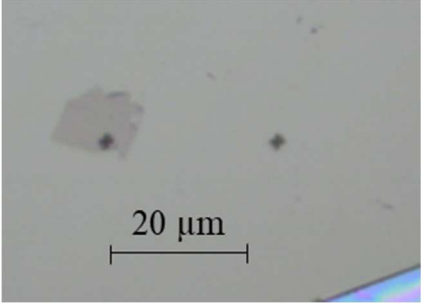
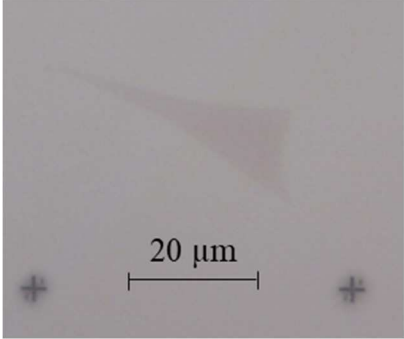
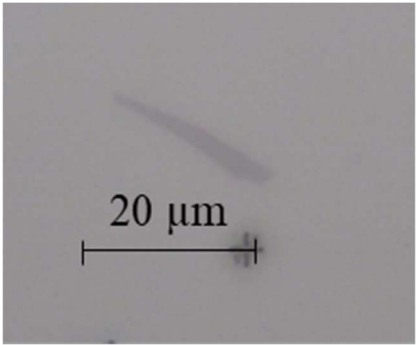
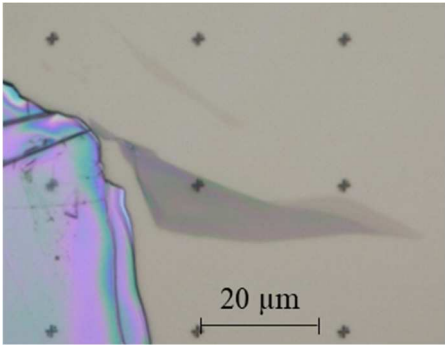
 <p>Micrograph of Device 8.1 showing a device structure with a scale bar of 20 μm. The device features a central rectangular region with a blue-tinted area on the right side. There are two small crosshair markers on the left side of the device.</p>	 <p>Micrograph of Device 8.2 showing a device structure with a scale bar of 20 μm. The device features a central rectangular region with a blue-tinted area on the right side. There are two small crosshair markers on the left side of the device.</p>
 <p>Micrograph of Device 8.3 showing a device structure with a scale bar of 20 μm. The device features a central rectangular region with a blue-tinted area on the right side. There are two small crosshair markers on the left side of the device.</p>	

Devices realized on sample 9

 <p>Micrograph of Device 9.1 showing a thin, elongated structure. A scale bar indicates 20 μm.</p>	 <p>Micrograph of Device 9.3 showing a thin, elongated structure. A scale bar indicates 20 μm.</p>
<p>Device 9.1</p>	<p>Device 9.3</p>
 <p>Micrograph of Device 9.4 showing a thin, elongated structure. A scale bar indicates 20 μm.</p>	 <p>Micrograph of Device 9.5 showing a thin, elongated structure. A scale bar indicates 20 μm.</p>
<p>Device 9.4</p>	<p>Device 9.5</p>
 <p>Micrograph of Device 9.6 showing a thin, elongated structure. A scale bar indicates 20 μm.</p>	 <p>Micrograph of Device 9.7 showing a thin, elongated structure. A scale bar indicates 20 μm.</p>
<p>Device 9.6</p>	<p>Device 9.7</p>

 <p>Micrograph of Device 9.8 showing a small, elongated, light-colored structure. A scale bar indicates 20 μm. A small crosshair is visible in the upper left corner.</p>	 <p>Micrograph of Device 9.9 showing a larger, elongated, light-colored structure. A scale bar indicates 20 μm. A small crosshair is visible in the upper left corner.</p>
 <p>Micrograph of Device 9.10 showing a small, elongated, light-colored structure. A scale bar indicates 20 μm. A small crosshair is visible in the lower right corner.</p>	

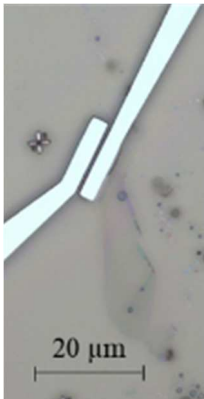
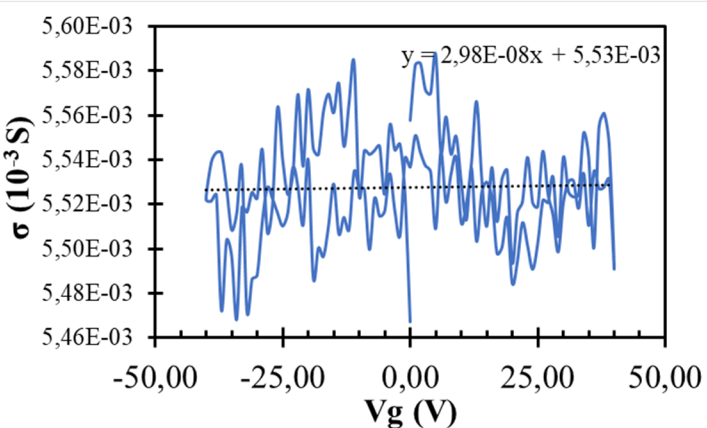

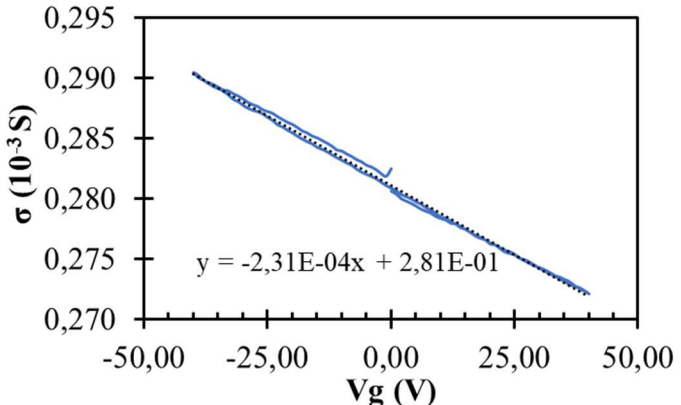
Devices realized on sample 10


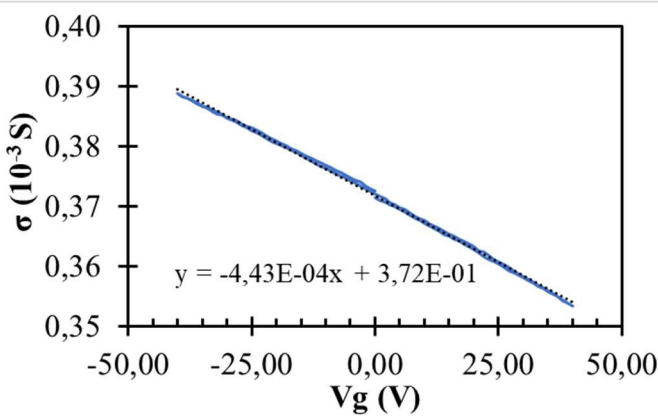
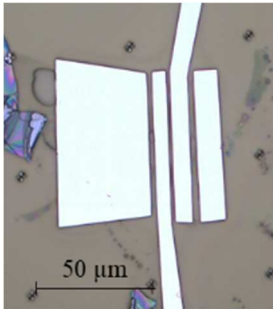
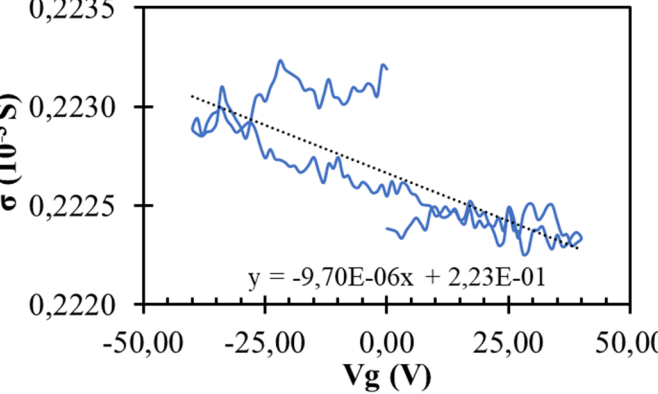
 <p>Micrograph of Device 10.1 showing a small, irregularly shaped device structure on a light gray background. A scale bar at the bottom indicates 20 μm.</p>	 <p>Micrograph of Device 10.2 showing a device structure with a distinct, elongated, and slightly curved shape. A scale bar at the bottom indicates 20 μm.</p>
Device 10.1	Device 10.2
 <p>Micrograph of Device 10.3 showing a small, irregularly shaped device structure on a light gray background. A scale bar at the bottom indicates 20 μm.</p>	 <p>Micrograph of Device 10.3b showing a device structure with a distinct, elongated, and slightly curved shape. A scale bar at the bottom indicates 20 μm.</p>
Device 10.3	Device 10.3b
 <p>Micrograph of Device 10.4 showing a small, irregularly shaped device structure on a light gray background. A scale bar at the bottom indicates 20 μm.</p>	 <p>Micrograph of Device 10.5 showing a device structure with a distinct, elongated, and slightly curved shape. A scale bar at the bottom indicates 20 μm.</p>
Device 10.4	Device 10.5

Supporting information 4. Infographic of the mechanically exfoliated LOL-NSG devices

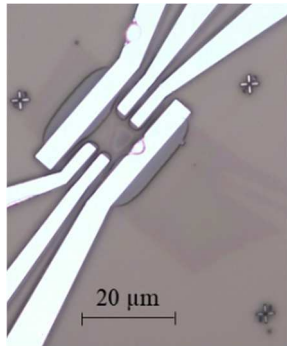
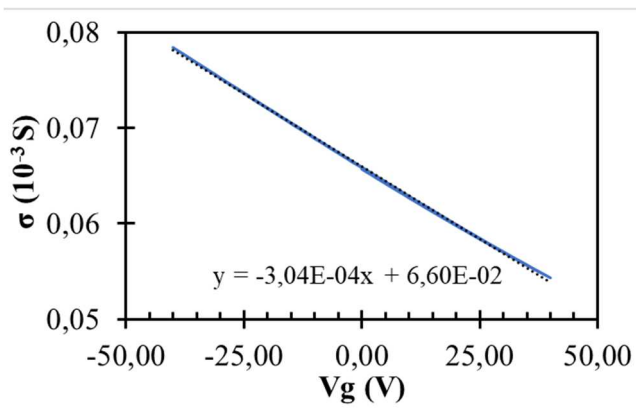
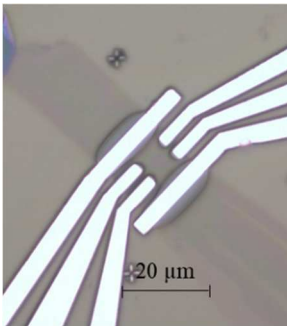
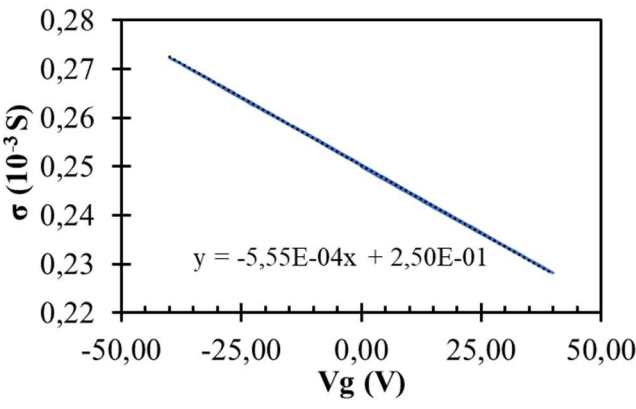
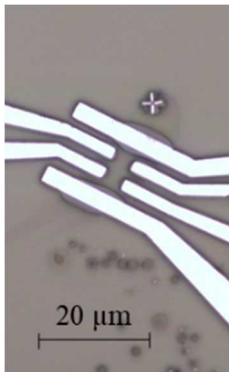
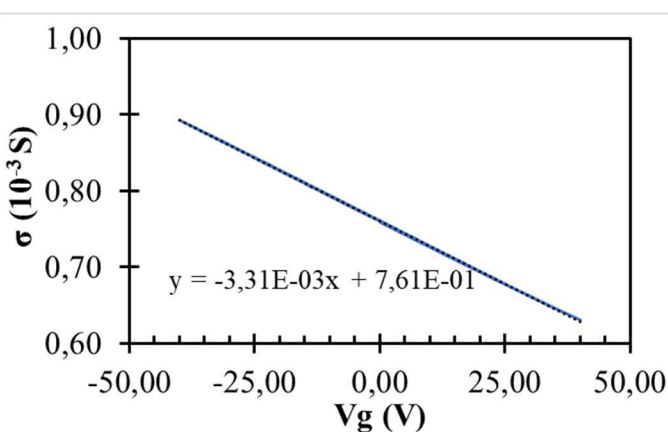
In the following supporting information, one can see all the mechanically exfoliated LOL-NSG devices whose results were used in this work. A picture of every device is taken after the deposition of the electrodes, an inset of the target before the realization of the electrodes is showed whenever the electrodes do not allow an easy recognition of the target. Besides the photo of the device is shown its conductivity curve. All the devices of LOL-NSG were tested with a two-terminal configuration. If not otherwise specified, the length of the channel is to be considered between source and drain. In the case of multiple measurements on a same device, the two electrodes considered are circled in red.

Devices realized on sample 6

Device	Photo	Conductivity curve
6.1	 <p>Length: 0.8846 μm Width: 6.5065 μm</p>	 <p>σ (10^{-3} S)</p> <p>$y = 2,98\text{E-}08x + 5,53\text{E-}03$</p> <p>$V_g$ (V)</p>
6.2	 <p>Length: 1.9948 μm Width: 23.5960 μm</p>	 <p>σ (10^{-3} S)</p> <p>$y = -2,31\text{E-}04x + 2,81\text{E-}01$</p> <p>$V_g$ (V)</p>

<p>6.3</p>	 <p>Length: 1.9208 μm Width: 14.6706 μm</p>	 <p>σ (10^{-3} S)</p> <p>$y = -4,43\text{E-}04x + 3,72\text{E-}01$</p> <p>$V_g$ (V)</p>
<p>6.4</p>	 <p>Length: 1.9374 μm Width: 48.0768 μm</p>	 <p>σ (10^{-3} S)</p> <p>$y = -9,70\text{E-}06x + 2,23\text{E-}01$</p> <p>$V_g$ (V)</p>

Devices realized on sample 7

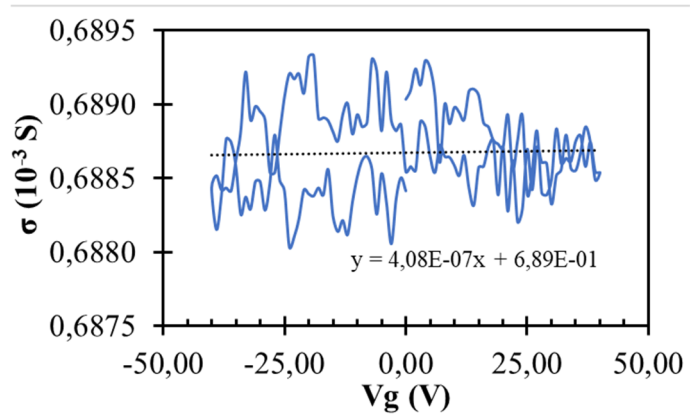
Device	Photo	Conductivity curve
7.1	 <p>Length: 10.5010 μm Width: 23.3282 μm</p>	 <p>$y = -3,04E-04x + 6,60E-02$</p>
7.2	 <p>Length¹: 2.0000 μm Width: 15.7217 μm</p>	 <p>$y = -5,55E-04x + 2,50E-01$</p>
7.3	 <p>Length: 9.7666 μm Width: 9.7805 μm</p>	 <p>$y = -3,31E-03x + 7,61E-01$</p>

¹ The length of the channel is here to be considered between the internal electrodes

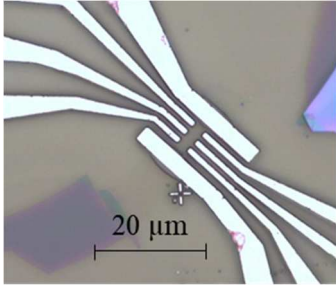
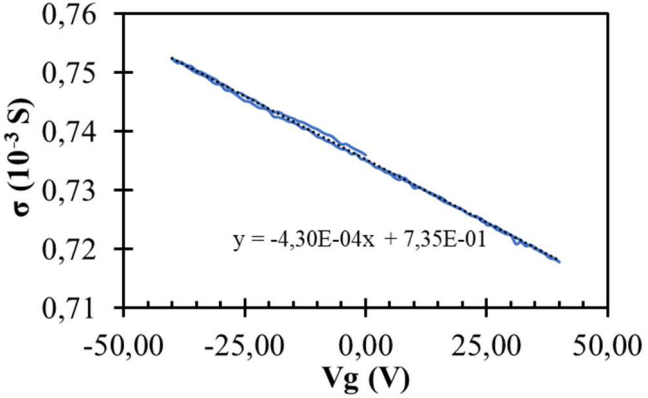
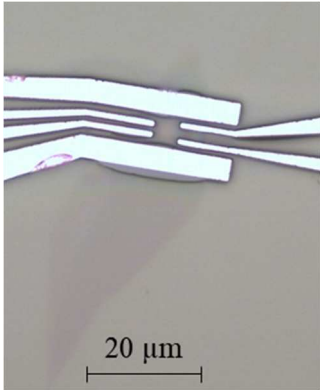
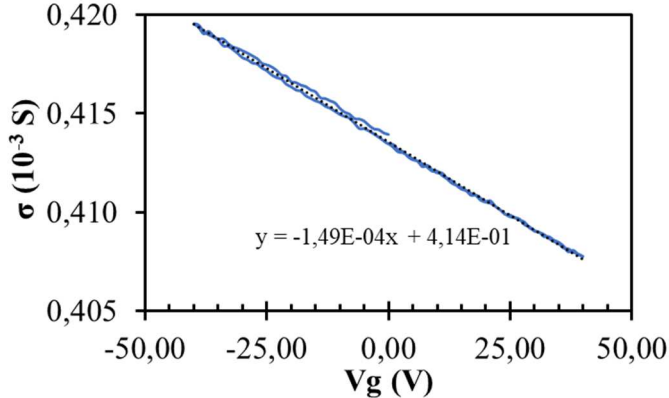
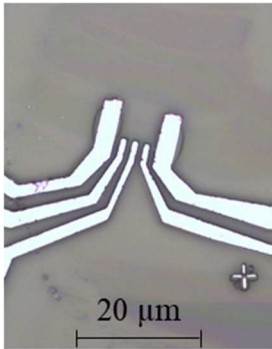
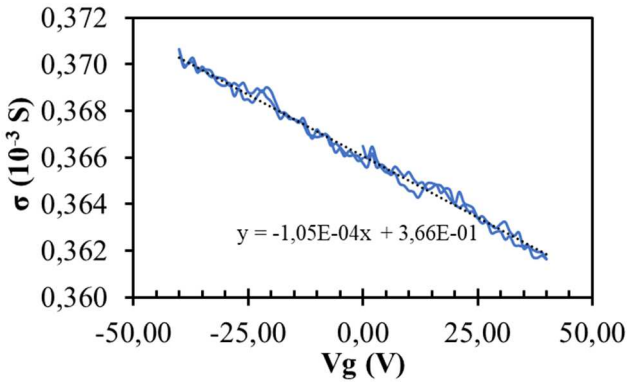
7.4



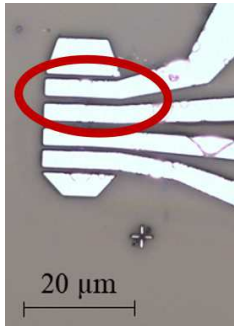
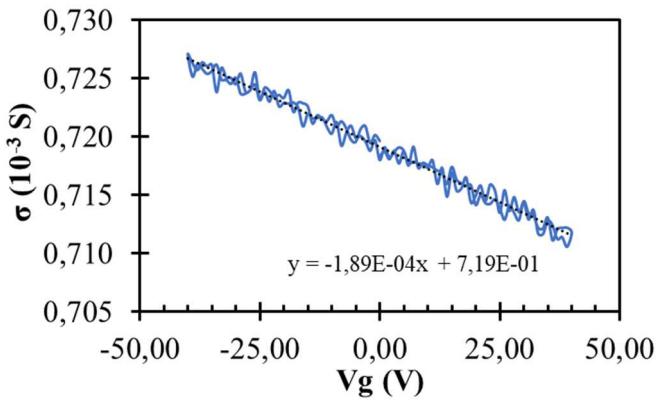
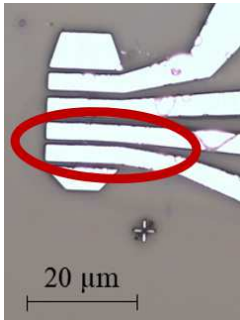
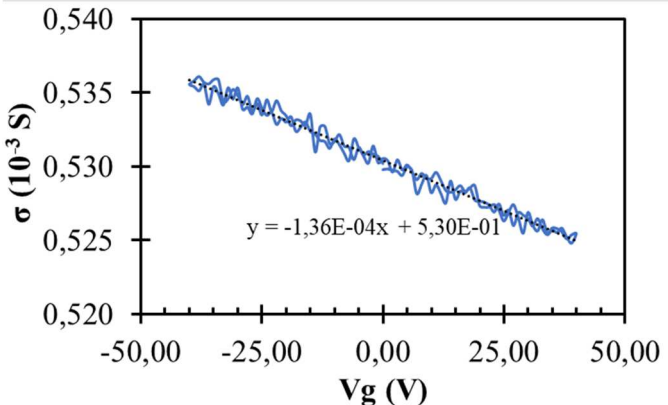
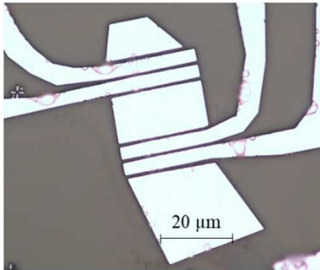
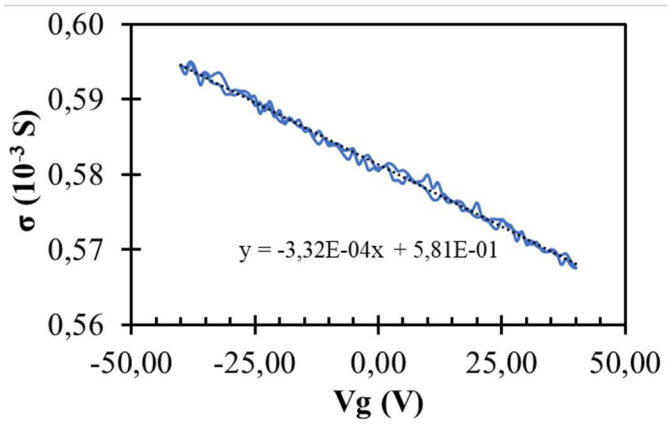
Length: 7.6821 μm
Width: 11.1868 μm


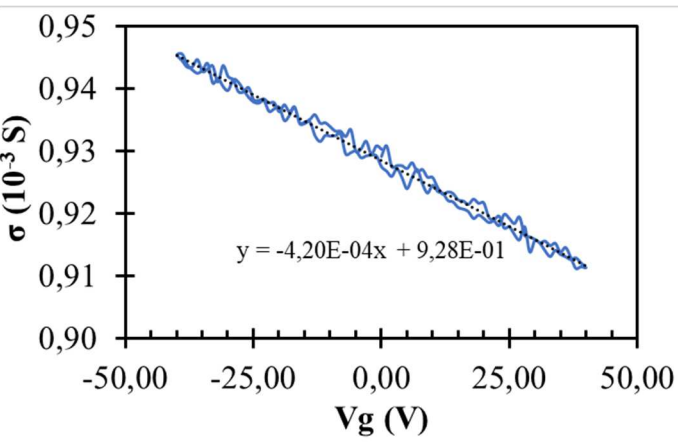
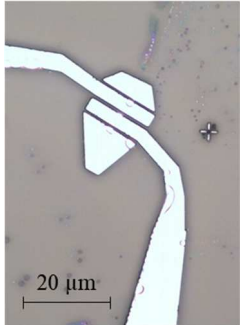
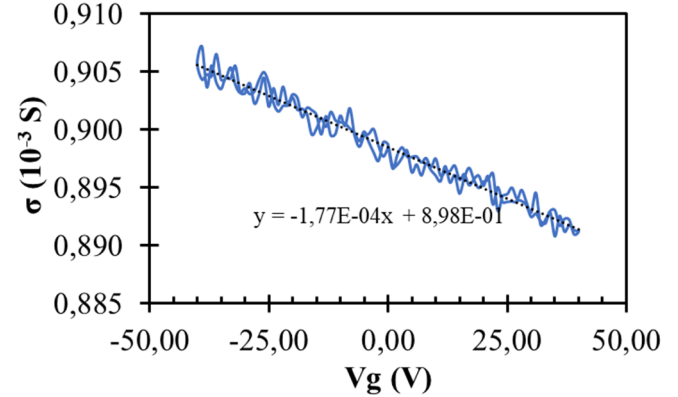
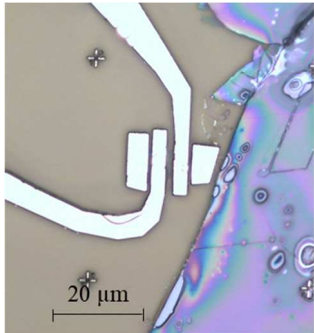
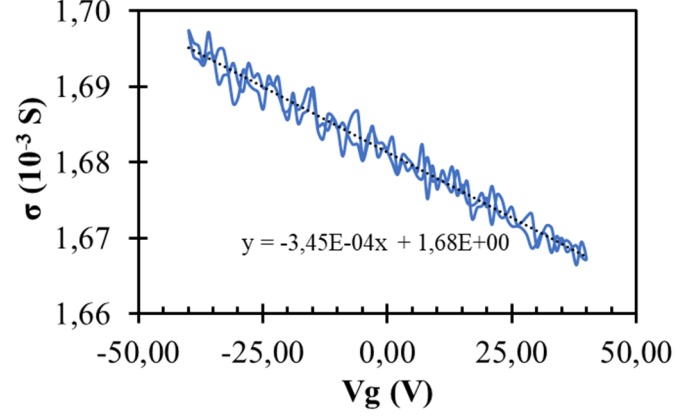
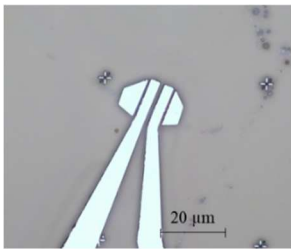
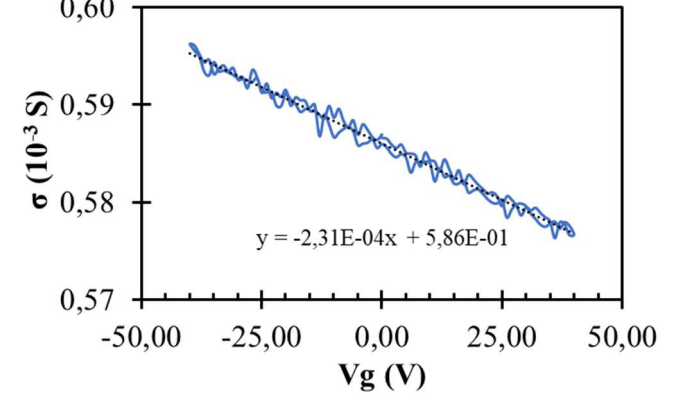


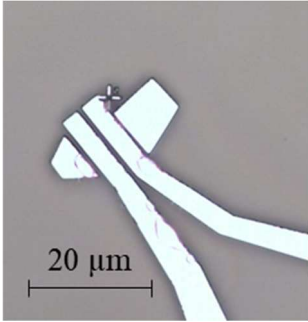
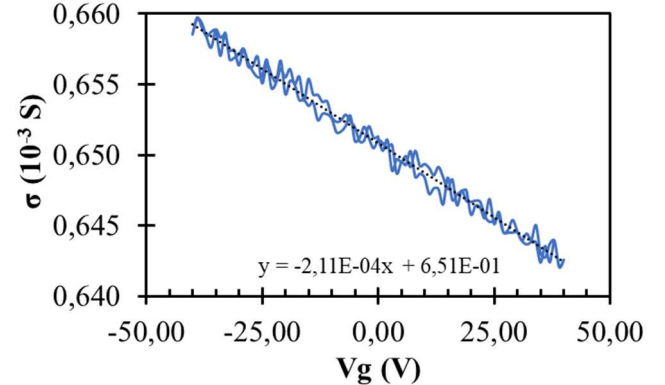
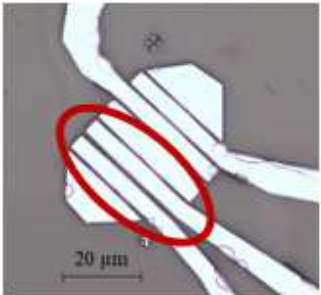
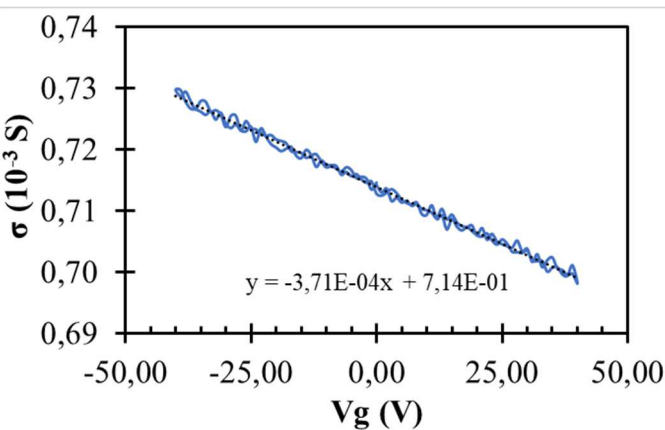
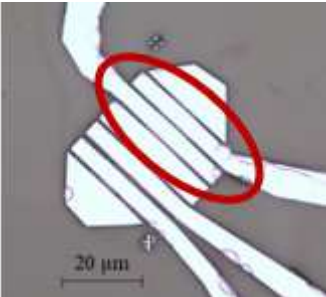
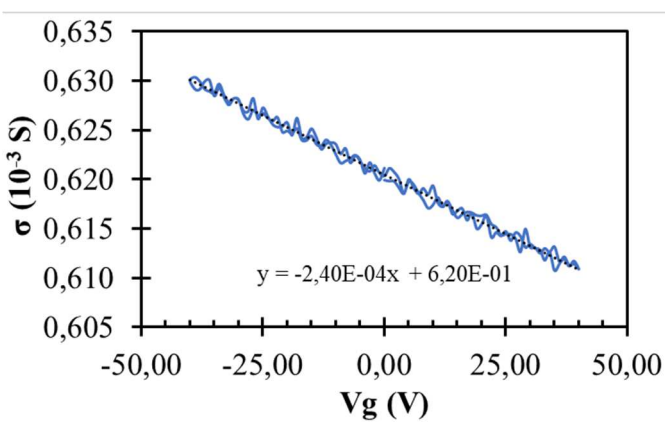
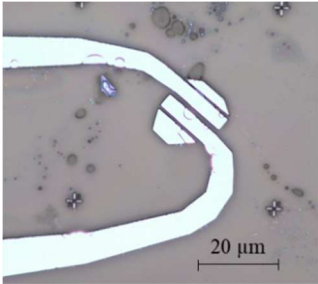
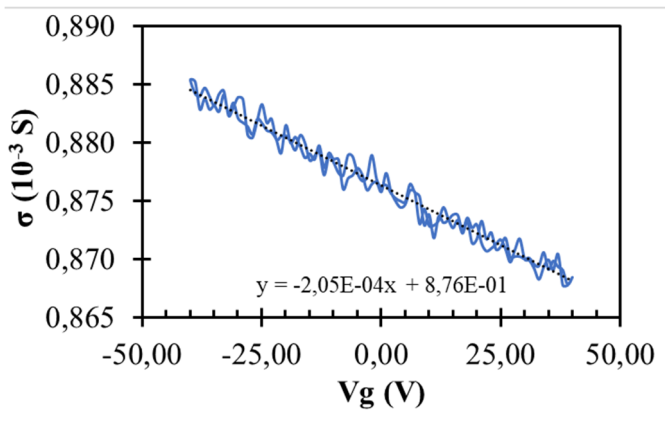
Devices realized on sample 8

Device	Photo	Conductivity curve
8.1	 <p>Length: 7.4120 μm Width: 8.4761 μm</p>	 <p>σ ($10^{-3} S$)</p> <p>$y = -4,30E-04x + 7,35E-01$</p> <p>$V_g$ (V)</p>
8.2	 <p>Length: 6.0000 μm Width: 14.9429 μm</p>	 <p>σ ($10^{-3} S$)</p> <p>$y = -1,49E-04x + 4,14E-01$</p> <p>$V_g$ (V)</p>
8.3	 <p>Length: 7.0555 μm Width: 5.8438 μm</p>	 <p>σ ($10^{-3} S$)</p> <p>$y = -1,05E-04x + 3,66E-01$</p> <p>$V_g$ (V)</p>

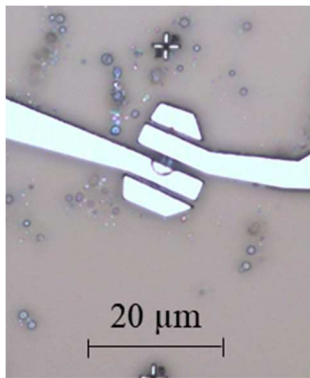
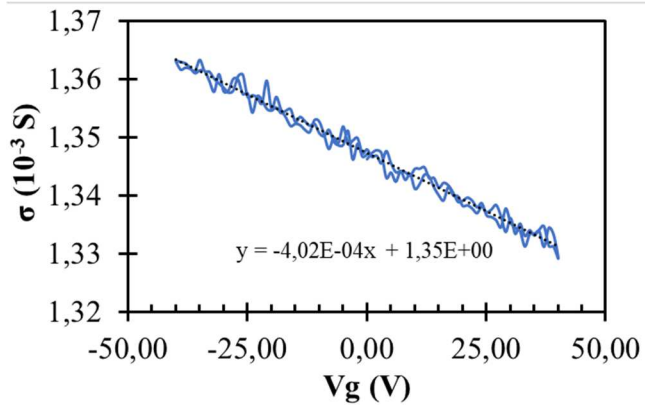
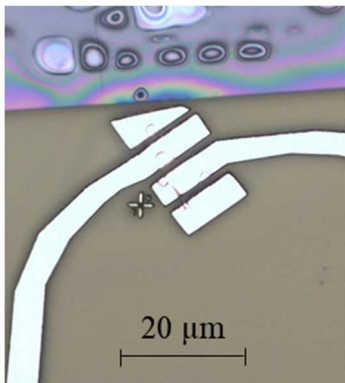
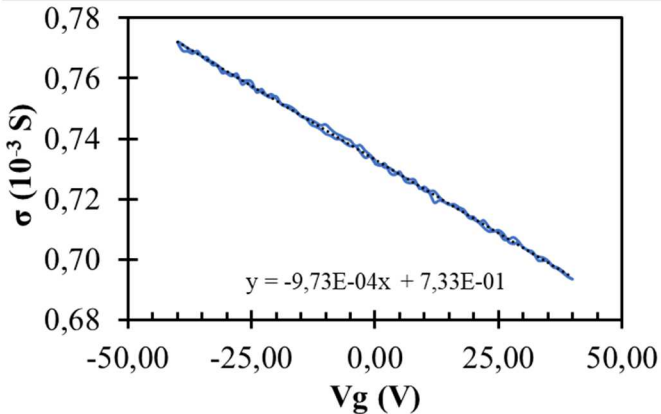
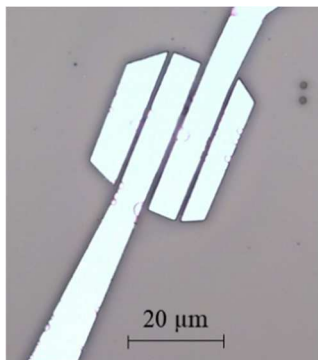
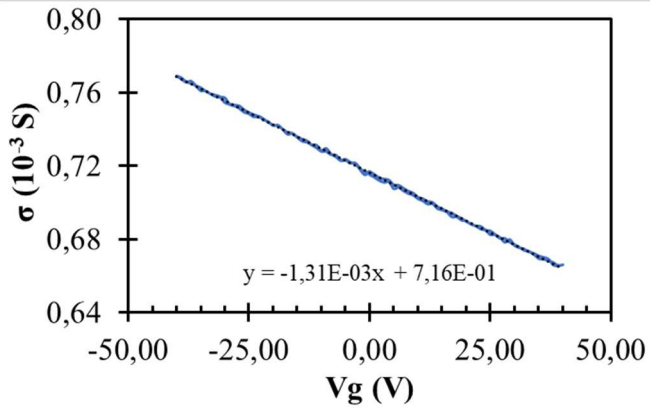
Devices realized on sample 9

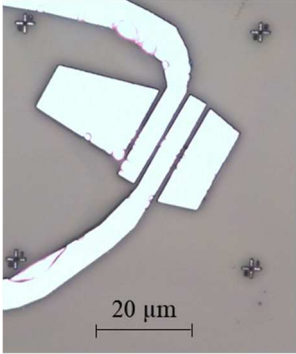
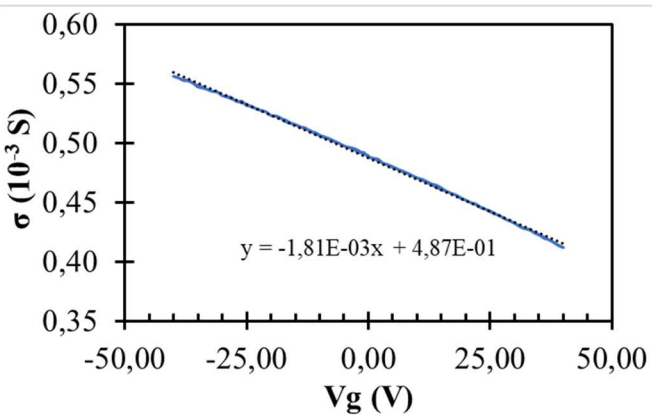
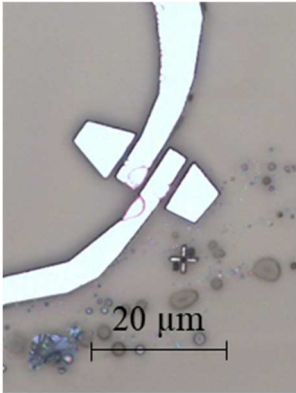
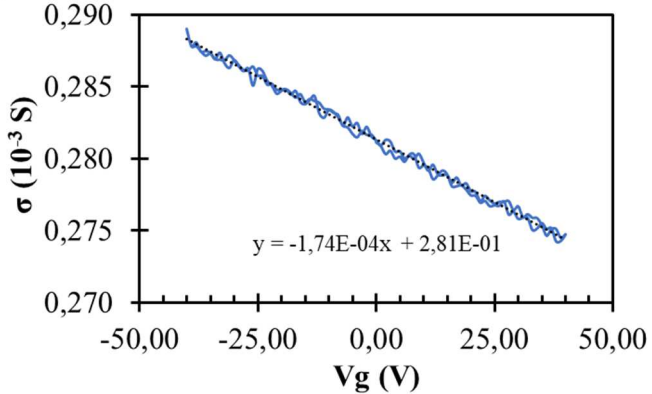
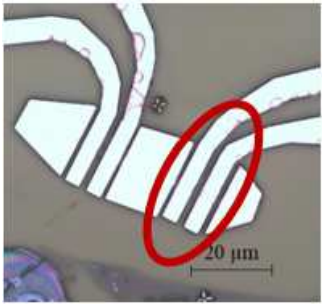
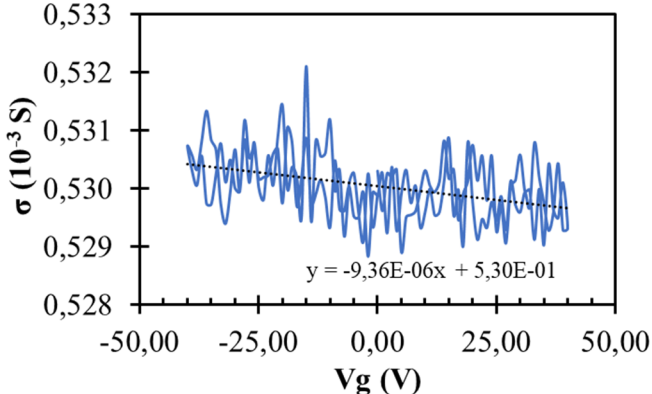
Device	Photo	Conductivity curve
9.1 (1)	 <p>Length: 1.5000 μm Width: 4.3942 μm</p>	 <p>σ (10^{-3} S)</p> <p>$y = -1,89\text{E-}04x + 7,19\text{E-}01$</p> <p>$V_g$ (V)</p>
9.1 (2)	 <p>Length: 1.0000 μm Width: 4.9277 μm</p>	 <p>σ (10^{-3} S)</p> <p>$y = -1,36\text{E-}04x + 5,30\text{E-}01$</p> <p>$V_g$ (V)</p>
9.3	 <p>Length: 1.0000 μm Width: 5.6023 μm</p>	 <p>σ (10^{-3} S)</p> <p>$y = -3,32\text{E-}04x + 5,81\text{E-}01$</p> <p>$V_g$ (V)</p>

9.4	 <p>Length: 1.5000 μm Width: 9.8923 μm</p>	 <p>$\sigma (10^{-3} S)$</p> <p>$y = -4,20E-04x + 9,28E-01$</p> <p>$V_g (V)$</p>
9.5	 <p>Length: 1.0000 μm Width: 2.3006 μm</p>	 <p>$\sigma (10^{-3} S)$</p> <p>$y = -1,77E-04x + 8,98E-01$</p> <p>$V_g (V)$</p>
9.6	 <p>Length: 2.0000 μm Width: 7.2462 μm</p>	 <p>$\sigma (10^{-3} S)$</p> <p>$y = -3,45E-04x + 1,68E+00$</p> <p>$V_g (V)$</p>
9.7	 <p>Length: 1.5000 μm Width: 5.3397 μm</p>	 <p>$\sigma (10^{-3} S)$</p> <p>$y = -2,31E-04x + 5,86E-01$</p> <p>$V_g (V)$</p>

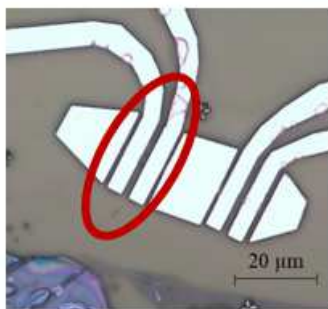
9.8	 <p>Length: 1.0000 μm Width: 1.9520 μm</p>	 <p>σ (10^{-3} S)</p> <p>$y = -2,11\text{E-}04x + 6,51\text{E-}01$</p> <p>$V_g$ (V)</p>
9.9 (1)	 <p>Length: 1.5000 μm Width: 15.7874 μm</p>	 <p>σ (10^{-3} S)</p> <p>$y = -3,71\text{E-}04x + 7,14\text{E-}01$</p> <p>$V_g$ (V)</p>
9.9 (2)	 <p>Length: 1.0000 μm Width: 9.7844 μm</p>	 <p>σ (10^{-3} S)</p> <p>$y = -2,40\text{E-}04x + 6,20\text{E-}01$</p> <p>$V_g$ (V)</p>
9.10	 <p>Length: 1.4351 μm Width: 6.7851 μm</p>	 <p>σ (10^{-3} S)</p> <p>$y = -2,05\text{E-}04x + 8,76\text{E-}01$</p> <p>$V_g$ (V)</p>

Devices realized on sample 10

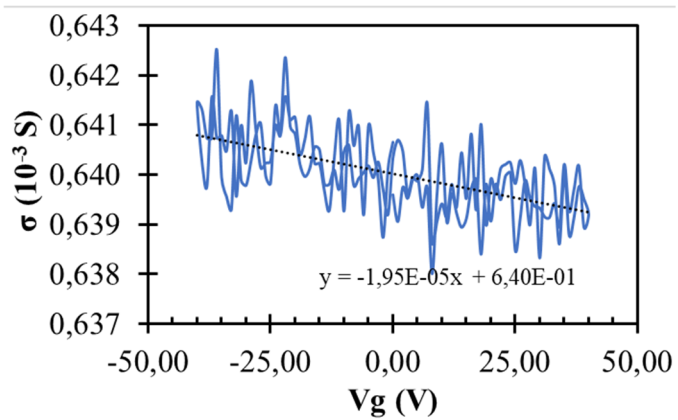
Device	Photo	Conductivity curve
10.1	 <p>Length: 1.4351 μm Width: 6.7851 μm</p>	 <p>$y = -4,02E-04x + 1,35E+00$</p>
10.2	 <p>Length: 1.5969 μm Width: 6.0000 μm</p>	 <p>$y = -9,73E-04x + 7,33E-01$</p>
10.3a	 <p>Length: 1.5000 μm Width: 17.557 μm</p>	 <p>$y = -1,31E-03x + 7,16E-01$</p>

10.3b	 <p>Length: 1.0033 μm Width: 7.1836 μm</p>	 <p>σ ($10^{-3} S$)</p> <p>$y = -1,81E-03x + 4,87E-01$</p> <p>$V_g$ (V)</p>
10.4	 <p>Length: 1.000 μm Width: 2.2260 μm</p>	 <p>σ ($10^{-3} S$)</p> <p>$y = -1,74E-04x + 2,81E-01$</p> <p>$V_g$ (V)</p>
10.5 (1)	 <p>Length: 2.000 μm Width: 4.4927 μm</p>	 <p>σ ($10^{-3} S$)</p> <p>$y = -9,36E-06x + 5,30E-01$</p> <p>$V_g$ (V)</p>

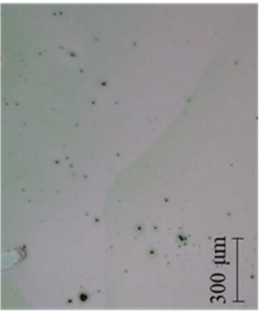
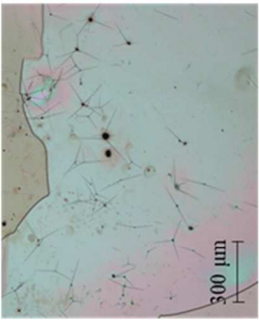


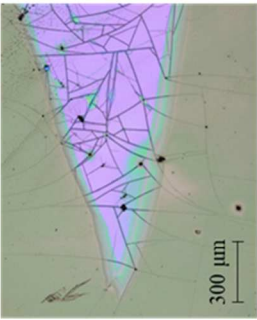
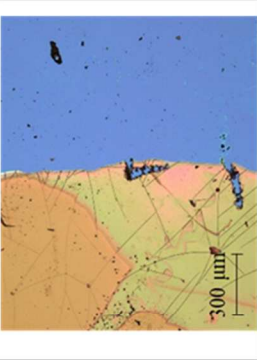
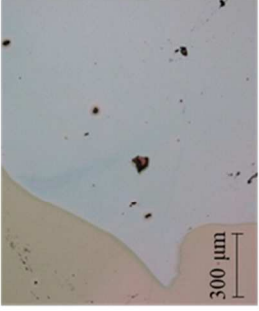
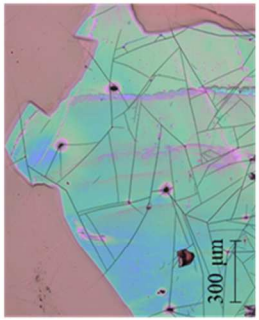

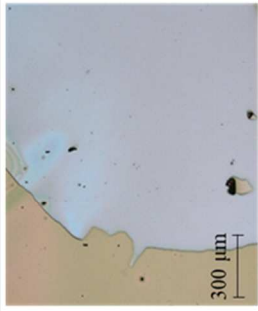
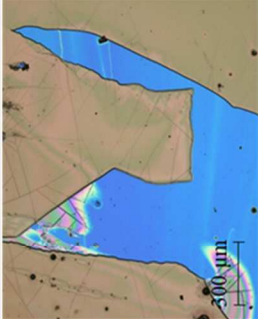

10.5
(2)



Length: 2.0000 μm
Width: 2.8214 μm



Supporting information 5. Study of the exposure time

UV exposure time	After UV exposure	After development	After 5 additional minutes of UV exposure and development
5 min			
10 min			
12 min			
15 min			

Acknowledgements

The work related in this master thesis comes as the coronation of a very international cursus in which I have met and worked with several people in different environments, both from a cultural and a geographical point of view, and as such there are several people that I would like to show my gratitude to.

I would like first of all to thank the three universities that welcomed me during my double degree exchange program. My alma mater, Politecnico di Torino (Italy), is here represented by the two people who most followed me during my cursus. I would then like to thank Prof. Marco Sangermano, the Erasmus referee of my course, for having encouraged me to pursue such an ambitious cursus and supported me throughout all the different countries I worked in, even though we both know he would have preferred I chose another university. And thank you to Dr. Andrea Lamberti, who courageously decided to follow my work even though when I met him I just knew where I was going and not much else about my research topic. I am indebted to both for all the faith and support they gave me.

My host establishment in France, Grenoble INP – Phelma (France), which not only welcomed me in an international environment so different than my own but further encouraged me to pursue further international internships at the other end of the globe. I am deeply thankful to Ms. Anne-Marie Bona for her administrative help during my stay and Prof. Alice Caplier who supported me in the application process for international overseas internship.

Last but not least I would like to show my appreciation to Okayama University (Japan) who welcomed me for my last internship which culminated in this work. I am deeply grateful to Prof. Bernard Chenevier for starting and developing these exchange programs between Grenoble and Okayama, and to all of Kubozono Laboratory of the Research Institute for Interdisciplinary Sciences for welcoming me in their family. I would further like to acknowledge the help and guidance I received from Prof. Yoshihiro Kubozono and Prof. Hidenori Goto, who followed me for my experimental works and Ms. Miwako Kakae for all the administrative help she provided while I was settling down in Japan. And let's not forget Takaki Uchiyama and Akihisa Takai for all the assistance and immense patience they demonstrated while helping me conducting my experiments.

A fundamental role in keeping me sane throughout all my adventures was the one played by the amazing group of colleagues I met while studying at Politecnico di Torino and who became much more than just simple friends. I am not sure I would have made it through so many different environments without such a solid and supportive group always cheering for me. Hence, for providing me with comic relief in difficult moments, for listening to all of my complaints, for their constant friendship and for always showing up whenever I came back to Italy I would like to thank: Matteo Caprioli, Jacopo Barberi, Elisa Albrile, Lorenzo Vigna, Andrea Cosola, Camilla Noè and Marina D'Aloiso.

A special thank goes to my friends Sara Giolo and Miriam Paschetta, but most of all to my favourite harpist, Ginevra Giobbio, who always supported me and never complained about all of my relocations and my absence to important moments of her life such as her graduation ceremony. And to top it all, to be sure I would get on the right plane to come back home and not hop somewhere else around the world, she came to pick me up in the land of the Rising Sun.

A special mention goes to the amazing group of girls who helped me during my stay in Japan: Anna Lusuardi, Chiara Locatelli, Orsola Chini. Thank you, my young marmots, for helping me learning the basics of Japanese, for translating everything all the time and for always supporting me even though engineering sciences aren't your field of study. Without you, Japan would have been much more boring.

Finally, I would like to thank my family for their constant support in my crazy plans for my academic career. I would like to thank my parents for infusing in me from the most tender age the love for foreign languages and cultures: without that, I would have certainly not have spent the last two years and a half in three different countries and two different continents! I would like to dedicate a special thought to my aunt Lorena, who sadly won't be able to witness the end of this adventure which she always followed with enthusiasm, and to my uncle Guido to whom I wished I could have been closer in such a sad period. Finally, the biggest thank you goes to my grandmother for everything she has done to get accustomed to my leaving home for so long, for bearing it with such fortitude and for hiding most of her worries, fears and sorrows to fully support me.

To sum it up: *"So Long, and Thanks for All the Fish"*. (D. Adams)

Ringraziamenti finali

Questa tesi rappresenta il culmine di un percorso tortuoso lungo il quale ho conosciuto e collaborato con un grande numero di persone in diversi ambienti accademici e di ricerca, sia dal punto di vista culturale che geografico, e come tale richiede un diffuso ringraziamento di svariate persone e istituzioni.

In primo luogo vorrei ringraziare le tre facoltà che mi hanno accolto durante il progetto di doppia laurea internazionale.

Innanzitutto, il mio *alma mater*, il Politecnico di Torino (Italia), che ritengo rappresentato al meglio dai due docenti che più mi hanno seguito in questo periodo. Il Prof. Marco Sangermano, referente dei progetti Erasmus del mio corso di studio, che mi ha da subito appoggiata e incoraggiata ad intraprendere un simile percorso. Grazie professore per il supporto che mi ha sempre dato nei vari paesi in cui sono finita a lavorare, sebbene entrambi sappiamo che l'università da me scelta non era quella che lei avrebbe preferito. E il Dott. Andrea Lamberti, che coraggiosamente ha deciso di imbarcarsi in questa strana avventura nonostante quando ci siamo incontrati io sapessi solo dove stessi andando e vagamente cosa andassi a fare in questo misterioso laboratorio giapponese. Grazie per la fiducia dimostratami sin da subito.

Quindi la mia università di adozione in Francia, Grenoble INP – Phelma, che non solo mi ha accolta a braccia aperte in un ambiente così diverso da quello cui ero abituata, ma mi ha incoraggiata a spingere oltre questa mia tendenza all'internazionalizzazione mandandomi all'altro capo del globo. Vorrei in particolare ringraziare la Sig.ra Anne-Marie Bona, per il supporto amministrativo e l'interesse dimostratomi durante l'intero soggiorno francese, e la Prof.ssa Alice Caplier per il supporto durante le procedure per la finalizzazione del tirocinio all'estero.

In ultimo, ma non per importanza, vorrei esprimere la mia riconoscenza verso l'università di Okayama (Giappone) che mi ha accolta per svolgere il tirocinio finale del mio percorso. Un profondo ringraziamento va al Prof. Bernard Chenevier per aver iniziato e sviluppato il programma di scambio tra Grenoble e Okayama, e a tutti i membri del laboratorio del Prof. Kubozono dell'Istituto di Ricerca per le Scienze Interdisciplinari (RIIS) per avermi accolto nella loro famiglia. Sono molto grata per l'aiuto e la guida ricevuta al Prof. Yoshihiro Kubozono e al Prof. Hidenori Goto, che mi ha seguito per la parte sperimentale della tesi, e alla Sig.ra Miwako Kakae per tutto l'aiuto e il supporto che mi ha dedicato durante il mio soggiorno in Giappone. E non si possono non citare Takaki Uchiyama e Akihisa Takai, per l'aiuto e l'immensa pazienza che hanno dimostrato nei miei confronti durante gli esperimenti.

Un ruolo fondamentale nel mantenermi sana di mente durante tutte queste avventure in giro per il mondo accademico è sicuramente stato quello svolto dal gruppo di straordinari colleghi conosciuti durante i miei anni al Politecnico di Torino. Ragazzi, lo sapete spero, oramai non siete più un semplice gruppo di amici, siete diventati parte integrante della mia famiglia. Non ce l'avrei mai fatta con tutti i cambiamenti e gli shock culturali senza un gruppo come voi a sostenermi sempre e comunque. Quindi, per essere sempre riusciti a risollevarmi il morale nei momenti bui, per aver pazientemente ascoltato tutte le mie lamentele, per essere sempre stati presenti ad ogni mio ritorno, insomma, per avermi supportata ma soprattutto sopportata, vorrei ringraziare in modo particolare: Matteo Caprioli, Jacopo Barberi, Elisa Albrile, Lorenzo Vigna, Andrea Cosola, Camilla Noè e Marina D'Aloiso.

Un ringraziamento particolare va alle mie amiche Sara Giolo e Miriam Paschetta, ma soprattutto alla mia arpista preferita, Ginevra Giobbio. Mi hai sempre spalleggiata, non ti sei mai lamentata di tutti i miei trasferimenti, della mia assenza in momenti particolarmente importanti, uno tra tutti la tua laurea in Chimica Industriale ma soprattutto ti sei voluta assicurare personalmente del mio rientro in Italia

venendo addirittura a cercarmi fino nel paese del Sol levante. Grazie Caballo per non aver mai perso la speranza nei confronti di questo matto Cioccolatino.

Infine, una menzione speciale per il fantastico gruppo di ragazze che ho conosciuto e che mi hanno aiutata mentre ero in Giappone: Anna Lusuardi, Chiara Locatelli, Orsola Chini. Grazie mie giovani marmotte per avermi aiutata ad imparare le basi del Giapponese, per tutte le volte che avete dovuto tradurmi anche le frasi più semplici, per avermi sostenuta nonostante l'ingegneria non sia proprio il vostro pane quotidiano. Senza di voi, il Giappone sarebbe stato molto più noioso.

Per chiudere la serie di ringraziamenti, vorrei ringraziare la mia famiglia per il costante incoraggiamento nel portare a termine i folli piani della mia carriera accademica. Vorrei ringraziare i miei genitori per avermi infuso dalla più tenera età l'amore per le lingue e le culture straniere. Senza di questo, non mi ritroverei di certo ad aver passato gli ultimi due anni e mezzo della mia vita in tre diversi paesi e due diversi continenti! Vorrei dedicare un pensiero speciale a Lorena, che purtroppo non potrà assistere alla fine di questa avventura che ha sempre seguito con molta partecipazione, e a mio zio Guido cui non sono potuta essere vicina quanto avrei voluto in questo periodo così triste. Ma il ringraziamento più grande va a Nonna Gianna per tutto quello che ha fatto per abituarsi al fatto che andassi così lontana per così tanto tempo, per averlo sopportato con tale forza d'animo e per essere riuscita a nascondere la maggior parte delle sue preoccupazioni, paure e tristezze per potermi sostenere al massimo. Grazie di tutto.

Per farla breve: "Addio e grazie per tutto il pesce" (D. Adams)